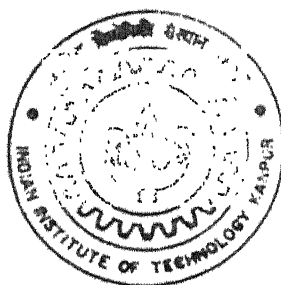


PHASE FORMATION AND ELECTRICAL PROPERTIES OF DOPED AND UNDOPE NANOCRYSTALLINE ZrO_2 THIN FILMS ON STAINLESS STEEL

by

Shiladitya Paul

TH
MSP/2003/M
P 262p



MATERIALS SCIENCE PROGRAMME

Indian Institute of Technology Kanpur

MAY, 2003

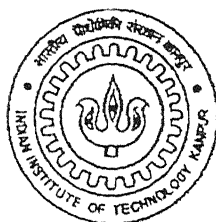
**PHASE FORMATION AND ELECTRICAL
PROPERTIES OF DOPED AND UNDOPED
NANOCRYSTALLINE ZrO_2 THIN FILMS ON
STAINLESS STEEL**

*A thesis submitted in partial fulfillment of the requirements for
the degree of*

MASTER OF TECHNOLOGY

by

SHILADITYA PAUL



To the

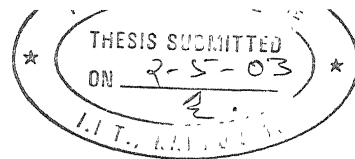
**MATERIALS SCIENCE PROGRAMME
INDIAN INSTITUTE OF TECHNOLOGY KANPUR
MAY, 2003**

2 - AUG 2003

दुर्धत्तम काशीनाथ ढेलकर पुस्तकालय
भारतीय प्रौद्योगिकी संस्थान कानपुर
अवधि क्र० A...144412

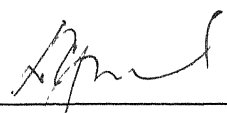


A144412



CERTIFICATE

This is to certify that the work contained in this thesis entitled " Phase formation and electrical properties of doped and undoped nanocrystalline ZrO_2 thin films on stainless steel ", by Mr. Shiladitya Paul (Roll No. Y111210), has been carried out under my supervision and to the best of my knowledge it has not been submitted elsewhere for a degree.



Dr. D. C. Agrawal
Professor

Materials Science Programme

May, 2003

Indian Institute of Technology Kanpur

Dedicated

To

My Parents

Acknowledgement

I would like to thank my supervisor Prof. D. C. Agrawal for introducing me to the field of sol-gel zirconia thin films and impedance spectroscopy. I thank him for his patience, constant encouragement and excellent guidance. I am grateful to him for his generosity. I wish that he will keep in touch with me in future and will continue to give his valuable advice

I am very grateful to Prof J Kumar for his help and advices during my thesis work. I want to thank all the staff of the ACMS, MSP, Glass Blowing Lab and FEAT Lab for their help and support during the entire course of work. Especially, I would like to thank Mr. Umashankar Singh, Mr G. S. Thapa and Mr Sushanta Pal for their constant help.

Thanks are in store for my lab mates and batch mates for their help and cooperation. It was a nice and memorable association with all of them. During this long stay at I.I.T. Kanpur many people helped in different ways and it is not possible to acknowledge each of them in this small space. I thank them all for their help and their cooperation. The list would be incomplete if I don't thank Mr. Dinesh Deva who rendered help with AFM whenever asked for.

I wish to give a heartfelt thanks to Dr. K. K. Kar his constant help and support.

The silent support from my family members was always a constant source of inspiration for me during my stay.

Shiladitya Paul

Contents

| <u>Topic</u> | Page Nos. |
|--|-----------|
| List of figures and tables | i - v |
| Abstract | vi |
| Chapter 1 Introduction | 1 |
| 1.1 Zirconia ceramics and their importance | 1 |
| 1.2 Stability of zirconia phases | 1 |
| 1.3 Electrical properties of zirconia ceramics | 3 |
| 1.4 Zirconia thin films | 7 |
| 1.4.1 Zirconia films on steel | 7 |
| 1.4.2 Electrical properties of zirconia thin films | 9 |
| 1.5 The Sol-gel process | 13 |
| 1.5.1 Chemistry of Sol-gel processing | 14 |
| 1.6 Spin coating process | 15 |
| 1.7 Impedance spectroscopy | 17 |
| 1.7.1 Complex impedance plane analysis | 18 |
| (a) Pure resistor circuit (R) | 19 |
| (b) Pure capacitor circuit (C) | 19 |
| (c) Series combination of R and C | 20 |
| (d) Parallel combination of R and C | 20 |
| 1.8 Statement of the problem | 23 |

Chapter 2 Experimental Procedure **24**

| | |
|---|----|
| 2.1 Sol preparation | 24 |
| 2.1.1 Apparatus used | 25 |
| 2.1.2 Procedure for sol preparation | 25 |
| 2.2 Substrate preparation | 28 |
| 2.2.1 Substrate | 28 |
| 2.2.2 Polishing | 28 |
| 2.2.3 Cleaning | 28 |
| 2.3 Thin film deposition | 29 |
| 2.4 Characterization of films | 30 |
| 2.4.1 Microscopy of films | 30 |
| 2.4.2 Atomic Force Microscopy (AFM) | 31 |
| 2.4.3 Thickness measurements | 32 |
| 2.4.4 X-ray diffraction | 32 |
| 2.4.5 Deposition of Au-Pd top electrode on the film | 34 |
| 2.4.6 Electrical measurements | 34 |
| 2.4.6.1 Sample configuration | 34 |
| 2.4.6.2 Thin film heater | 35 |
| 2.4.7 Impedance analysis | 36 |
| 2.4.8 Impedance data analysis | 37 |
| 2.4.9 Dielectric constant and dielectric loss | 39 |

Chapter 3 Results and Discussion

| | |
|---|----|
| 3.1 Thickness and microstructure of films | 41 |
| 3.2 Phase analysis by x-ray diffraction | 42 |
| 3.3 Electrical properties | 43 |
| 3.4 Dielectric constant | 47 |
| 3.5 Dielectric loss | 48 |
| 3.6 Discussion | 49 |

Chapter 4 Summary and Conclusion **97**

| | |
|---|-----|
| References | 101 |
| Appendix -1: Calculation of the amounts of different Ingredients used for the preparation of sol | 105 |
| Appendix -2: Calibration of impedance analyzer | 109 |
| Appendix-3: Cole-Cole plots for different samples | 110 |

List of Figures

| <u>Figure No.</u> | <u>Title</u> | <u>Page No.</u> |
|-------------------|---|-----------------|
| 1.1 | The fluorite crystal structure | 3 |
| 1.2 | Complex impedance plots for 7.5 mole % Y_2O_3 - ZrO_2 ceramics at 290°C | 4 |
| 1.3 | Arrhenius plots showing variation in conductivity with Y_2O_3 content | 5 |
| 1.4 | Influence of the amount Y_2O_3 on the activation energy of YSZ single crystals in the temperature range 180-520°C | 6 |
| 1.5 | Oxidation kinetics curves of uncoated and ZrO_2 coated mild steel | 7 |
| 1.6 | XRD patterns of rapidly annealed ZrO_2 | 8 |
| 1.7 | Temperature dependence of resistance for YSZ thin films of different thickness | 10 |
| 1.8 | Cole-Cole plots of (a) ZrO_2 :16%Sc thin films on Al_2O_3 substrates and (b) 3 mole % YSZ single crystal | 11 |

| <u>Figure No.</u> | <u>Title</u> | <u>Page No.</u> |
|--------------------------|--|------------------------|
| 1.9 | (a) Arrhenius plots of conductivity and (b) film thickness dependence of activation energy of 4.9 mole % Y_2O_3 doped ZrO_2 thin film deposited on different substrates | 11 |
| 1.10 | Scheme describing a basic spinning process | 17 |
| 1.11 | Impedance plots for parallel combination of a resistor and a capacitor | 21 |
| 2.1 | Flow chart for sol preparation | 26 |
| 2.2 | The AFM feedback loop | 31 |
| 2.3 | MOM capacitor configuration showing substrate, film and Au-Pd top electrode | 35 |
| 2.4 | Sample holder for electrical measurements | 35 |
| 3.1.1 | Thickness profile of fired Gd_2O_3 - ZrO_2 thin films of (a) 4 mole %, (b) 5 mole % and (c) 9 mole % Gd_2O_3 content | 51 |
| 3.1.2 | AFM topographic images of (a) pure zirconia thin film, (b) 5 mole % Gd_2O_3 - ZrO_2 film and (c) 9 mole % Gd_2O_3 - ZrO_2 film with a scan area of 300 nm x 300 nm | 52 |
| 3.2 | X-ray diffraction plots of (a) heat treated steel, (b) as obtained steel, (c) pure zirconia film (as deposited), (d) pure zirconia, (e) ZrO_2 -1.75 mole% Gd_2O_3 , (f) ZrO_2 -2.5 mole% Gd_2O_3 , (g) ZrO_2 -4 mole% Gd_2O_3 , (h) ZrO_2 -5 mole% Gd_2O_3 , (i) ZrO_2 -8 mole% Gd_2O_3 , (j) ZrO_2 -9 mole% Gd_2O_3 , (k) ZrO_2 -11 mole% Gd_2O_3 | 54 |

| <u>Figure</u> <u>No.</u> | <u>Title</u> | <u>Page No.</u> |
|---|--|------------------------|
| 3.3 | Optical micrographs of $\text{Gd}_2\text{O}_3\text{-ZrO}_2$ thin films (a) 1.75 mole % $\text{Gd}_2\text{O}_3\text{-ZrO}_2$, (b) 4 mole % $\text{Gd}_2\text{O}_3\text{-ZrO}_2$, (c) 5 mole % $\text{Gd}_2\text{O}_3\text{-ZrO}_2$, (d) 11 mole % $\text{Gd}_2\text{O}_3\text{-ZrO}_2$ | 57 |
| 3.4 | AFM phase images of (a) pure, (b) 5 mole % $\text{Gd}_2\text{O}_3\text{-ZrO}_2$ and (c) 9 mole % $\text{Gd}_2\text{O}_3\text{-ZrO}_2$ films | 58-59 |
| 3.5 | Cole-Cole plots for pure ZrO_2 thin film at different temperatures | 60-61 |
| 3.6 | Cole-Cole plots for 1.75mole% $\text{Gd}_2\text{O}_3\text{-ZrO}_2$ thin film at different temperatures | 62-63 |
| 3.7 | Cole-Cole plots for 2.5 mole % $\text{Gd}_2\text{O}_3\text{-ZrO}_2$ thin film at different temperatures | 64-65 |
| 3.8 | Cole-Cole plots for 4 mole % $\text{Gd}_2\text{O}_3\text{-ZrO}_2$ thin film at different temperatures | 66-67 |
| 3.9 | Cole-Cole plots for 5 mole % $\text{Gd}_2\text{O}_3\text{-ZrO}_2$ thin film at different temperatures | 68-69 |
| 3.10 | Cole-Cole plots for 8 mole% $\text{Gd}_2\text{O}_3\text{-ZrO}_2$ thin film at different temperatures | 70-71 |
| 3.11 | Cole-Cole plots for 9 mole% $\text{Gd}_2\text{O}_3\text{-ZrO}_2$ thin film at different temperatures | 72-73 |

| <u>Figure No.</u> | <u>Title</u> | <u>Page No.</u> |
|--------------------------|--|------------------------|
| 3.12 | Cole-Cole plots for 11 mole% $\text{Gd}_2\text{O}_3\text{-ZrO}_2$ thin film at different temperatures | 74-75 |
| 3.13 | Cole-Cole plots for pure and $\text{Gd}_2\text{O}_3\text{-ZrO}_2$ thin films at different temperatures | 76-79 |
| 3.14 | Arrhenius plots of $\ln(\sigma)$ versus $1000/T$ for pure and $\text{Gd}_2\text{O}_3\text{-ZrO}_2$ thin films of different compositions | 80-81 |
| 3.15 | Variation of dc conductivity with temperature for samples with different Gd_2O_3 content | 82 |
| 3.16 | Activation energy for conduction variation with different compositions of $\text{Gd}_2\text{O}_3\text{-ZrO}_2$ thin films | 83 |
| 3.17 | ϵ_r is plotted against frequency for different compositions at different temperatures | 84 - 85 |
| 3.18 | Frequency variation of the dielectric loss for pure ZrO_2 and Gd_2O_3 doped ZrO_2 systems on log scale at different temperatures | 86-87 |
| 3.19 | Variation of dielectric loss with temperature and Gd_2O_3 content at 100kHz | 88 |

List of Tables

| <u>Table No.</u> | <u>Title</u> | <u>Page No.</u> |
|------------------|---|-----------------|
| 1.1 | Activation energies for different mole % of YSZ | 5 |
| 2.1 | Chemicals used in the preparation of thin films | 24 |
| 2.2 | Operating parameters for XRD | 32 |
| 2.3 | Standard XRD data of stainless steel | 33 |
| 2.4 | The displays 'A' and 'B' of impedance analyzer | 37 |
| 3.1 | Thickness of films prepared under different conditions | 89 |
| 3.2 | Standard diffraction data for zirconia phases | 90 |
| 3.3 | X-ray diffraction analysis chart | 91-93 |
| 3.4 | Conductivity and Activation energy values of $\text{Gd}_2\text{O}_3\text{-ZrO}_2$ ceramics for different compositions and temperatures. | 94-95 |
| 3.5 | Grain Conductivity in Bulk and Thin Film Samples compared at $\sim 280^\circ\text{C}$ | 96 |

Abstract

Zirconia, ZrO_2 , is an important ceramic material having diverse applications because of its interesting mechanical and electrical properties. Pure ZrO_2 exists in monoclinic (m) structure at room temperature. It transforms to a tetragonal (t) structure at 1150°C and to a cubic (c) structure at 2350°C before undergoing solid-liquid transition at 2680°C . Monolithic ZrO_2 ceramics are prepared from powders and require a sintering step at high ($\sim 1500^\circ\text{C}$) temperature, where the t phase is stable. While cooling from the sintering temperature, the $t \rightarrow m$ transformation occurs martensitically at 950°C . This phase change is accompanied by large volume expansion (4 -6 %) and shear strain (1 -2 %) This results in the disintegration of the sintered body. To avoid this problem, some oxides, called stabilizers, such as CaO , MgO , Y_2O_3 , CeO_2 , Gd_2O_3 etc. are alloyed with ZrO_2 . This causes the t or the c phase to remain stable down to room temperature.

Stabilized t ZrO_2 can transform under a stress to m phase and thus causes a very large increase in toughness. This phenomenon is essentially responsible for the excellent mechanical properties of ZrO_2 ceramics and ZrO_2 toughened ceramics.

ZrO_2 alloyed with di or trivalent oxides has large concentration of oxygen vacancies. This imparts significant ionic conductivity at low temperatures to zirconia ceramics and makes them useful for applications such as oxygen sensors, oxygen pumps, fuel cells, etc. ZrO_2 stabilized with few mole % of Y_2O_3 has been the material most investigated for this purpose.

In the present work, thin films of ZrO_2 alloyed with different amounts of Gd_2O_3 have been investigated. Gd_2O_3 acts as a stabilizer for ZrO_2 and Gd^{3+} has a smaller ionic size than Y^{3+} , which may have beneficial effect on the electrical conductivity. Pure and 1.75, 2.5, 4, 5, 8 and 11 mole % Gd_2O_3 - ZrO_2 thin films having thickness between 0.4 to $0.7\text{ }\mu\text{m}$ are synthesized via sol-gel method on stainless steel substrates. The characterization of all the samples is done using XRD, complex impedance spectroscopy, optical microscopy and atomic force microscopy (AFM). The films are crystalline after heat treatment at 500°C for 10 minutes. The optical and atomic force microscopic analysis shows that the films are crack free. The films dried at a higher temperature ($\sim 200^\circ\text{C}$) develop cracks. The RMS surface roughness value of 0, 5, 9 mole % Gd_2O_3 -

A 500 nm. The films have a very fine grain size 10-25 nm (for 0 and 5 mole % sample) due to the use of a low crystallization temperature (500°C); higher crystallization temperature causes oxidation of the substrate and degradation of the films. Because of very fine grain size, the x-ray peaks are quite broad. Although it appears that all the compositions crystallize in the cubic/ tetragonal structure, the electrical conductivity data indicates that the m phase may be present at low Gd₂O₃ concentration. The presence of the orthorhombic phase, as suggested in an earlier investigation, is ruled out.

The impedance data taken at different temperatures (25 to 280°C) is used to construct the Cole-Cole plots. The plots consist of only one semicircle corresponding to the grain boundary resistance. The conductivity of the films increases with an increase in temperature. The conductivity has a high value for compositions that fall in the single phase region (m for 1.75 %, t for 4 % and c for 8-9 mole %) and is low in the intermediate compositions corresponding to the intermediate regions. The activation energy for conduction is calculated using the Arrhenius equation. The activation energy for conduction has a value of about 0.29 eV for the compositions in the t phase region and 0.38 eV in the m and c phase regions. The low activation energy value suggests that thermal annealing after electrode deposition has an effect on the concentration of free oxygen vacancies.

The dielectric property of the samples is examined using an impedance analyzer. The dielectric constant has a very high value at low frequency and it decreases with an increase in frequency and decrease in temperature for all samples. The dielectric loss decreases very rapidly below 100 kHz but is almost constant at frequencies > 100 kHz. There appears to be a periodic variations in dielectric loss with Gd₂O₃ content and such variation becomes more pronounced with an increase in temperature.

Chapter 1.

Introduction

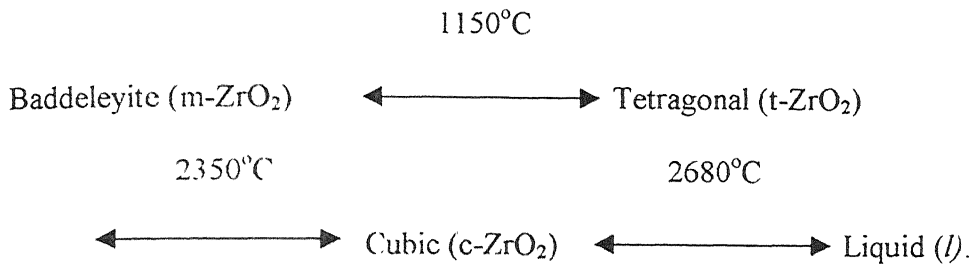
1.1 Zirconia ceramics and their importance

Zirconia ceramics have a unique set of properties such as high refractoriness, good corrosion resistance and mechanical strength, high fracture toughness and hardness, high ionic conductivity at elevated temperatures, low thermal conductivity at high temperatures, high thermal stability and resistance to thermal shock¹. Various stabilizing agents such as CeO_2 ², Y_2O_3 ³, MgO ⁴, CaO and rare earth oxides⁵ are used to form cubic or tetragonal modifications that remain stable at room temperature. Stabilized zirconia is used as ceramic storage heaters, oxide thermistors, hydrogen generators, oxygen detectors and high temperature fuel cells. Thin film applications of zirconia include oxidation resistant coatings⁶, sensor films⁷, catalytic films, transparent films and anti glare coatings.

1.2 Stability of zirconia phases

It is well known that ZrO_2 can crystallize in the different phases depending on the temperature and dopant concentration. These phases can be partially (PSZ) or fully (FSZ) stabilized at room temperature by the addition of suitable dopants, e.g. Y_2O_3 , CaO and MgO . However even in these well-studied systems, there has been considerable confusion as to the exact location of phase boundary⁸.

There are at least five known polymorphs of ZrO_2 . These are monoclinic (m- ZrO_2), tetragonal (t- ZrO_2), cubic (c- ZrO_2), hexagonal and the high-pressure orthorhombic phase. The orthorhombic phase exists as either ortho (I) or ortho (II). The stability of these phases depends on temperature, pressure and the amount of additive. Thus, for pure zirconia the monoclinic phase is stable upto $\sim 1100^\circ\text{C}$ after which it transforms to the tetragonal phase within a range of 100°C . At around 2350°C it finally undergoes a phase change to cubic fluorite structure.



Ohtaka et. al.⁹ prepared ortho I & II phases of ZrO_2 by doping with HfO_2 at high pressure. They also reported a phase diagram where they distinguished between Ortho I & II phases. Many workers have also tried rare earth dopants for stabilization of zirconia. CeO_2 as a dopant has been studied by Rossignol et. al.².

The destructive phase transformation from t- ZrO_2 to m- ZrO_2 accompanied by 4 to 6% volume increase and 1 to 2% shear strain renders pure ZrO_2 unsuitable for engineering use. Thus stabilizers are essential for retaining the tetragonal phase at room temperature. Aliovalent oxides such as R_2O_3 ($\text{R} = \text{Y, Gd, Nd, Sc}$ etc), CaO , MgO , etc. are effective stabilizers, which when added to ZrO_2 stabilize the tetragonal and cubic phases of ZrO_2 . Monoclinic zirconia has Zr^{4+} ion coordinated with seven oxygen ions which after substitution by other aliovalent oxides causes the creation of oxygen vacancies in order to maintain the overall charge neutrality. This reduces the internal strain, which stabilizes the cubic fluorite structure of zirconia.

Phase transition and elasticity in zirconia was studied by Cohen et . al.¹⁰ by using an ab initio model. The instability and resulting phase transition of cubic zirconia was extensively studied by Shibata et. al.³ . The effect of RO_2 ($\text{R} = \text{Ce}, \text{Ti}$) and R_2O_3 ($\text{R} = \text{rare earth element}$) type additives was studied in some detail. They found that the electrical repulsive interaction between the neighboring oxygen ions was responsible for the instability. The addition of more than 10 mole % Gd_2O_3 in ZrO_2 results in formation of fluorite type phase¹¹ . This structure contains metal ions at the body corners and face centers and the oxygen ions occupy the eight tetrahedral voids as seen in figure 1.1.

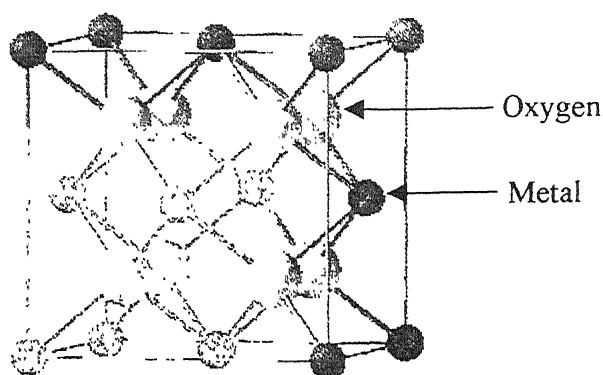


Fig.1.1 The fluorite crystal structure

1.3 Electrical properties of zirconia ceramics

Zirconia based solid electrolyte systems doped with many rare earth and alkaline earth metal oxides are used in many applications such as oxygen sensors, catalytic membrane reactors, etc. Solid solutions of ZrO_2 with oxides of divalent and trivalent cations show a high ionic conductivity at elevated temperatures ($>1000 \text{ K}$). The ionic conductivity of the phase-stabilized zirconia depends on various factors such as composition, grain size, microstructure, phases, porosity and purity¹². Annealing temperature and time also effects the ionic conductivity of YSZ ceramics¹³.

The high electrical conductivity in stabilized zirconia at elevated temperatures is due to the mobile oxygen ion vacancies created in the oxygen sub-lattice, in order to preserve charge neutrality when the lower valent dopant cation (e.g. Y^{3+}) is substituted for Zr^{4+} sites.

Electrical properties of any ceramic system are conveniently studied by impedance spectroscopy¹⁴. The impedance spectra of bulk zirconia ceramics shows two semicircles and an electrode arc^{15, 16, 17, 18} at high, intermediate and low frequencies respectively (figure 1.2). These correspond to grain, grain boundary and electrode response.

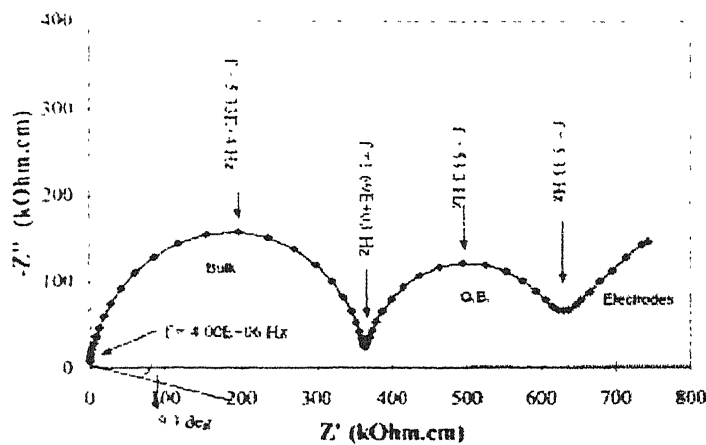


Fig.1.2 Complex impedance plots for 7.5 mole% Y_2O_3 - ZrO_2 ceramics at 290°C.

Moztarzadeh¹¹ found that the electrical conductivity of Gd_2O_3 doped zirconia decreases with increase in Gd_2O_3 concentration from 10 to 30mol %. They assigned this behavior to formation of certain associates at higher Gd_2O_3 concentration. Electrical conductivity of YSZ- Gd_2O_3 doped CeO_2 (YSZ-CGO) exhibits a minimum when Ce and Zr are present at almost equimolar quantities¹⁹. The variation of conductivity with temperature was studied in detail by Luo et. al¹⁷ (figure1.3). Low temperature ionic conductivity of 9.4 mole% YSZ single crystals was studied by Solier et. al.²⁰. They observed a decrease in the activation energy values from 1.16 eV at $T < 360^\circ C$ to

0.84 eV at $T > 450^\circ\text{C}$ while, Srđić et. al.²¹ obtained an activation energy value of 0.78 and 1.00 eV for grain and grain boundary conduction in 9.4 mole % YSZ the temperature range 75 – 825°C.

Ramamoorthy et. al.¹² have reported the activation energy for ionic conduction in grain, grain boundaries and for total conductivity in YSZ with different dopant concentration in the temperature range 573 – 1173 K (table 1.1). They showed that for ultrafine-grained materials the total conductivity is mainly influenced by the grain boundaries.

Table 1.1 Activation energies for different mole % YSZ

| Y ₂ O ₃ Concentration (mole %) | E _a (grain) (eV) | E _a (grain boundary) (eV) | E _A (total ionic conductivity) (eV) | |
|--|---------------------------------|---|---|---------|
| | | | ref. 12 | ref. 17 |
| 2 | 0.98 | 1.20 | 1.17 | |
| 3 | 0.97 | 1.21 | 1.12 | 0.593 |
| 4.5 | 1.12 | 1.27 | 1.27 | |
| 6 | 1.02 | 1.20 | 1.18 | |
| 9 | 1.17 | 1.31 | 1.29 | |
| 12 | 1.22 | 1.35 | 1.32 | 1.255 |

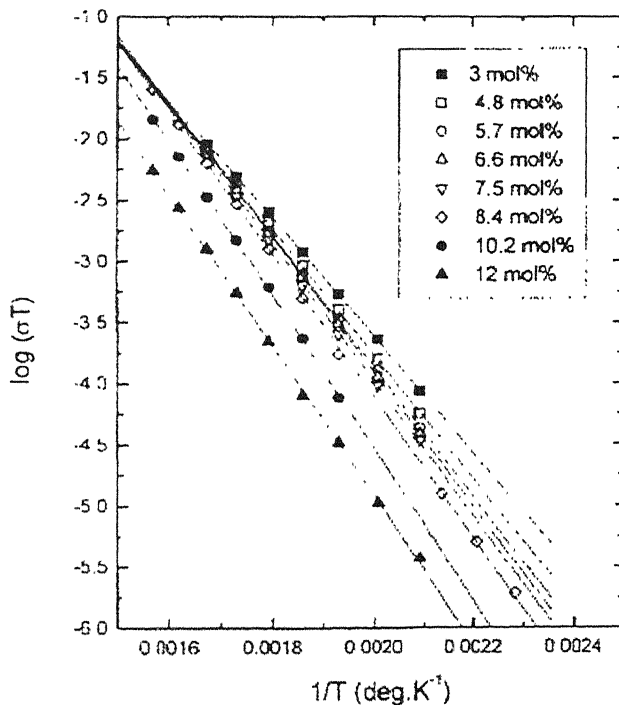


Fig. 1.3 Arrhenius plots showing variation in conductivity with Y₂O₃ content.

The 4.5 mole % YSZ shows higher activation energy than that of the 6 mole % YSZ. This may be due to the presence of mixed c and t phases in 4.5 mole % YSZ.

The defects such as vacancies generated by the substitution of Y^{3+} ions and association of defect complexes play a significant role in the ionic conduction. The effect of a wide range of Y_2O_3 additions on the electrical conductivity (σ) and activation energy (E_a) (figure 1.4) was studied on YSZ single crystals by Hartmanova et. al.⁸. Electrical conductivity (σ) of the investigated systems exhibited its maximum value close to the tetragonal-cubic phase boundary i. e. ~ 4.3 mol% Y_2O_3 .

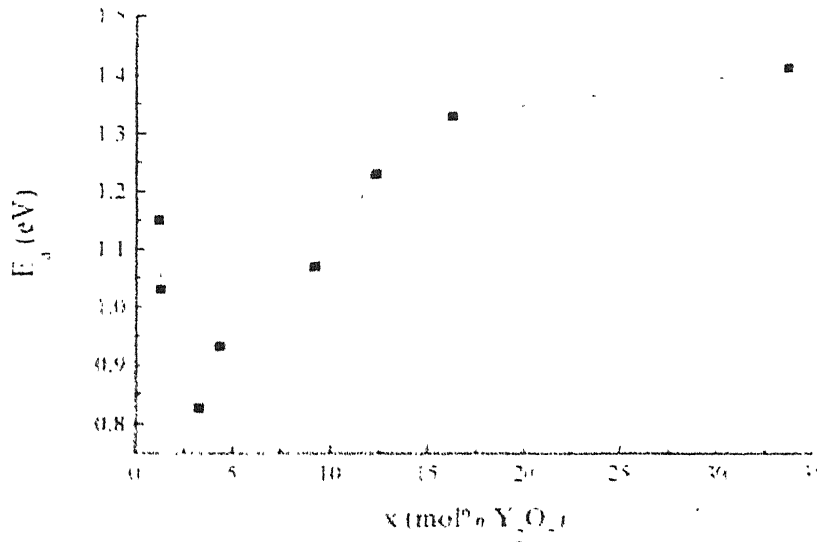


Fig. 1.4 Influence of the amount of Y_2O_3 on the activation energy of YSZ single crystals in the temperature range 180 – 520°C.

Zirconia is an insulating, direct wide-gap metal oxide with an optical band gap of ~ 5.0 eV. Thus it is expected to be an insulator at ordinary temperatures. The effect of additives on the electrical behavior of ZrO_2 ceramics has already been emphasized.

1.4 Zirconia thin films

Zirconia thin films have been extensively studied due to their wide applications. Interesting areas of applications include thermal barrier coatings²², sensor films⁷, catalytic films, transparent films, wear and oxidation resistance coatings²³ and fuel cells. Various deposition techniques have been tried which include PVD, CVD, plasma or thermal spraying and sol-gel method. Among these the sol-gel technique has an added advantage of producing uniform, homogeneous films at low temperature.

1.4.1 Zirconia films on steel

The protection of metal components in aggressive environments is one of the promising applications of sol-gel zirconia films

Li et. al.^{6, 23} deposited sol-gel ZrO_2 coatings using propoxide, Acetyl Acetone, and water on mild steel substrate and studied their oxidation resistance as shown in figure 1.5. The intermediate heat treatment was at 400°C for 5min in Ar and the final heat treatment was at 600°C for 1hr in Ar.

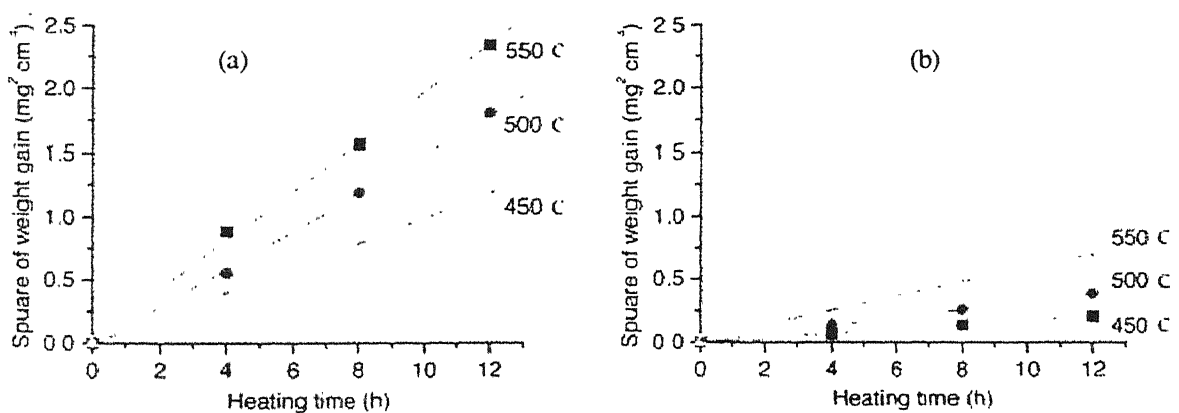


Fig.1.5 Oxidation kinetics curves of (a) uncoated and (b) coated mild steel

In the coated substrate very weak peaks, one each of t-ZrO₂ at $2\theta = 30.5^\circ$ and m-ZrO₂ at $2\theta = 31.5^\circ$ were observed. They concluded that the oxidation resistance of mild steel was improved by the application of zirconia coatings.

Paterson and Ben-Nissan²⁴ studied multi-layered sol-gel ZrO₂ coatings on 316 stainless steel. They used intermediate firing temperature of 380⁰C for 1hr and the final firing temperature of 800⁰C for 1, 2, 4, 8 and 12 hrs (SET-I). Some samples were subjected to firing at 380⁰C and 800⁰C (SET-II) after each coating. The coating thickness varied from 300 to 1032nm. X-ray diffraction showed that both set I and set II samples had a mixture of metastable cubic and monoclinic phases. The amount of m-phase was found to increase as the thickness increased from 344nm to 1032nm. The amount of cubic phase in this case increased as the film thickness increased. The authors²⁵ in their other work resorted to AFM and SEM that revealed that SET-I firing regime was detrimental to the film morphology that resulted in cracking and delamination of the films.

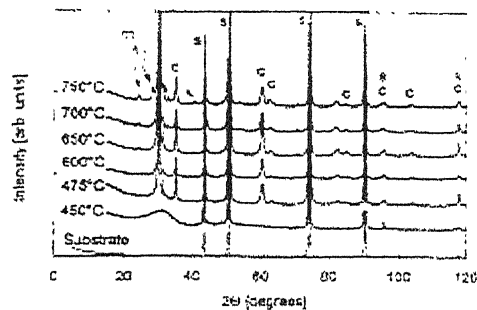


Fig. 1.6 XRD patterns of rapidly annealed ZrO₂ films (450-750°C)

Mehner et. al.²⁶ deposited ZrO₂-thin films on polished 304 stainless steel by a sol-gel process based on zirconium-n-propoxide. The films were dried at 200⁰C for 30 min and two different heat treatment schedules were followed. The XRD of films annealed at 475⁰C or above showed

sharp diffraction lines corresponding to metastable cubic or t- ZrO_2 . A distinction between these two could not be made due to close proximity of the diffraction lines (figure 1.6). Formation of high compressive stresses up to -750 MPa was detected in the films with crystallite size in the range 13-20 nm

Di Maggio et. al.²⁷ deposited stabilized zirconia thin films on 304 stainless steel by PVD and dip coating method. A 10 layer dip coated sample of thickness ~150 nm was produced by drying each layer at 250⁰C for 3 min followed by a final heat treatment at 500⁰C in vacuum. The oxidation kinetics studied at 850⁰C up to 15 hrs in air followed a parabolic trend.

Thus most of the above works supported Garvie's hypothesis that explains the stabilization of nanocrystalline ZrO_2 but there remains uncertainty as to why metastable cubic phase is formed in Zirconia thin films on stainless steel.

1.4.2 Electrical properties of zirconia thin films

Oxygen sensors have been widely used in several fields, such as experimental measurements, medical engineering and monitoring and control of large combustion furnaces. YSZ has been most widely used in the above mentioned applications due to its relatively high ionic conductivity. However, YSZ based devices have to be operated at 1000⁰C or higher²⁸ to reach an appreciable level of ionic conductivity and such a high operating temperature leads to complex materials problems

Electrical characterization of ZrO_2 thin films is necessary to find its applicability in electronic and fuel cell industry. The estimation of ohmic resistance of a thin film requires some special precautions due to two specific problems as stated in literature²⁸. First, the ohmic resistance of thin layer cannot be treated as a discrete quantity, but rather as a sum of ohmic resistance of the

thin layer and the substrate on which the thin layer is deposited. Second, the electrical contact made by deposition of metal is not complete ones. Such an imperfection of the electrical contact can dramatically influence the magnitude of the measured ohmic resistance in the case of layer thickness of $\sim 100 \text{ nm}$ ²⁸.

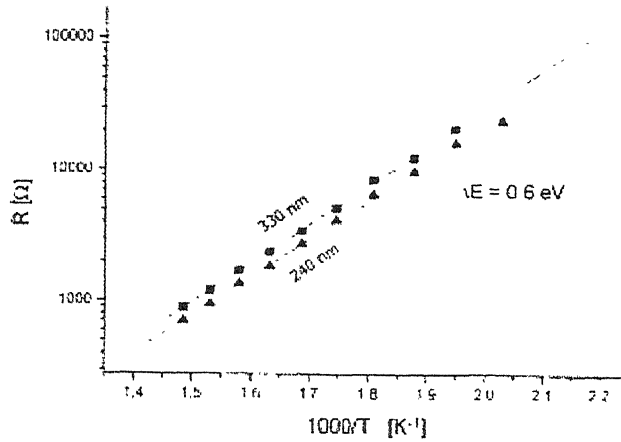


Fig. 1.7 Temperature dependence of resistance for YSZ thin films of different thickness.

Kundracik et. al.²⁸ made the impedance measurements on YSZ films on n-doped Si in the frequency range of 10Hz-1MHz at temperatures 493-673 K. The ohmic resistance of the films decreases as the temperature increases due to the increased mobility at elevated temperatures. Thus it is evident that the resistance of the film decreases as the temperature increases following the Arrhenius equation as shown in figure 1.7.

The transport mechanism of YSZ thin films prepared by MOCVD was studied by Sung-Yong Chun et. al.²⁹. The ionic conductivity of the specimens was evaluated by complex impedance in the frequency range 10Hz to 100MHz. The conductivity was measured between 600 and 900 °C. The impedance spectra¹⁶ of ZrO_2 :16%-Sc nanocrystalline thin films show only one semicircle (figure 1.8 (a)) as found in 3mole % Y_2O_3 doped ZrO_2 single crystals²⁹ (figure.1.8 (b)).

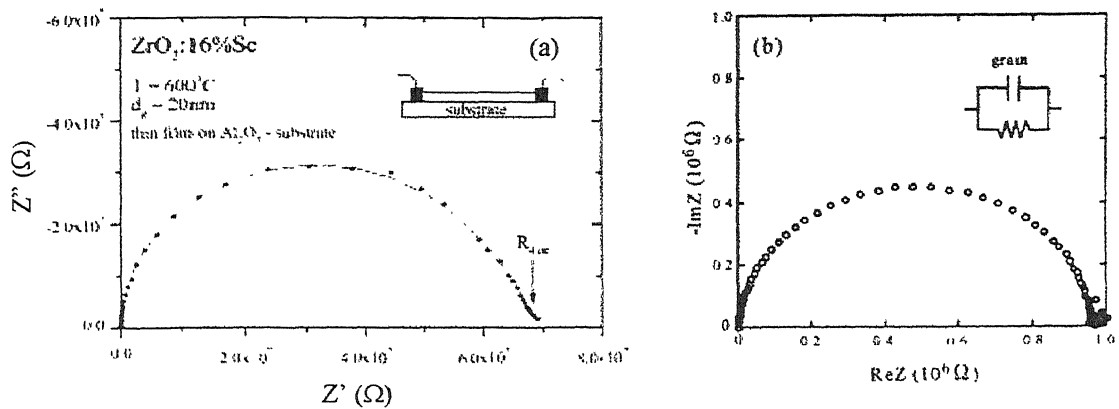


Fig. 1.8 Cole-Cole plots of (a) ZrO_2 :16%Sc thin film on Al_2O_3 substrate, and (b) 3 mole% YSZ single crystal

The thin film sample (a) shows only one semicircle due to the overlapping of grain and grain boundary conductivity while the single crystal sample (b) shows only one semicircle due to the absence of any grain boundary effect. Chun et. al²⁹ also found that the substrate and film thickness also effects the conductivity and hence activation of the films as shown in figure 1.9.

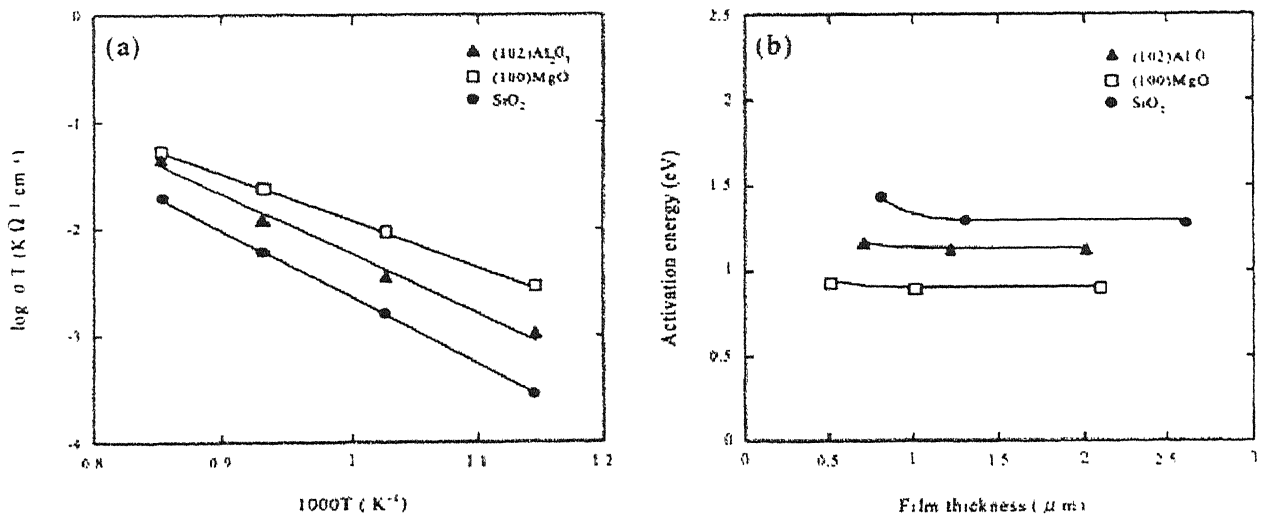


Fig. 1.9 (a) Arrhenius plots of conductivity and (b) film thickness dependence of activation energy of 4.9 mole% Y_2O_3 doped ZrO_2 thin film deposited on different substrates.

The microstructural result obtained by Chun et. al. suggest that the different values of activation energy of the films deposited on each substrate can be ascribed not to the grain size but other parameters such as thermal and crystallographic mismatch between film and substrate. It has been found that the conductivity of the films can be changed if the oxygen vacancy conduction in the grain boundary of the film is increased or decreased. Thus oxygen partial pressure has an effect on the conductivity of zirconia. It is also found that the oxygen partial pressure has an effect on the conductivity of Gd_2O_3 doped CeO_2 .

Impedance of $\text{La}_{0.7}\text{Sr}_{0.3}\text{MnO}_3/\text{YSZ}/\text{La}_{0.7}\text{Sr}_{0.3}\text{MnO}_3$ as a function of frequency has been studied by Charpentier et. al.³⁰ at a temperature of 850°C keeping the oxygen partial pressure at 0.21 atm. The effect of oxygen partial pressure on conductivity has been studied by Kosacki et. al.¹⁶ in some detail. He and his coworkers found an enhancement of about two orders of magnitude (at 600°C) in the ionic conductivity of nanocrystalline YSZ thin film. The enhancement in the conductivity of nanocrystalline YSZ was attributed to the decrease in the activation energy from 1.23 to 0.93 eV for macro- and nanocrystalline material, respectively. This decrease was attributed to extended interfacial area in the nanocrystalline material and the unique defect thermodynamics, which determine the hopping energy for oxygen ions.

Yeh et. al.³¹ found a decrease in the activation energy from 0.58 to 0.35 eV in the low temperature regime for vapor-deposited YSZ thin films on thermal annealing. Two different activation energies (0.6 and 1.08 eV) were observed for two different temperature domains. This difference was attributed to two different mechanisms. The two mechanisms were speculated to be the migration of free oxygen vacancies at low temperatures and the dissociation of oxygen-vacancy-yttrium pairs at temperatures above the transition point.

1.5 The sol-gel process

Sol-gel technology is a very simple but a very useful technique developed to prepare metal-oxide fibers, monoliths, microspheres, thin films and fine powders etc. The sol-gel prepared films have large number of applications such as protective and antireflection coatings, catalysts, piezoelectric devices, wave-guides, and coating of optical lenses.

The sol-gel process offers the following advantage over the conventional processing methods

- 1) High purity of the products is obtained.
- 2) Mixing takes place at the molecular level so that one can get molecular level homogeneity in the multicomponent materials.
- 3) Lower processing temperature leading to low energy requirements
- 4) Film thickness can be controlled by varying the sol concentration and the number of the coatings.
- 5) Dopants can be easily introduced for desired electrical and physical properties.

However it has some disadvantages

- 1) Long processing time
- 2) Residual fine pore after drying and annealing
- 3) Large shrinkage in films during heating and annealing, which may cause crack formation in the film.

Two type of sol-gel processing are generally used

a. Colloidal Processing

Particles of size 1-1000 nm are used. They form a gel network and subsequently sinter to yield a continuous film

b. Polymeric Processing

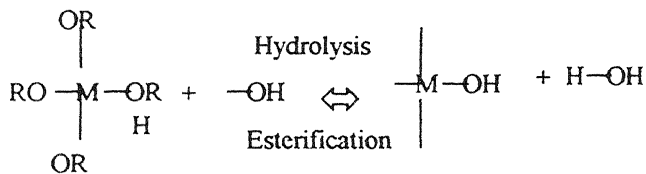
Different metal alkoxides $M(OR)_x$ are used as precursors. In the sol-gel synthesis, $M(OR)_x$ is mixed with water and appropriate solvent (usually an alcohol). A small amount of acid or base is added to catalyze the reaction. To avoid or minimize self-condensation, some metal salt like chloride, nitrate and acetate are used. Alcohol, chloride, nitrate and acetate play an important role in determining the thickness and volume shrinkage. During polymeric gel formation, hydrolysis and condensation reactions take place simultaneously.

1.5.1 Chemistry of sol-gel processing

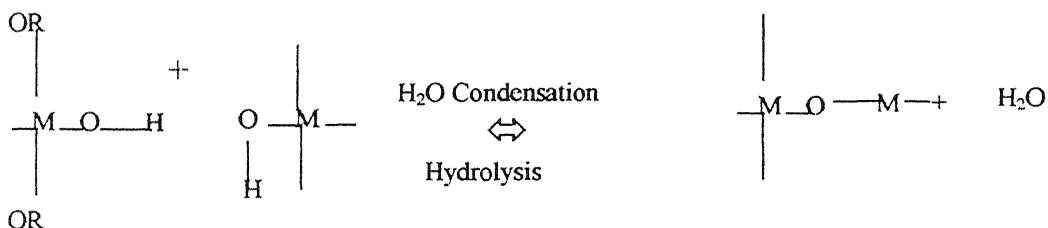
The reactions, which lead to the formation of a gel from the sol, are of two types

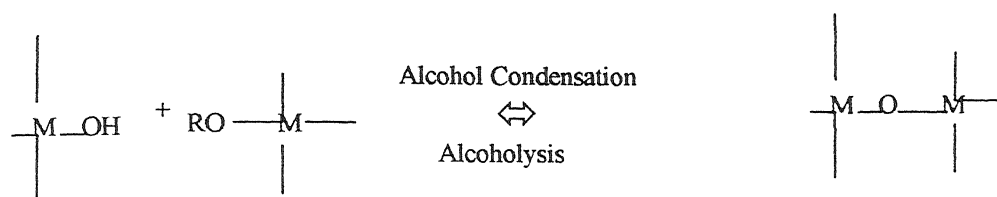
a) hydrolysis and b) condensation

(1) Hydrolysis Reaction: By this reaction, the alkoxy group is replaced by an $-OH$ group as under.



(2) Condensation Mechanism: The $-OR$ ($R = \text{alkyl or H}$) group is eliminated and metal oxygen metal ($M-O-M$) linkages form as under:





The sol is eventually transformed into a 3-D network (gel) by the elimination of water or some other group like alcohol. This process is known as gelation. The physical characteristics such as volatility, solubility and hydrolysis rate of oxides depends on the chemistry of metal and alkyl group ³². Water is a by-product of the condensation reaction. Since hydrolysis and condensation are reversible, increasing the amount of water inhibits the condensation reaction.

For Zr-n-propoxide as a precursor the main reactions are shown below



Zirconium alkoxide form hydrous zirconium oxide like $\text{ZrO}_2 \cdot n\text{H}_2\text{O}$ or $\text{ZrO(OH)}_2 \cdot n\text{H}_2\text{O}$ and/ or hydrated polymeric species having a number of Zr-O-Zr bridges. Hydrolytic polycondensation reactions of zirconium alkoxides result in the formation of Zr-O-Zr bridges based on a octahedrally six coordinated zirconium.

1.6 Spin coating process

Various coating techniques such as dip coating, spray coating and spin coating are available for the preparation of sol-gel thin films. In spin coating process the substrate spins around an axis perpendicular to the coating area. Some variable process parameters involved in spin coating are (a) solution viscosity, (b) solid content, (c) angular speed and (d) spin time. These

process variables determine the film thickness as well as film quality. The film-forming process is primarily driven by two independent parameters – viscosity and spin speed. Usually thin films are formed by spin coating. For thicker films, high material viscosity, low spin speed, and a short spin time are needed. However, these parameters can affect the uniformity of the coat. Dubey³³ observed an increase in the film thickness of PZT films by addition of a vinyl polymer (PVP). However, multiple coatings are still preferred for a thicker film.

Spin coating is divided into four stages: deposition/dispense, spin-up/spread cycle, spin-off and evaporation. The final thickness of the spin-coated layer also depends on the rate of evaporation of solvent. The final thickness is given by the semi-empirical formula as follows³⁴.

$$h = \left(1 - \frac{m_A}{m_{A_0}} \right) \left(\frac{3\eta e}{2m_{A_0} \omega^2} \right)^{1/3} \quad \text{----- (1)}$$

where, h = final thickness, ω = angular speed,

m_A = mass of volatile solvent per unit volume,

m_{A_0} = initial value of m_A ,

e = evaporation rate of the solvent.

During deposition, the excess of liquid is dispersed on the surface. The quality of the film depends on whether the solution wets the surface completely or not. If not then incomplete coverage can result in poor quality of film. In the spin-up stage, centrifugal force drives the liquid radially outwards. During spin-off stage i.e., when the substrate is spinning at a constant rate, excess liquid flows to the perimeter and film thinning takes place thus giving a uniform film thickness. Finally, evaporation takes place dominated by drying in which the volatile solvents are removed and the viscosity of sol rises and so the coating transforms into a 'gel'. Stages of the spin coating³⁵ process can be seen in the figure (1.10).

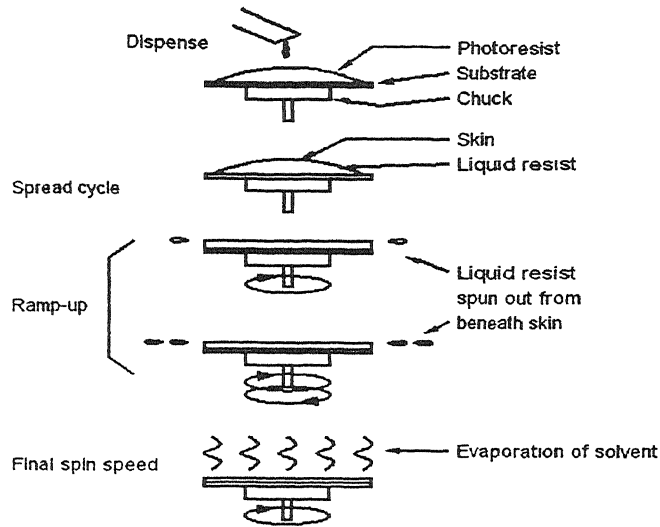


Fig.1.10 Scheme describing a basic spinning process

After spinning the film is dried and then baked or fired at a desired temperature, depending on the application when further reduction in thickness takes place³⁶.

1.7 Impedance spectroscopy

Impedance Spectroscopy (IS) is a relatively new and powerful technique of characterizing many of the electrical properties of materials and their interfaces with electronically conducting electrodes. Impedance spectroscopy was first applied by Baurele³⁷ to investigate solid electrolyte³⁸, electrode materials and the interfacial regions between them. Since dc measurements involve polarization effects, ac measurements are used to extract the dc conductivity. The general approach is to apply an electrical stimulus to the electrode and observe the response. The impedance is directly measured in the frequency range by applying a single frequency voltage to the interface. The impedance analyzer directly measures the amplitude of the

Impedance $|z|$ and the phase shift θ .

An impedance analyzer is useful to derive many parameters of materials such as dielectric constant, conductivity, mobility of charges etc. Capacitance of the electrode, adsorption reaction rates and constants pertaining to an electrode material interface are also obtained.

The $|z|$ and θ values are plotted in a complex impedance plane with $|z|\cos\theta$ (z') as x-axis and $|z|\sin\theta$ (z'') as y-axis. The plot is popularly known as Cole-Cole plot.

1.7.1 Complex impedance plane analysis

Impedance of a circuit is the ratio of voltage to the current as Ohm's law is followed well in the time domain. If the voltage function is given by $V(t) = V_M \sin(\omega t)$, with a single frequency $f = \omega/2\pi$, is applied to a cell and the steady state current $I(t) = I_M \sin(\omega t + \theta)$ is measured. then, θ = phase difference between the voltage and the current. Phase difference (θ) is zero for purely resistive behavior. The complex impedance now can be written as

$$\text{Complex Impedance, } z^*(\omega) = \frac{v(t)}{i(t)} \quad \text{----- (1)}$$

Its magnitude is $|z(\omega)| = \frac{V}{I_m(\omega)}$ and phase angle is $\theta(\omega)$.

Impedance is a more general concept than resistance because it takes phase differences into account.

The complex impedance $[z^*(\omega)]$ at an applied frequency is written as:

$$z^*(\omega) = z'(\omega) + jz''(\omega) \quad \text{----- (2)}$$

where, z' and z'' are the real and imaginary parts of the complex impedance respectively which also can be represented as

$$z' = |z|\cos\theta \text{ and } z'' = |z|\sin\theta$$

The phase angle $\theta = \tan^{-1}(z'/z'')$ and the modulus (or magnitude) is

$$|z| = [(z')^2 + (z'')^2]^{1/2} \quad \text{----- (3)}$$

This defines the Argand diagram or a complex plane. In general, z is frequency dependent and is measured by impedance spectroscopy as a function of ν or ω over a wide frequency range.

In order to analyze the physical processes occurring in the ionic solids, semiconductors or mixed electronic-ionic solids and insulators, the net complex impedance can be represented with the combination of resistors and capacitors. If the Cole-Cole plot is obtained as a semicircle then the diameter of the semicircle is the dc resistance, which is independent of the frequency.

Simple RC circuits common to impedance spectroscopy and typical z and y plots are shown below:

(A) Pure resistor circuit(R)³⁹

Complex impedance for a pure resistor can be written as

$$z^* = z' + jz'' = R \quad \text{----- (6)}$$

Thus, $z' = R$

and $z'' = 0$

(B) Pure capacitor circuit (C)

Complex impedance for a pure capacitor can be written as

$$z^* = z' + jz'' = \frac{1}{j\omega C} = -\frac{j}{\omega C} \quad \text{----- (7)}$$

where, ω = angular frequency

Therefore, $z' = 0$ and $z'' = -\frac{1}{\omega C}$

(C) Series combination of R and C

For a series combination of R and C,

$$z^* = R + \frac{1}{j\omega C} = R + j\left(-\frac{1}{\omega C}\right) \quad \text{----- (8)}$$

Comparing the real and imaginary parts,

$$z' = R \text{ and } z'' = -1/\omega C$$

(D) Parallel combination of R and C

Net complex impedance for RC parallel combination can be represented as follows:

$$z^* = \frac{R\left(\frac{1}{j\omega C}\right)}{R + \frac{1}{j\omega C}} = \frac{R}{(1 + j\omega RC)} \quad \text{----- (9)}$$

By rationalizing the denominator we get

$$z^* = z' + jz'' = \left(\frac{R}{1 + \omega^2 R^2 C^2}\right) + j\left(-\frac{\omega R^2 C^2}{1 + \omega^2 R^2 C^2}\right) \quad \text{----- (10)}$$

Comparing real and imaginary parts, we get

$$z' = z \cos \theta = \frac{R}{1 + \omega^2 R^2 C^2} \quad \text{----- (11)}$$

$$\text{and, } z'' = z \sin \theta = -\frac{\omega R^2 C^2}{1 + \omega^2 R^2 C^2} \quad \text{----- (12)}$$

Eliminating ω from these two equations, we have

$$(z')^2 + (z'')^2 = \frac{R^2}{1 + \omega^2 R^2 C^2} = Rz' \quad \text{----- (13)}$$

This equation can be written in the form of

$$\left(z' - \frac{R}{2}\right)^2 + (z'')^2 = \left(\frac{R}{2}\right)^2 \quad \text{----- (14)}$$

Equation (14) represents a circle with radius $=R/2$ and center at $(R/2, 0)$. The value of R is the diameter of a circle, which is called the dc resistance of the sample. The impedance plot is shown in figure (1.11).

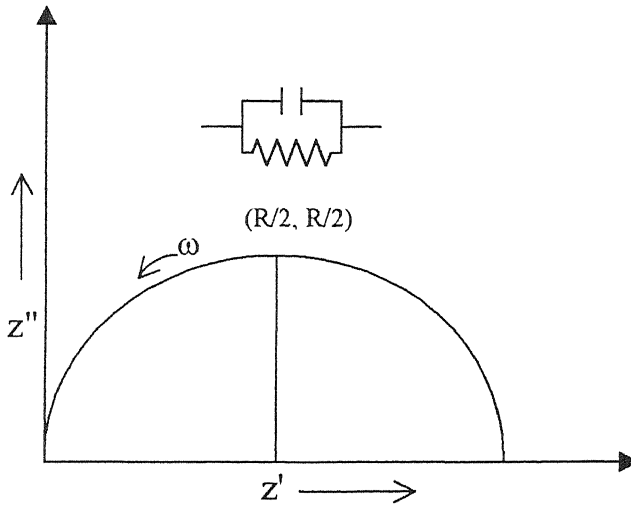


Fig.1.11 Impedance plot for parallel combination of a resistor and capacitor

The admittance value can also be determined from the impedance value as discussed below

$$\text{Admittance, } Y^*(\omega) = Y' + jY'' = 1/Z^*(\omega) \quad \text{----- (15)}$$

where, $Y' = 1/R = Y \cos \theta$ and $Y'' = \omega C_p = Y \sin \theta$ [C_p = measured capacitance].

The dielectric constant is,

$$k^* = k' - jk'' = \frac{Y''}{\omega C_0} - j \left(\frac{Y'}{\omega C_0} \right) = \left(\frac{\omega C_p}{\omega C_0} \right) - j \left(\frac{1}{\omega R C_0} \right) \quad \text{----- (16)}$$

$$\text{Therefore, } k^* = \frac{C_p}{C_0} - j \left(\frac{1}{\omega R C_0} \right) \quad \text{----- (17)}$$

where, C_0 is the capacitance with no dielectric material.

The dielectric loss tangent is given as:

$$\text{Loss tangent (D)} = \tan \delta = \frac{k''}{k'} = \frac{\left(\frac{1}{\omega RC_0} \right)}{\left(\frac{C_p}{C_0} \right)} \quad \text{----- (18)}$$

Therefore,
$$D = \frac{1}{\omega RC_p} = \frac{1}{2\pi f C_p} \quad \text{----- (19)}$$

where, f is the frequency.

In polycrystalline ceramic sample, we generally get depressed semi-circles. By finding out their diameter we get an idea about their dc resistivity. In these solids there is ionic conduction due to both grain and grain boundary effects. So, there are two semicircles with an arc due to electrode effect. Bauerle³⁷ has showed that for zirconia with platinum electrodes the individual polarization of grain interiors (g_i), grain boundaries (g_b), and electrode-electrolyte interfaces could be resolved in the admittance plane. He also presented a circuit equivalent to this arrangement. In this circuit, the elements corresponding to grain interiors (g_i), grain boundaries (g_b), and electrode (e) are connected in series.

1.8 Statement of the problem

It is quite evident from the previous sections that thin films of ZrO_2 are important both technically as well as due to their scientific interest. Zirconia ceramics stabilized by MgO , CaO , CeO_2 , Y_2O_3 etc have been very well studied. There are several other rare earth R_2O_3 type oxides which are known to stabilize the high temperature phases of ZrO_2 , but are not well studied. Gd_2O_3 is on such rare earth oxide.

Several reports have been dedicated to the study of corrosion resistance behavior of zirconia thin films on stainless steel but rarely anyone has worked on the electrical properties of such films.

In a previous work⁴⁰ carried out in our laboratory, certain ambiguities in the results were found.

In this work, it is planned, therefore, to prepare thin films of pure and Gd_2O_3 stabilized ZrO_2 on stainless steel substrates and study the phases, microstructures and electrical properties by impedance spectroscopy. To clarify the issues that emerged from the earlier work it is also planned to vary the concentration of Gd_2O_3 and study its effect on the properties of the films.

Chapter 2.

Experimental procedure

2.1 Sol preparation

Solutions containing a source of Zr(IV) and varying amounts of Gd(III) were prepared using Zr-IV-propoxide and Gd_2O_3 . The chemicals used to make the ZrO_2 sol have specifications as given in table 2.1 below:

Table 2.1 Chemicals used in the preparation of thin films

| Precursor | Source | Mol. Wt. | Density (g/cm^3 at $20^\circ C$) | Assay |
|------------------------|--------------------|-----------------|--|-------------------|
| Zr-IV-propoxide | Fluka Chemika | 327.58 | 1.05 | 70% (in propanol) |
| Gadolinia | Kemphasol | 362.5 | 7.407 | 99% |
| Ethyl Alcohol | Merck | 46.07 | 0.794 | 99.8% |
| Acetic Acid | Thomas Baker | 60.05 | 1.049 | 99.8% |
| PVP | | 111.00(monomer) | | 94.1% |
| Triple Distilled Water | Prepared in lab | 18 | 1 | |
| Nitric Acid | S-D Fine Chemicals | 63.01 | 1.4 | 69-71% |

Singh⁴⁰ found that with 0.2 M concentration of the sol, good and shining films having a thickness in the range 0.4 to 0.9 μm could be obtained after heat treatment. So, the present work was restricted to films prepared using 0.2M sol.

2.1.1 Apparatus used

Apparatus used in the experiments are 10, 25 and 50ml beakers, pipettes, 10 ml measuring cylinders, 5 ml plastic syringe and teflon coated magnetic needle. The glass wares were cleaned and dried with the following steps:

- (i) Cleaned with dilute nitric acid
- (ii) Cleaned with wetting and cleaning agent solution (Labogent, S.D Fine Chemicals)
- (iii) Cleaned with distilled water
- (iv) Cleaned with acetone
- (v) Dried at 100°C in oven overnight

2.1.2 Procedure for sol preparation

The procedure of preparing the sols is outlined in the flowchart given in figure (2.1)

All the sols were prepared inside the glove box maintained at a relative humidity $\leq 30\%$. This level was obtained by pacing the dried silica gel inside the glove box for 3-4 hours. The silica gel was dried at $\sim 150^\circ\text{C}$ overnight to get required moisture-absorbing capability. It is necessary to maintain a low humidity level because zirconium-n-propoxide reacts with moisture in air and gets gelled immediately. The calculations and the actual amounts of the various ingredients used in sol preparation are given in Appendix-1.

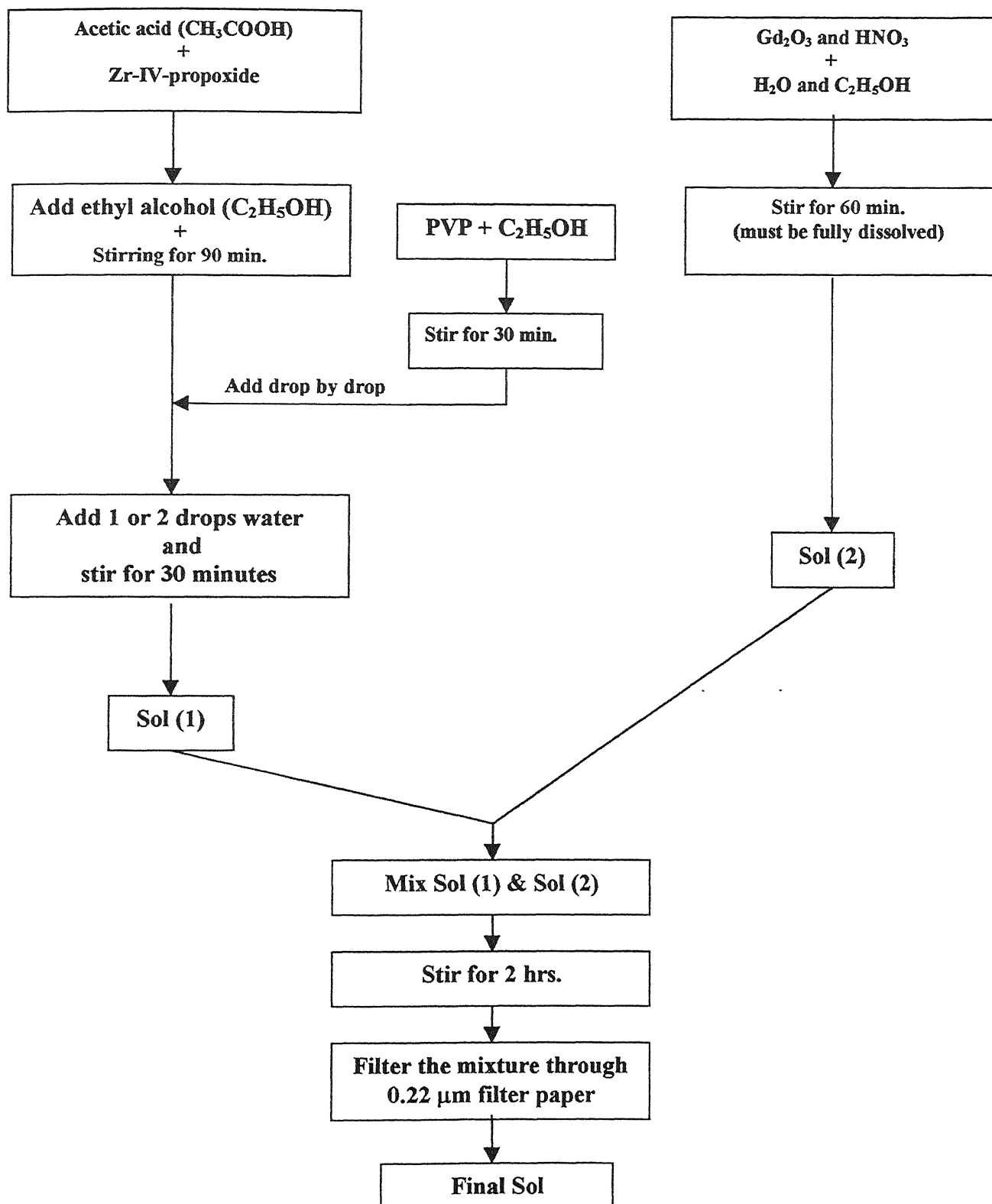


Figure 2.1 Flow chart for sol preparation

A measuring cylinder, two pipettes, a 10ml beaker, two 25 ml beakers and a 50 ml beaker (containing clean and dried magnetic bar) were placed inside the glove box. The required amount of ethyl alcohol was poured in the measuring cylinder and covered by aluminum foil. All the required amounts of acetic acid, zirconium-n-propoxide were weighed in the glove box and taken in a 50 ml beaker. However, the addition sequence is very important. It is imperative that zirconium-n-propoxide should be added to acetic acid and not the other way round else it will form particles³². To the above solution 1/4th(~2.5ml) of the total amount of ethyl alcohol was added and the mixture was stirred for 90 minutes. After 60 minutes of stirring measured amount of PVP was dissolved in 1/4th(~2.5ml) of the total amount of ethyl alcohol in a 25 ml beaker and stirred for 30 minutes. Then the PVP solution was added drop by drop to Zr-n-propoxide bearing solution and further stirring was done for 30 minutes. The resulting solution turns milky but clears upon addition of 1 to 2 drops of water (this is solution -1). PVP was added to slow the condensation rates during film drying and densification⁴¹. By minimizing the condensation rate, the stress developed in the film can be minimized and crack free film can be grown²⁴.

In another beaker, all the required amount of HNO₃ and water was taken and to it measured quantity of Gd₂O₃ and 1/4th(~2.5 ml) of the ethyl alcohol was added. The mixture was stirred for 60 minutes or till the solution becomes transparent (This is solution 2). This was added to solution (1) and the mixture was subjected to rigorous stirring for another 2 hours on a magnetic stirrer to ensure that every ingredient is mixed homogeneously. It was found that mild heating during stirring enhanced the formation of transparent sol. This sol was filtered through 0.22 µm filter paper with the help of a syringe. This ensured the removal of coarse particles that may remain in the sol. The final sol was transferred in 25 ml polystyrene bottles, properly labeled and kept in a cool dry place to increase shelf life. Using the above procedure, pure zirconia sol and 1.75, 2.5, 4, 5, 8, 9 and 11 mole % gadolinia-doped zirconia sols were prepared. Coating is done after storing for 4-5 hours. It is observed that the stability of the sol depends on the addition

of HNO_3 . The pure ZrO_2 sol has the least stability while some of the doped sols with HNO_3 content were found to be stable even after 6 months. Generally, the average sols gel often after 30–40 days or more of preparation.

2.2 Substrate preparation

2.2.1 Substrate

Singh⁴⁰ experimented on the sticking behavior of ZrO_2 sol on Pt, glass, Ag and stainless steel substrates. He found that ZrO_2 sol tends to stick to 304 stainless steel. Thus the present work was started with 1.5 cm x 1.0 cm 304 stainless steel as substrate.

2.2.2 Polishing

Initially the substrates were polished with 1/0, 2/0, 3/0, 4/0 emery papers and then with 0.05 μm fine alumina paste on a polishing cloth in the above sequence to give a mirror like finish to the substrate surface. Whenever the emery papers is changed i.e., coarse to fine, the substrate is rotated by 90° and polished until the coarse scratches are replaced by the fine scratches and a mirror like finish is obtained.

The whole procedure takes 2-3 hours for a steel surface to give a mirror like finish due to its high hardness. It was found that the sol does not stick properly to heavily polished steel substrate so further work was done on 1/0 and 2/0 polished steel substrates.

2.2.3 Cleaning

Proper cleaning of the substrate surface is a must after polishing to ensure uniform defect-free deposition. The substrate surface must be free from dust and other particulate matter. It must set the sol uniformly during film deposition.

The substrates were initially rubbed with detergent powder and then the steps described below was followed to clean the substrates:

- (i) Ultrasonication in water for 5 minutes.
- (ii) Ultrasonication in dilute detergent ("Labogent", S. D. Fine Chemicals) for 5 minutes.
- (iii) Ultrasonication in distilled water twice for 5 minutes each.
- (iv) Ultrasonication in ethyl alcohol for 5 minutes.
- (vi) Ultrasonication in acetone for 5 minutes
- (vii) Drying in oven at $\sim 100^{\circ}\text{C}$ for 3 to 5 minutes.

These steps ensure the removal of polishing debris and make the substrate surface grease free. This increases the wettability and binding of the sol-gel coating on the surface of the substrate. After cleaning each substrate was kept on a tissue paper inside a clean polystyrene box. Also, every substrate was stored separately to avoid marks or scratches made on the surface by friction of many substrates.

2.3 Thin film deposition

In the present work spin coating technique was used to deposit thin films on polished stainless steel substrates. This process is most suited for sol-gel deposition because the process involves simple fluid flow and evaporation behaviors that generally give rather uniform coating. For thickness measurement of the thin films by surface profilometer, a small area of the substrate was covered with a teflon tape to make a step on it. The undoped zirconia and gadolinia-doped zirconia sols were deposited on steel substrates using a fully automatic spin coater (Photo Resist Spinner, Ducom). The substrate was kept at the center of the chuck having a small hole (~ 2 mm diameter) at its center which is connected to a vacuum pump. When vacuum is 'ON', the vacuum is created at the hole and the substrate is held firmly on to the wheel. The

speed of the spinner was fixed at 4000 rpm and the time of spinning is set for 30 seconds to get uniform spreading of the sol. One drop of the sol was placed onto the substrate during the initial few seconds of spinning by using a dropper to coat a single layer. Initially drying temperatures of $\sim 125^{\circ}\text{C}$ and 200°C for 2 minutes per coat was used, but it was found that the films dried at 200°C resulted in crack formation so for further work $\sim 125^{\circ}\text{C}$ was used as the drying temperature. The drying temperature was maintained on a hot plate by setting it at 80% power. Multiple coatings were applied to get a film of desired thickness by repeating the above step. For our purpose 10 and 15 layers were deposited, but it was seen that 15 layered film did not show a good step so further work was done on 10 layered film. After the final coating, the film was inserted in a tube furnace heat treated at 500°C for a soaking period of 10 minutes because the films fired at higher temperatures get oxidized. The heating and cooling rate was fixed at 300°C/hr to get a crack free film.

Optical microscopic observation was carried out to find the film quality. The absence of electrical continuity between the bare and the coated parts of the substrate also confirmed the presence of film. On the stainless steel substrate, the film was found to form when the substrate is partly polished only up to 2/0-emery paper. Film does not form on the substrate polished further⁴⁰. Hence in all the experiments described hereafter the steel substrate polished to 2/0-emery paper was used. It is believed⁴⁰ that the presence of the fine chromium oxide (Cr_2O_3) coating on the stainless steel may also be acting as an adhering layer to hold the film.

2.4 Characterization of films

2.4.1 Microscopy of films

An optical microscope (ZEISS, West Germany) under reflected light at magnifications 50x, 100x and 200x was used to examine the quality of the thin films. Presence of

any cracks after heat treatment can be very easily seen at 50x, 100x and 200x magnifications. A camera attached to the microscope was used to take the photographs of the films.

A scanning electron microscope (JEOL 840A, Japan) was initially used to observe the microstructure of the samples. No microstructure was visible at a magnification of 9000x. Thus AFM phase imaging was done to get an idea of the grain size.

2.4.2 Atomic Force Microscopy (AFM)

AFM of the films was done by an atomic force microscope (MI, Picoscan-4). Both surface roughness and grain size was determined from the topographic and phase images. AFM generally uses a feedback mechanism (figure 2.2) to regulate the force on the sample.

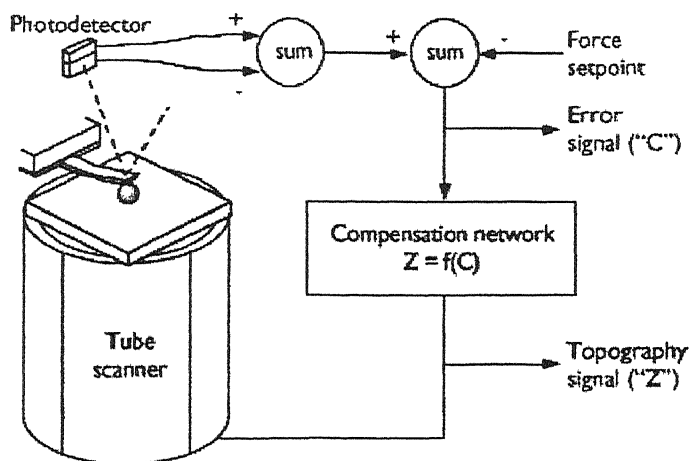


Fig. 2.2 The AFM feedback loop

In AFM two different modes⁴² are generally used for scanning the surface (a) contact mode and (b) non-contact mode. In contact mode the force applied is in the range of 10^{-8} to 10^{-9} N while the same for the non-contact version is 10^{-12} N. Thus by using different modes of operation one can find the topography as well as elasticity of the sample which in turn gives an idea of the grain size. A compensation network (which is a computer program) monitors the cantilever deflection and keeps it constant by adjusting the height of the cantilever. For our samples a Si tip 10-15 Å diameter was used as a probe. Various scan areas ranging from 150 nm x 150 nm to 2500 nm x

2500 nm was used to get the topographic and phase images. The root mean square (RMS) roughness values were determined by using picoscan software.

2.4.3 Thickness measurements

The thickness of the films has been determined using Surface Profilometer Alfa step 100 (Tencor Instruments, USA). The instrument scans a diamond stylus over the sample and directly measures the step height between the substrate and the film. A small area of the substrate covered with teflon tape during coating was removed to provide a sharp step for this measurement. The stylus of the surface profilometer scans the bare substrate and then scans the film surface through the sharp step. A recorder attached with the profilometer produces the plot of the thickness measurement. For a baseline correction, the step up (\Uparrow) or step down (\Downarrow) button is pressed a number of times as needed.

2.4.4 X-ray diffraction

The X-ray diffraction patterns of pure and the doped zirconia thin films were collected to determine the phases and crystallinity. A fully computerized X-ray diffractometer (Rich Seifert Iso-Debyeflex-2002, Germany) has been used with a $\text{CuK}\alpha$ radiation ($\lambda=1.5405\text{\AA}$) having a Ni monochromator for probe. The Following operating conditions have been used.

Table 2.2 Operating parameters for XRD

| Parameter | Values |
|----------------------|-----------------------------------|
| Accelerating voltage | 30 kV |
| Accelerating current | 20 mA |
| Scanning speed | $3^\circ/\text{min}$ in 2θ |
| Time constant | 10 sec |
| Range (CPM) | 5k |

All X-ray patterns were recorded at room temperature. The value of the inter-planer spacing (d) is used to calculate the index of an X-ray line, using the Bragg's relation,

$$2d \sin \theta = n \lambda$$

where, θ = Bragg (or diffraction) angle,

n = order of diffraction (= 1)

λ = X-ray wavelength (1.54 Å).

d = interplanar spacing.

By diffraction patterns gives intensity Vs 2θ (angle in degrees) plots by which 2θ values can be obtained corresponding to the peaks maximum and this when compared with the standard data gives the phase(s) present. The relative intensities of the peaks can be measured with reference to a maximum peak, which is called 100 percent peak.

To obtain the diffraction pattern, the substrate with the film is placed in a perspex holder and fixed with a small amount of plasticine. Then it is pressed down with the help of a glass slide to make it horizontal to the sample holder.

The table 2.3 shows the standard 2θ values corresponding to the peaks of the stainless steel.

Table 2.3 Standard XRD data of stainless steel

| 2θ (deg) | Intensity (%) | hkl (plane) | Phase |
|-----------------|---------------|-------------|---|
| 43.620 | 100 | 111 | CrO. ₁₉ FeO. ₇ NiO (PDF 33-0397) |
| 50.836 | 45 | 200 | |
| 74.770 | 26 | 220 | |
| 90.791 | 30 | 311 | |
| 96.071 | 12 | 222 | |
| 118.315 | 3 | 400 | |

The XRD pattern of the substrate (stainless steel) is taken between 20°-80° in 2 θ range and observed three peaks (at 43.78°, 50.85° and 74.93°). This confirms that the substrate is austenitic steel, which is also called 304 stainless steel.

2.4.5 Deposition of Au-Pd top electrode on the film

Hummer (VI-A) sputtering unit (Anatech Limited, VA) with Au-Pd target in a shape of circular disc was used to deposit Au-Pd top electrode on ZrO₂ thin films. A mask with several circular holes (~ 0.5 mm diameter) was kept on the film. So only the spare small circular areas get deposited with Au-Pd electrode. The bare steel substrate acts as the bottom electrode.

For sputtering, following conditions were used:

Vacuum in sputtering chamber = 80 mT (milliTorr),

Plasma discharge current = 10 mA (milliAmpere),

Voltage control setting = 3.5 to 4.5,

Total time for sputtering = 15 minutes.

The samples were annealed in the furnace at 250°C for 5 minutes after annealing to have better adhesion between the electrode and the film surface.

2.4.6 Electrical measurements

2.4.6.1 Sample configuration

Pure and Gd₂O₃ doped thin films were deposited on polished stainless steel substrate for electrical measurements. After heat treatment at 500° for 5 minutes, Au-Pd top electrodes (0.5 mm diameter) were deposited through a mask by dc sputtering. The metal oxide metal (MOM) configuration is given in figure 2.3.

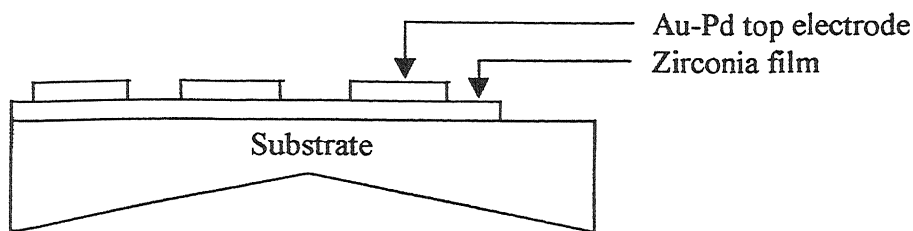


Fig. 2.3 MOM capacitor configuration showing substrate, film and Au-Pd top electrode

2.4.6.2 Thin film heater

For all the electrical measurements, a special kind of sample holder was used to take data at different temperatures. The sample holder is shown in figure 2.4

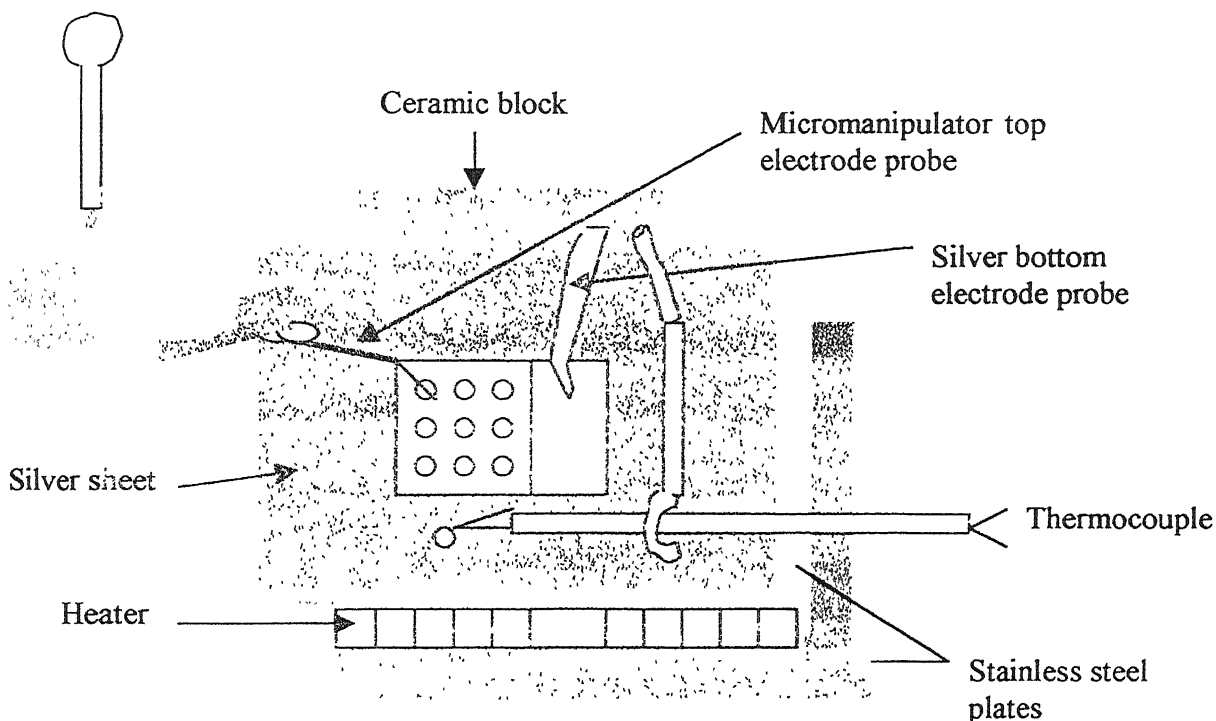


Fig. 2.4 Sample holder for electrical measurements

A heating coil used in the domestic iron is sandwiched between two mica and stainless steel plates. The top stainless steel plate is partially covered with a silver foil of about 0.2 mm thickness. An adjustable silver probe is fixed on the top plate. This probe contacts the uncoated surface of the substrate and forms the bottom electrode. A micromanipulator with a tungsten tip

is used to make contact with the top electrode while viewing under an optical microscope. A chromel alumel thermocouple (K-type) is kept close to the film to measure the sample temperature. The maximum temperature attainable by the sample holder is 300°C. For electrical measurements, the maximum temperature used in the present work is 280°C. A temperature controller, an ON/OFF relay and a digital panel meter (DPM) was attached to the thermocouple and the heater to control the temperature.



2.4.7 Impedance analysis

An impedance analyzer (Model HP 4292A LF) with a HP 1607A test fixture is used for electrical measurements. The impedance Z , phase angle θ , dielectric loss (D) and capacitance (C) of the films were measured as a function of frequency between 1kHz to 7 MHz at different temperatures ranging from 25°C to 280°C. The built in frequency synthesizer is used to generate frequency in the range of 5 Hz to 13 MHz with 1 mHz resolution. The a.c. voltage peak amplitude and the frequency range over which measurements are desired are set while calibrating the instrument. There are two display modes 'A' and 'B', which can be selected to measure the desired quantities.

The complex impedance z^* consists of real and imaginary parts z' and z'' respectively. The oscillation level is fixed at 0.05V (50mV). The Au-Pd top electrode has an area of $0.196 \times 10^{-6} \text{ m}^2$ (diameter is 0.5mm). Impedance plot, popularly known as Cole-Cole plot was plotted with the positive x-axis containing real part of the impedance (z' or $|z|\cos\theta$) and the positive y-axis containing imaginary part of the impedance (z'' or $|z|\sin\theta$).

Table 2.4: The displays 'A' and 'B' of impedance analyzer

| Display 'A' Function | Display 'B' Function |
|---|---|
| $ z $: Absolute value of Impedance $ Y $: Absolute value of Admittance | θ (deg/rad) : Phase Angle |
| R : Resistance | X : Reactance |
| G : Conductance | B : Susceptance |
| L : Inductance C : Capacitance | Q : Quality factor D : Dissipation factor R : Resistance G : Conductance |

The equivalent modes are auto,  (series) and  (parallel).

For dielectric measurements, the display can be set to 'C' and 'D' to calculate dielectric constant (k) and loss measurements. These measurements were taken as a function of frequency.

2.4.8 Impedance data analysis

The sample is placed on the sample stage covered with a cardboard box and heated to the test temperature. Now, the impedance analyzer (IA) is calibrated by following the steps given in Appendix-2.

After calibration, the spot frequency (f) is manually changed in steps from 1kHz to 7 MHz and values of f, z, θ , C and D are noted. Oscillator level is kept constant at 0.05 Volts. The measurements were carried out in the temperature range from 25°C to 280°C. The conductivity depends on the ZrO₂ phases and the concentration of vacancies that contribute to the

conduction process. In ZrO_2 , The dominant charge carriers are the oxygen vacancies. The conductivity also depends on the energy required for moving these defects through the structure. The conductivity in the grain (g) and grain boundaries (gb) can be expressed as²⁹:

$$\sigma_g = \frac{1}{\rho_g} = \frac{q^2}{kT} c_g D_g \exp\left(-\frac{E_g}{kT}\right) \quad \text{----- (1)}$$

and

$$\sigma_{gb} = \frac{1}{\rho_{gb}} = \frac{q^2}{kT} c_{gb} D_{gb} \exp\left(-\frac{E_{gb}}{kT}\right) \quad \text{----- (2)}$$

where, ρ_g and ρ_{gb} are the resistivities of grain and grain boundaries respectively.

q is the electric charge carried by an oxygen vacancy.

k = Boltzmann constant and T = temperature in Kelvin.

D_g and D_{gb} are the pre-exponential constants for diffusion coefficients in the grain and grain boundary respectively.

c_g and c_{gb} are the concentrations of oxygen vacancies in the grain and grain boundary respectively.

E_g and E_{gb} are the activation energies for diffusion in the grain and grain boundary respectively.

The effective conductivity of the grain is defined as:

$$\sigma_g = \frac{1}{R_g} \left(\frac{l}{A} \right) \quad \text{----- (3)}$$

And the effective conductivity of the grain boundary is defined as:

$$\sigma_{gb} = \frac{1}{R_{gb}} \left(\frac{l}{A} \right) \quad \text{----- (4)}$$

where, R_g and R_{gb} are the resistance of the grain and grain boundaries respectively and

l and A are the thickness of the thin film and area of the electrode respectively.

The resistance was calculated from the diameter of the semicircle in the Cole-Cole plots (from the respective semicircles described in chapter 3). Knowing R_g , R_{gb} , l and A , the dc conductivity of grain and grain boundary can be calculated.

The conductivity data for grain and grain boundary conductivity can be plotted as $\ln(\sigma_g)$ vs $1000/T$ and $\ln(\sigma_{gb})$ vs $1000/T$. The effect of T in the denominator of the pre-exponential factor is negligible and is usually neglected. The activation energies for grain and grain boundaries can be obtained by knowing the slope of the plots respectively. In our samples we have obtained a single semicircle in almost all cases and thus only one activation energy data was obtained

2.4.9 Dielectric constant and dielectric loss

High dielectric constant materials are finding increased use in electronic industry. High dielectric constant material can speed up the microprocessor appreciably if used in MOSFETs. The dielectric properties such as dielectric constant, dielectric loss factor, dielectric resistivity, dielectric strength and magnetic permeability are very useful for ceramic applications. The capacitance (C) and dielectric loss factor (D) are measured directly by impedance analyzer for all the samples. The thin film sandwiched between the top and bottom electrodes acts as MOM (metal oxide metal) capacitor.

The capacitance of a dielectric materials is given by

$$C = \epsilon_o \epsilon_r \frac{A}{l} \quad \text{----- (5)}$$

where, ϵ_o = permittivity of vacuum,

ϵ_r = dielectric constant of the film,

A = area of the top electrode,

and, l = thickness of the film.

From equation (5),

$$\varepsilon_r = \frac{1}{\varepsilon_o} \left(\frac{C \times l}{A} \right) \quad \text{----- (6)}$$

Hence, ε_r was calculated in the frequency range of 1 kHz to 7 MHz for all the samples at temperature between 25°C to 280°C. The dielectric loss was directly read from the impedance analyzer and was plotted as a function of frequency and temperature.

Results and discussion

3.1 Thickness and microstructure of the films

The thickness measurement was carried out using a surface profilometer (Tencor Alpha step 100). Examples of profilometer traces are given in figure 3.1.1. The thickness of ZrO_2 and Gd_2O_3 -doped ZrO_2 films are given in table 3.1. All samples are prepared using 0.2 M sol. The number of coatings is 10.

Figures. 3.3 (a to d) show the optical micrographs of some of the films. The films dried at $\sim 125^\circ\text{C}$ and subsequently treated at 500°C are smooth and crack free except some cracks present near the corners or edges of the films (Fig. 3.3 a to c). The film dried at 200°C and fired at 500°C has cracks [Fig. 3.3 (d)].

Figures. 3.1.2 (a to c) show the AFM topographic images of some of the films. The root mean square (RMS) surface roughness was calculated from AFM images by using picoscan software. For pure ZrO_2 film and 5 mole % Gd_2O_3 - ZrO_2 film, the surface was found to be smoother than other samples. The RMS surface roughness value for pure, 5 and 9 mole % Gd_2O_3 - ZrO_2 film was found to be 0.669, 0.806 and 6.423 nm for a scan area of 300 nm x 300 nm, while the same for the polished substrate was found to be 1.179 nm for a scan area of

1000 nm x 1000 nm. RMS surface roughness values between 12.2 – 16.1 nm were reported for zirconia thin films on stainless steel by Paterson et. al.²⁵ for a scan area of 2000 nm x 2000 nm. Kim et al.⁴³ reported the RMS surface roughness of 13.699 nm for the same scan area for CVD YSZ thin films.

The AFM phase images show that pure and 5 mole % Gd_2O_3 films have grain size of the order of 10-25 nm [Fig. 3.4 (a) and (b)], while 9 mole % Gd_2O_3 film has somewhat coarser grains [Fig. 3.4 (c)]. Fine grain size ~50 – 54 nm was also reported for sol-gel zirconia films by Paterson et. al.²⁵

3.2 Phase analysis by x-ray diffraction

X-ray diffraction technique is used to determine the phases present in the pure ZrO_2 films and the films of ZrO_2 containing 1.75, 2.5, 4, 5, 8, 9 and 11 mole % Gd_2O_3 heated at 500°C for 10 minutes. The X-ray diffractograms (intensity Vs 2θ) of the films are taken between $2\theta = [20^\circ, 80^\circ]$. The values of 2θ corresponding to the peaks obtained from diffraction patterns are noted and compared with the standard data. The x-ray pattern of the substrate and some of the representative patterns of the films are shown in figure 3.2. In each case, peaks corresponding to the substrate are also observed. These peaks are due to Fe-Cr and CrO.19FeO.7NiO phases present in stainless steel. In addition to the peaks corresponding to the as obtained substrate, two additional peaks are observed at $2\theta = 44.65^\circ$ and $2\theta = 64.86^\circ$ for heat-treated substrate. Both the peaks can be attributed to Fe-Cr phase present in stainless steel. These were ignored while analyzing the diffraction patterns. The XRD of the as-deposited film dried at 125°C for 2 minutes after the final coating is shown in figure 3.2 (c). It shows that the dried films are not crystalline. The films heated at 500°C for 10 minutes show additional peaks. The peaks are quite broad. The high intensity peak data for the various phases of ZrO_2 taken from JCPDS is given in table 3.2. According to the data for bulk samples, the $\text{ZrO}_2\text{-Gd}_2\text{O}_3$ ceramics have monoclinic structures at 0

and 1.75 mole % Gd_2O_3 , tetragonal between 2.5 and 4 mole % Gd_2O_3 and cubic between 9 and 11 mole % Gd_2O_3 .

The x-ray diffraction data from the film is difficult to analyze because (i) only a few peaks are observed (ii) the peaks are broad, which can be due to their small grain size or due to incomplete crystallization.

However, certain features present in the diffractogram help to indicate the phases present. Thus in the 1.75 mole % Gd_2O_3 sample, there is a small peak at $2\theta = 34.5^\circ$ which shows that this film has the monoclinic structure. Similarly a peak at $2\theta = 30^\circ$ in the 2.5 and 4 mole % Gd_2O_3 samples show that these compositions contain the tetragonal phase. In the higher composition samples the small number of peaks that are present are those which occur nearly at the same position for both the tetragonal and the cubic structures. Based on all these observations, it can be assumed that the films crystallize into structures as observed for the bulk ceramics i.e. in the monoclinic for 0 and 1.75 mole % Gd_2O_3 , t phase for 4 mole % Gd_2O_3 , mixed t + c for 5 and 8 mole % Gd_2O_3 , and c phase for 9 and 11 mole % Gd_2O_3 samples. This conclusion is supported by the results on electrical conductivity discussed later.

3.3 Electrical properties

In impedance analysis different $|z|$ and θ values were obtained at different frequencies, where $|z|$ is the impedance and $\theta = \tan^{-1}(z''/z')$. The plot of $|z|\sin\theta$ (z'') Vs $|z|\cos\theta$ (z') yields a semicircle which is popularly called Cole-Cole plot. Generally, two semicircles and one straight line is obtained for bulk samples^{15, 16, 17} corresponding to the grain, grain boundary and electrode behaviors respectively. These semicircles which are related to grain, grain boundary and electrode interface are obtained at high, intermediate and low frequency range¹³. The computer fitting to semicircles is performed using a non-linear curve fitting employing the Origin

6 software for all the impedance plots. The detailed procedure is described in Appendix-3. Figures (3.5 to 3.13) show these plots for the samples at different temperatures. One semicircle is obtained for almost all the films. This may be due to the superposition of the grain and grain boundary contributions or may be due to grain boundary conductivity as reported for nanocrystalline thin films¹⁶.

The curve fitting procedure yields the diameter of the semicircle, which is equal to the corresponding resistance.

Using the following formula the dc conductivity can be calculated,

$$\sigma_{dc} = \frac{1}{R_{dc}} \left(\frac{l}{A} \right) \quad \text{----- (1)}$$

where, R_{dc} is the resistance and l and A are the thickness of the film and area of the electrode respectively.

Substituting the value of A (0.5 mm diameter electrode), this relation becomes

$$\sigma_{dc} = \left(\frac{l}{1.9625R} \right) \times 10^{-4} \Omega^{-1} cm^{-1} \quad \text{----- (2)}$$

where R is the diameter of the semicircle in $k\Omega$ and l is the film thickness in μm .

With these conductivity data, $\log \sigma_{dc}$ Vs $1000/T$ is plotted to obtain the activation energy (E_a) for the motion of charges. The electrical conductivity (σ) follows an Arrhenius equation of the form

$$\sigma = B \exp \left(- \frac{E_a}{kT} \right) \quad \text{----- (3)}$$

where, T = temperature in Kelvin,

B = pre-exponential factor (a constant),

k = Boltzmann constant,

and E_a = Activation energy.

The plot of $\log \sigma_{dc}$ Vs $1000/T$ is fit to a regression line using Origin 6 software.

From equation (3) we get,

$$\text{Slope} = (-E_a/k) \times 1000$$

$$\text{So that, } E_a = (-\text{slope}) \times k \times 1000 \quad \text{----- (4)}$$

Since we have plotted the impedance in $k\Omega$ the activation energy becomes,

$$E_a = (-\text{slope}) \times 1000 \times 8.616 \times 10^{-5} \text{ eV}$$

The values of the dc conductivities and the activation energies are given in table 3.4. Some of the representative plots of $\ln(\sigma)$ versus $1000/T$ are shown in figure 3.14.

The dc conductivity of samples with different Gd_2O_3 content is plotted at different temperatures in figure 3.15. It can be seen that the conductivity decreases with decrease in temperature. The conductivity for 4 mole % Gd_2O_3 sample is found to be higher at all temperatures except at 280°C where the 1.75 mole % sample has the highest conductivity. Hartmanova et. al.⁸ reported highest conductivity for 4.21 mole% Y_2O_3 doped ZrO_2 single crystals.

Dutta⁴⁴ and Singh⁴⁰ have reported the conductivity data for bulk and thin film samples of ZrO_2 - Gd_2O_3 . These data are compared with the present thin film data at 280°C in table 3.5. It is seen that the conductivity for the thin film samples is larger than that for the bulk samples by a factor of more than 10 for almost all samples. Singh found that for the higher concentration, the conductivity for the two cases are nearly equal and difference tends to decrease as the Gd_2O_3 concentration increases. In the case of Y_2O_3 containing ZrO_2 films, the conductivities for the thin films and the bulk samples have been reported to be nearly the same by Chun and Mizutani²⁹.

For pure, 2.5, 5 and 8mole% Gd_2O_3 - ZrO_2 film, two semicircles corresponding to grain and grain boundary can be distinguished at low temperatures (25 and 75°C). The semicircle corresponding to the grain is distinct for 8 mole% Gd_2O_3 - ZrO_2 film at high frequencies ($>1\text{MHz}$) but for other samples the grain and grain boundary semicircles seem to overlap. So it is very

difficult to distinguish them. The large volume of grain boundary in nano-crystalline films may result in grain boundary conduction making the dominant contribution to the overall conduction. This has also been reported by Dutta et. al.⁴⁵ in fine grained $\text{Gd}_2\text{O}_3\text{-ZrO}_2$ ceramics. Wang et. al.⁴⁶ found that the small semicircle at the left was due to an oxide layer in thermal barrier coatings. They also reported an increase in the diameter of the small semicircle with oxidation time.

Table 3.4 gives the variation of conductivity with temperature. The conductivity increases with an increase in temperature for all the films. The conductivity varies periodically with composition and that figure 3.15 also shows that the peaks in conductivity are obtained at Gd_2O_3 content of 1.75, 4 and 8-9 mole %. While at the intermediate contents, the conductivity dips to low values. Similar trend has also been reported by Dutta et. al.⁴⁵ in the $\text{Gd}_2\text{O}_3\text{-ZrO}_2$ bulk ceramics. The peak compositions correspond to the single phase regions (1.75 mole % monoclinic; 4 mole % tetragonal and 8-9 mole % cubic) in the bulk samples. The similarity in the behavior of electrical conductivity points to the existence of monoclinic, tetragonal and cubic phases at 1.75, 4 and 8-9 mole % Gd_2O_3 respectively in the thin films also.

Thus the x-ray evidence, together with the variation in the electrical conductivity, support the conclusion that the thin $\text{Gd}_2\text{O}_3\text{-ZrO}_2$ films after heat treatment at 500°C have also crystallized in phases which behave similar to the phases expected in the bulk ceramics.

The activation energy variation with different mole% Gd_2O_3 is presented in the figure 3.16. The activation energy varies from 0.29 to 0.38 eV. The activation energy for grain conduction in bulk $\text{ZrO}_2\text{-Gd}_2\text{O}_3$ samples has been found to vary between 0.75 eV to 1.12 eV with Gd_2O_3 concentration between 1.75 to 11 mole % by Dutta et. al.⁴⁵. Chun and Mizutani²⁹ found the value of activation energy in 3 mole % Y_2O_3 doped thin film to be 1.22 eV. However, we obtained much lower values i.e. 0.29 to 0.38 eV in the thin film samples on stainless steel. The values in the same range was reported by Yeh et. al.³¹. They indicated that thermal annealing reduces the activation energy for electrical conduction due to free oxygen vacancies by as much

as 50%. As our films were annealed at 250°C for 5 minutes after electrode deposition the assumption made by Yeh. et. al. may hold true for our samples also. The activation energy is minimum (0.29-0.3 eV) for Gd₂O₃ contents between 2.5 and 5 mole % and is appreciably higher (0.38 to 0.39) for the lower and higher Gd₂O₃ content. The same trend was observed in YSZ single crystals by Hartmanova et. al.⁸. This variation also appears to be due to the phase changes in the film. The activation energy is lowest in the tetragonal composition region and higher and nearly equal in the m and c phase regions.

3.4 Dielectric constant

The dielectric constant was calculated using the following relationship:

Capacitance of the film is given by

$$C = \epsilon_0 \epsilon_r \frac{A}{d} \quad \text{----- (1)}$$

where, ϵ_0 = permittivity of vacuum,
 ϵ_r = relative dielectric constant,
 d = thickness of the film,
and A = area of the electrode.

From equation (1) above,

$$\epsilon_r = C \times d / \epsilon_0 A \quad \text{----- (2)}$$

Thus ϵ_r was calculated by putting the values in the above formula as-

$$\epsilon_r = 0.5757 \times C \times d$$

where, C is in pF and d is in μm .

The capacitance is measured directly from the impedance analyzer. The ϵ_r is plotted against frequency for all the films at different temperatures and is shown in figure 3.17. The ϵ_r is found to have very high values at lower frequencies, which decreases rapidly at the

higher frequencies for all the films. As the temperature is increased, ϵ_r also increases rapidly. At temperatures higher than 200°C the increase in the dielectric constant is associated with the presence of space charge polarization⁴⁷. At higher frequencies (>1MHz), the space charge polarization is negligible and only the dipolar, ionic and electronic polarization contribute to the total permittivity.

In the bulk samples of $\text{Gd}_2\text{O}_3\text{-ZrO}_2$, much higher values of dielectric constant (10000 at low frequency, 300 at high frequencies) have been found by Dutta⁴⁴. In addition, in the plots of ϵ_r Vs frequency for the bulk samples, a distinct step in the plot is observed when the dominant conduction mechanism changes from grain to grain boundary. In the experiments on thin films, the values of dielectric constant are lower and range from few hundreds at low frequencies to ~ 60 at high frequencies and no step is evident.

3.5 Dielectric loss

The dielectric loss spectra were obtained directly from the impedance analyzer. The variation of the dielectric loss with frequency and temperature for pure ZrO_2 and Gd_2O_3 doped ZrO_2 system is shown on log scale in figure 3.18. The dielectric loss decreases rapidly below 100 kHz. At higher frequencies (>100 kHz), the dielectric loss is almost independent of frequency. There is an increase of dielectric loss with increase of temperature. All the doped samples show similar behavior. Figure 3.19 shows the variation of dielectric loss with Gd_2O_3 content at different temperatures at 100 kHz. There appears to be periodic variations in dielectric loss with Gd_2O_3 content and such variation becomes more pronounced with increase in temperature. It is observed that for 4 and 11mole % $\text{Gd}_2\text{O}_3\text{-ZrO}_2$ samples the loss is low as compared to other samples. This aspect needs to be further looked into.

Discussion:

Sol-gel zirconia thin films can be successfully prepared on stainless steel substrate by spin coating. Singh⁴⁰ studied the sticking behavior of ZrO_2 sol on different substrates and found that the sol spreads uniformly over roughly polished stainless steel substrate. Almost crack free films can be prepared by restricting the drying temperature to $\sim 125^\circ\text{C}$. The intermediate firing temperature of 500°C for 10 min results in nanocrystalline films which give broad zirconia peaks. The phases are difficult to determine due to low crystallization temperature, small crystallite size and overlap of some of the zirconia peaks with that of stainless steel, but on the basis of electrical conductivity data we can assume m phase for 1.75 mole % sample, t phase for 5 mole % sample, c phase for 9 mole % sample and mixed phases in between. Singh was unable to distinguish the phases due to the existence of a single broad ZrO_2 peak at $2\theta = 30^\circ$.

The conductivity of the thin films is higher than that of bulk samples by a factor of more than 10. In $\text{Gd}_2\text{O}_3\text{-ZrO}_2$ bulk ceramics⁴⁵ it has been found that the grain boundary resistance increases with a decrease in grain size and a single semicircle was observed in case of very fine-grained bulk samples. Thus, for nanocrystalline samples the grain boundary dominates the electrical properties. Thin film samples show a single semicircle in the Cole-Cole plots which is due to the presence of large volume of grain boundary and small crystallite size as evidenced from broad diffraction peaks and AFM phase images. The activation energy shows an unusually low value between 0.29-0.38 eV while for the same compositions Dutta⁴⁴ found the activation energy for grain boundary conduction to be between 0.75-1.12 eV. However, the lowest activation energies for bulk samples were obtained for samples with smallest crystallite size. Activation energy values between 0.27-0.40 eV was observed by Singh for $\text{Gd}_2\text{O}_3\text{-ZrO}_2$ thin films. Yeh et. al³¹ reported that annealing reduces the activation energy for electrical conduction

due to free oxygen vacancies by 50% (from 0.6 eV in the as-deposited condition to 0.4 eV after treatment to 500°C). Thus, the high conductivity and low activation energy values in our thin films can be explained on the basis of high grain boundary volume, low crystallite size and thermal annealing at 250°C/5min (to get better adhesion of Au-Pd top electrode). The dielectric response of the films is as expected and the dielectric constant and loss shows a decrease with an increase in frequency and decrease in temperature. This decrease is associated with the decrease in space charge polarization⁴⁷ at temperatures lower than 200°C. A similar trend was also observed by Singh⁴⁰.

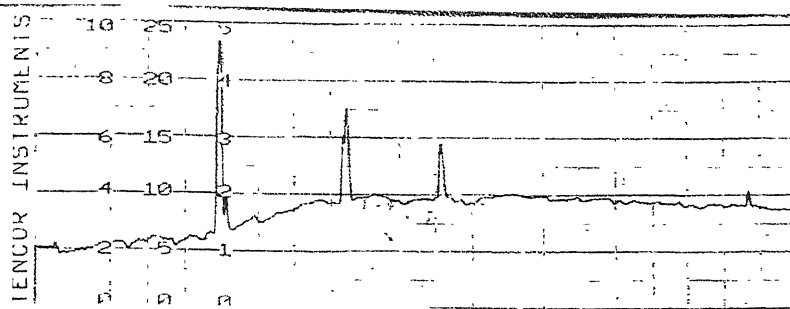


Fig. 3.1.1(a) full scale showing 50 kÅ

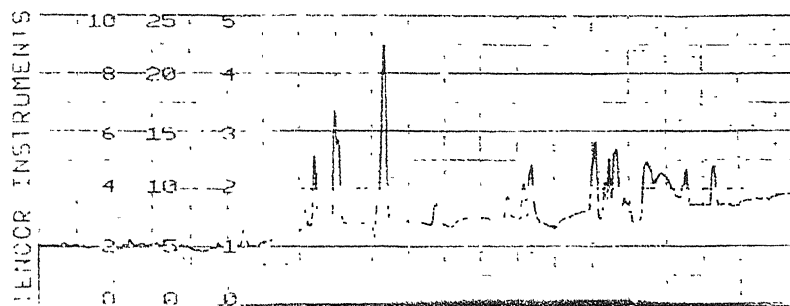


Fig. 3.1.1 (b) full scale showing 50 kÅ

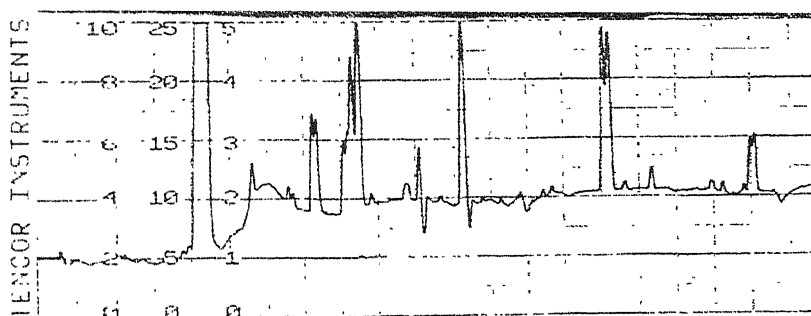


Fig. 3.1.1 (c) full scale showing 25 kÅ

Fig. 3.1.1 Thickness profile of fired $\text{Gd}_2\text{O}_3\text{-ZrO}_2$ thin films of (a) 4 mole%, (b) 5 mole% and (c) 9 mole% Gd_2O_3 content

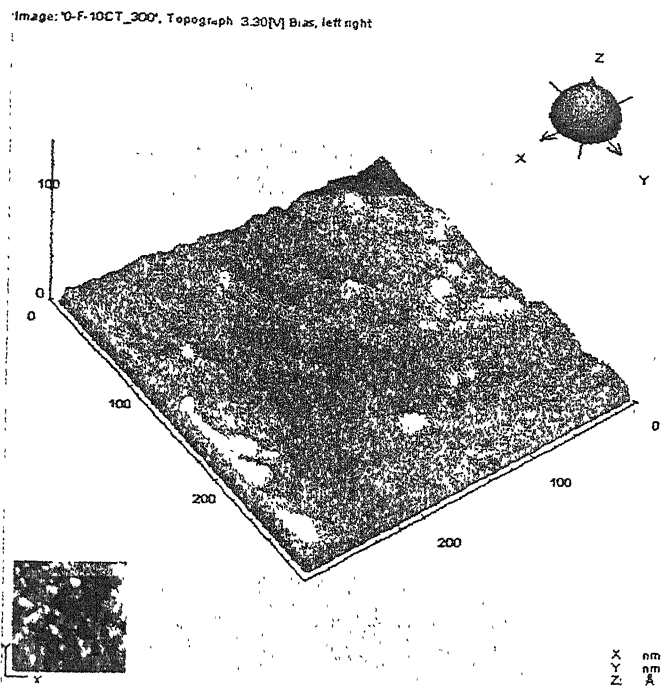


Fig. 3.1.2 (a)

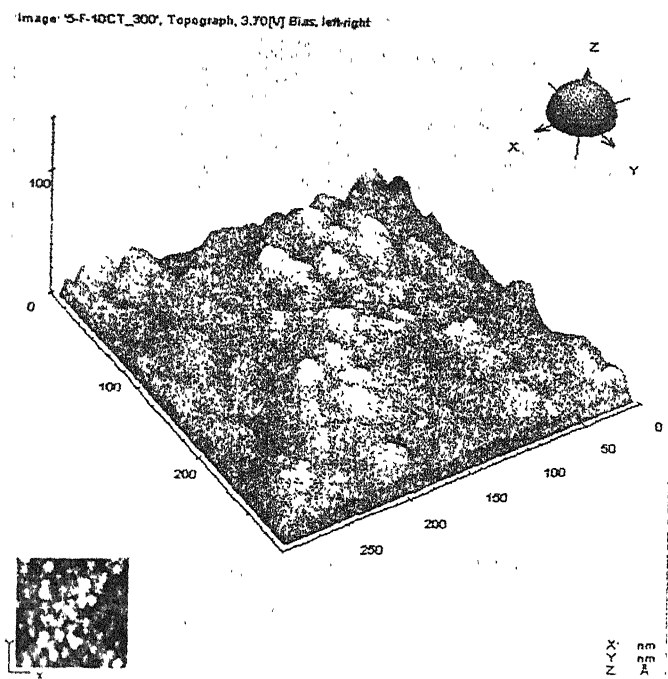


Fig.3.1.2 (b)

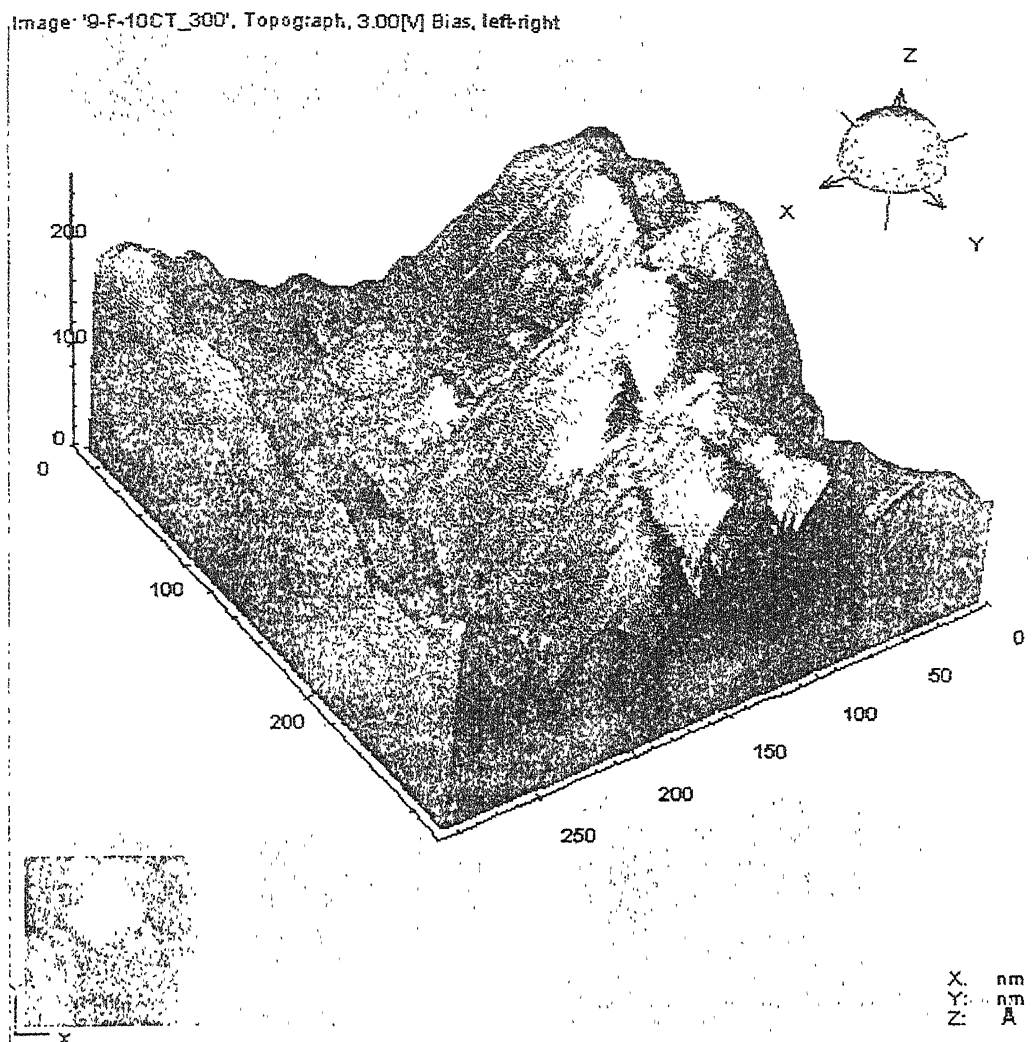
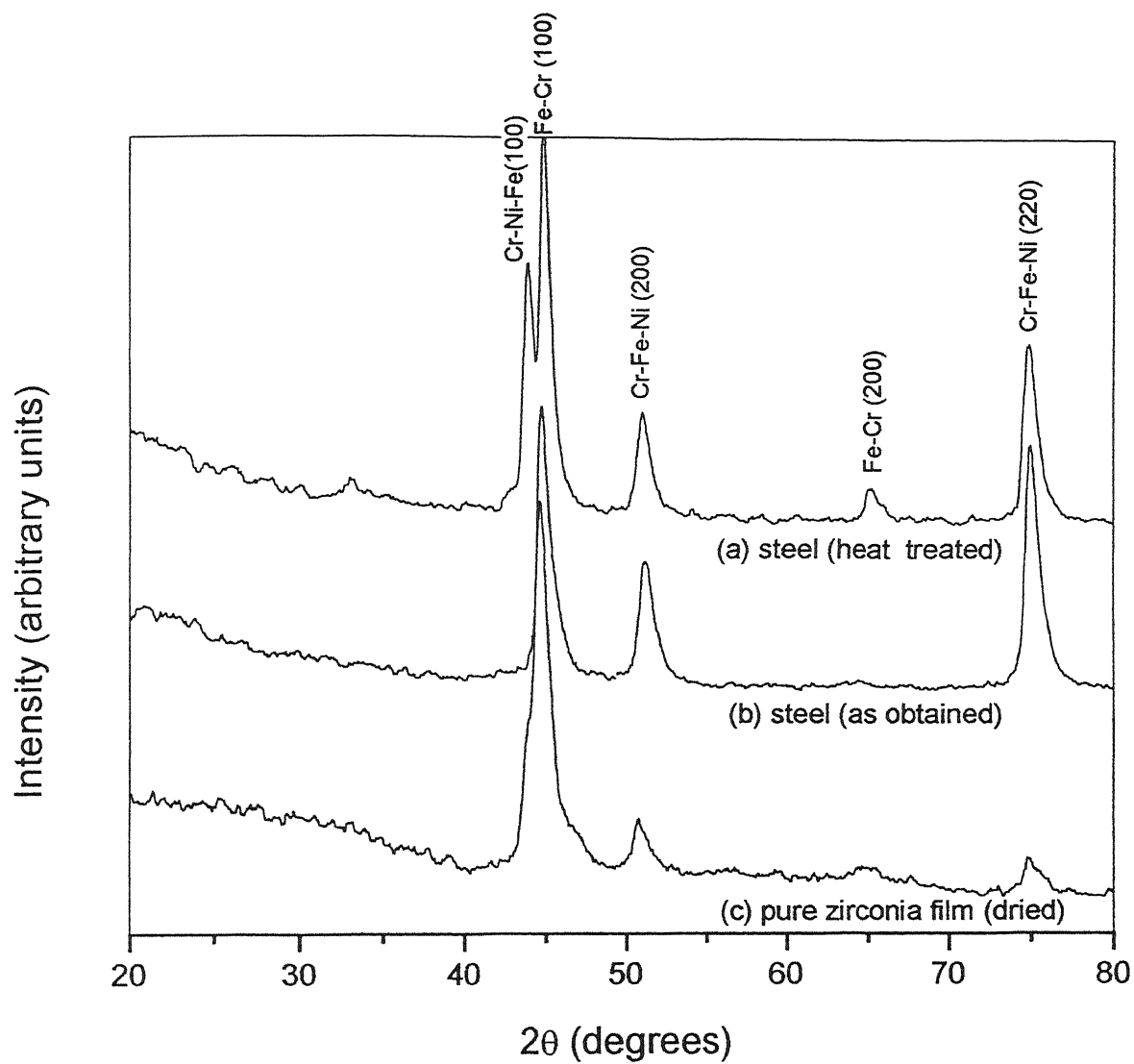
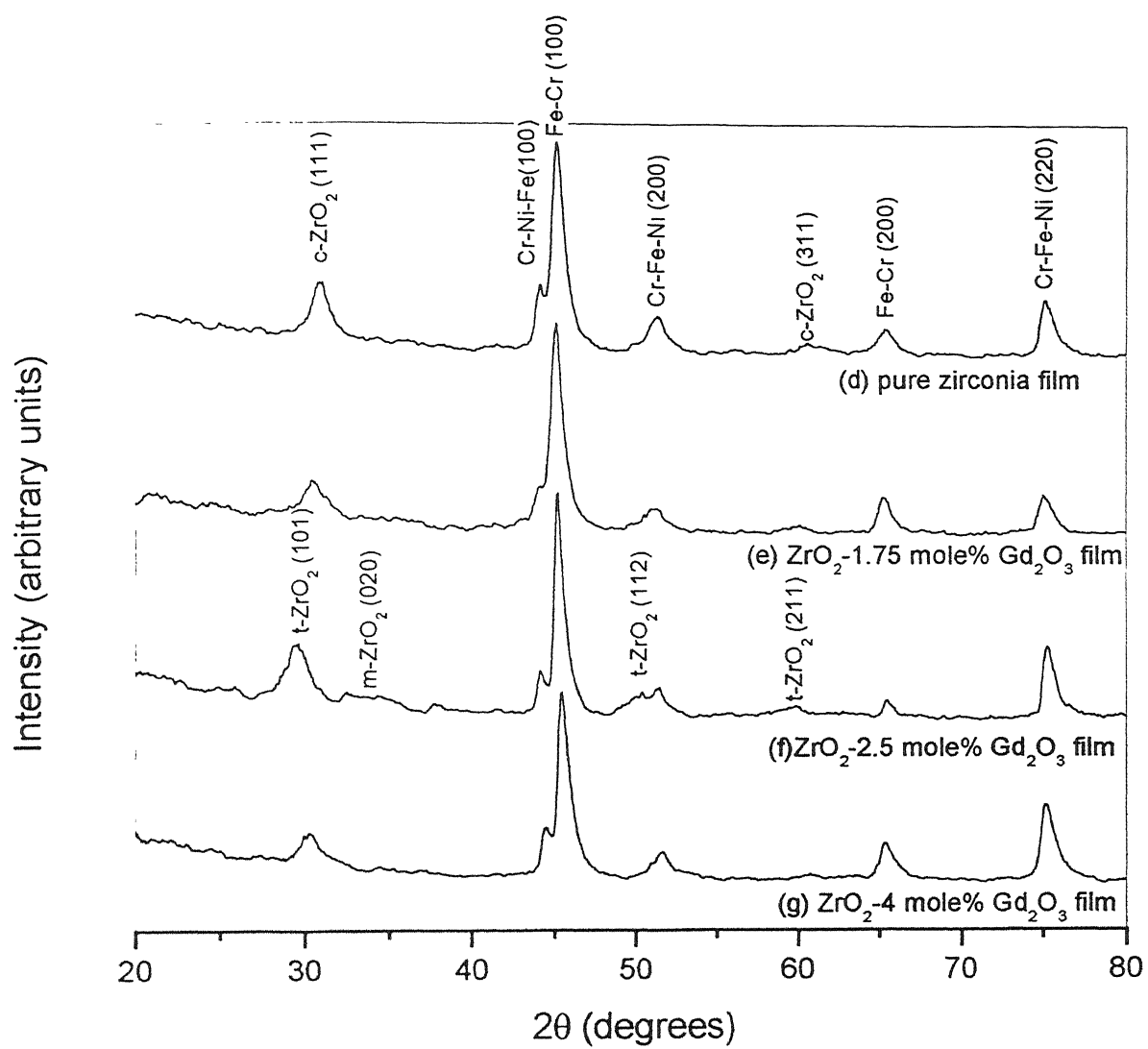


Fig.3.1.2 (c)

Fig. 3.1.2 AFM topographic images of (a) pure zirconia thin film, (b) 5 mole% $\text{Gd}_2\text{O}_3\text{-ZrO}_2$ film and (c) 9 mole% $\text{Gd}_2\text{O}_3\text{-ZrO}_2$ film with a scan area of 300 nm x 300 nm. The Z-axis is in Å.





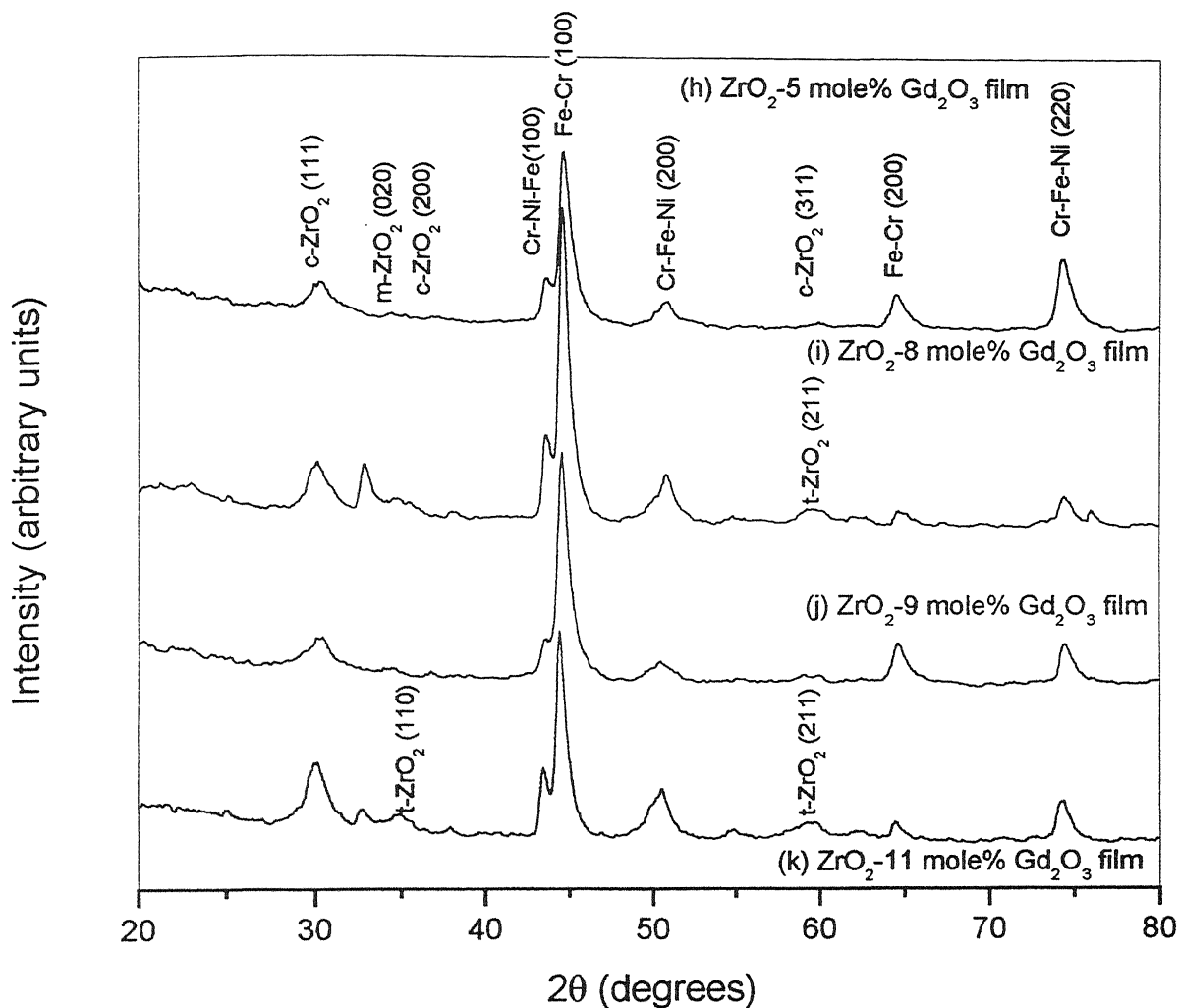


Fig.3. 2 X-ray diffraction plots of (a) Stainless steel substrate heat treated at 500°C for 10 minutes, (b) as obtained steel, (c) pure zirconia film (as deposited); x-ray diffractograms of heat treated films (500°C, 10 min) with different mole % Gd₂O₃ (d) 0 (e) 1.75 (f) 2.5 (g) 4 (h) 5 (i) 8 (j) 9 (k) 11

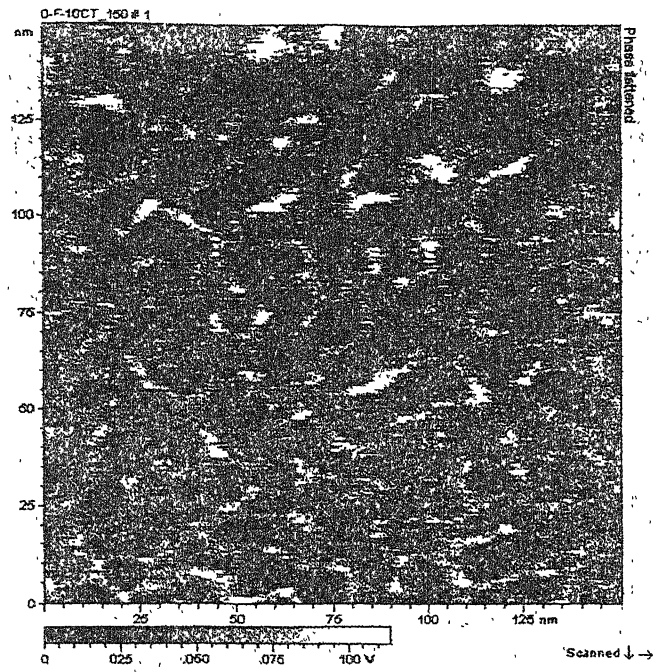


Fig. 3.4 (a)

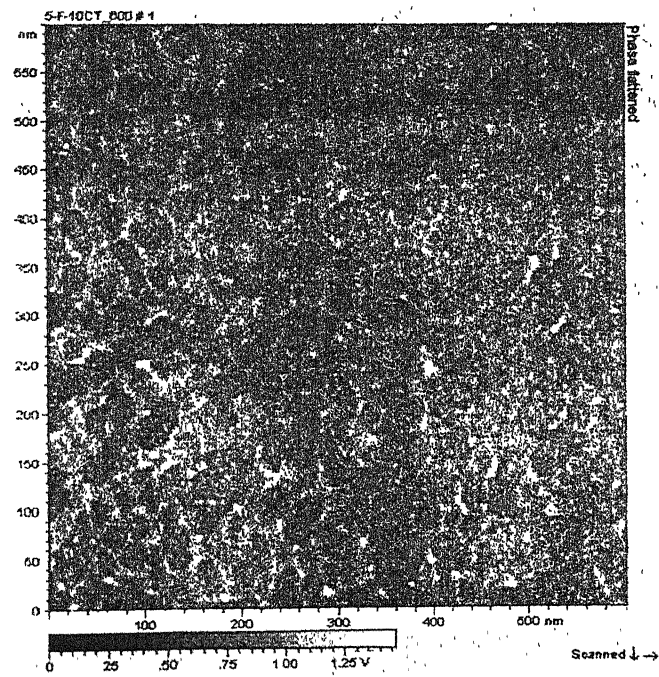


Fig.3.4 (b)

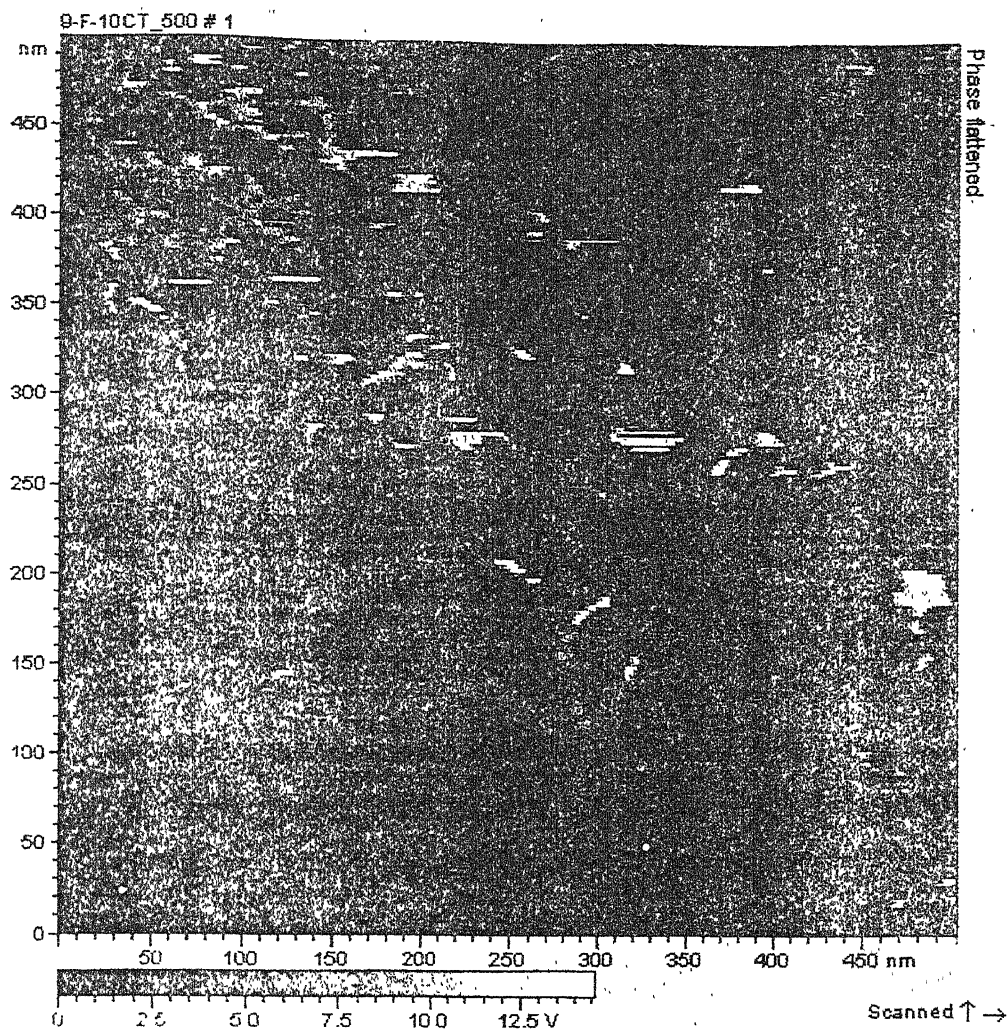
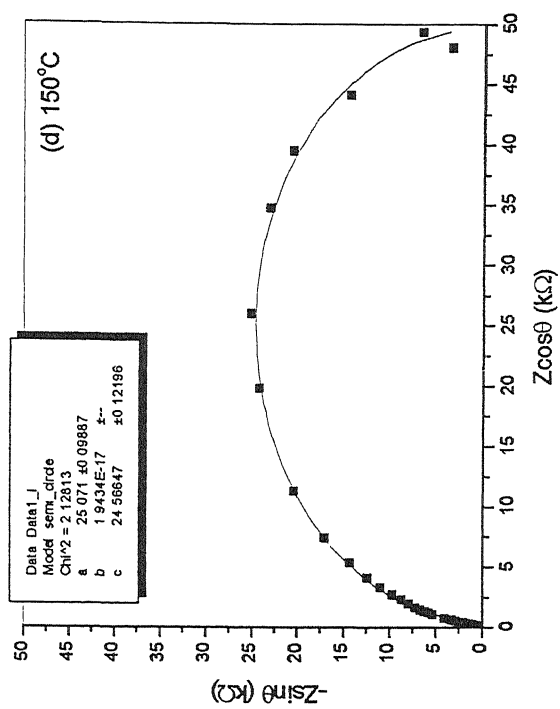
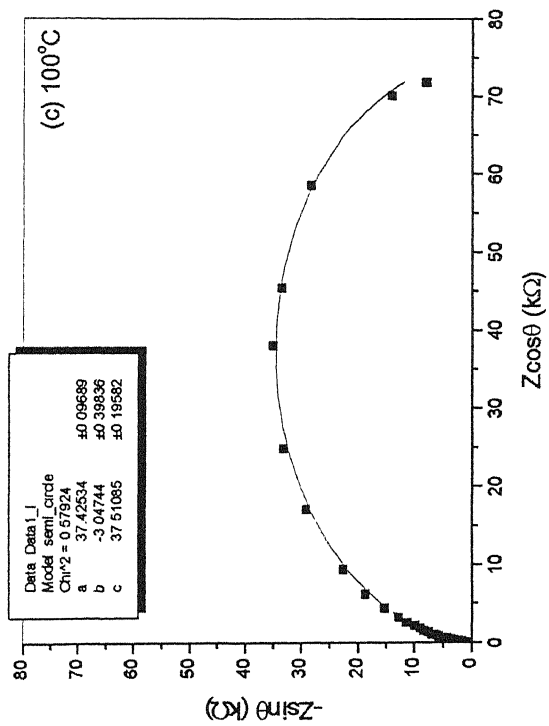
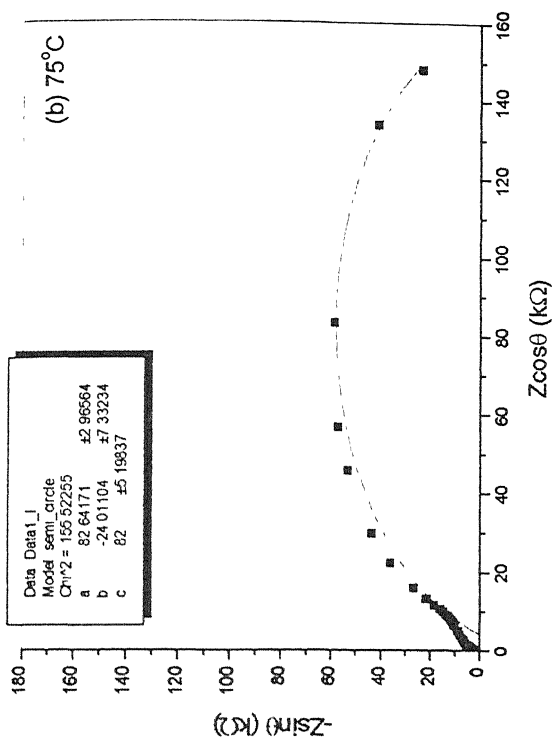
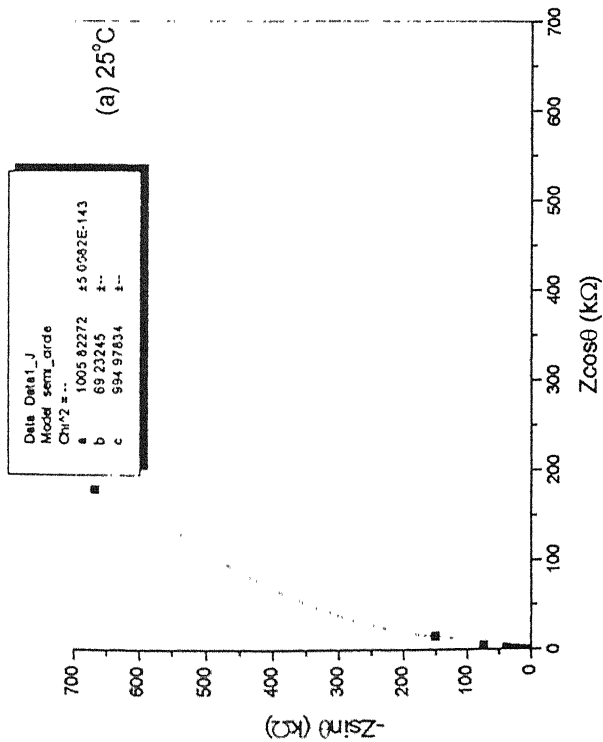


Fig. 3.4 (c)

Fig. 3.4 AFM phase images of (a) pure, (b) 5 mole % $\text{Gd}_2\text{O}_3\text{-ZrO}_2$ and (c) 9 mole % $\text{Gd}_2\text{O}_3\text{-ZrO}_2$ thin films heat-treated at 500°C for 10 minutes.



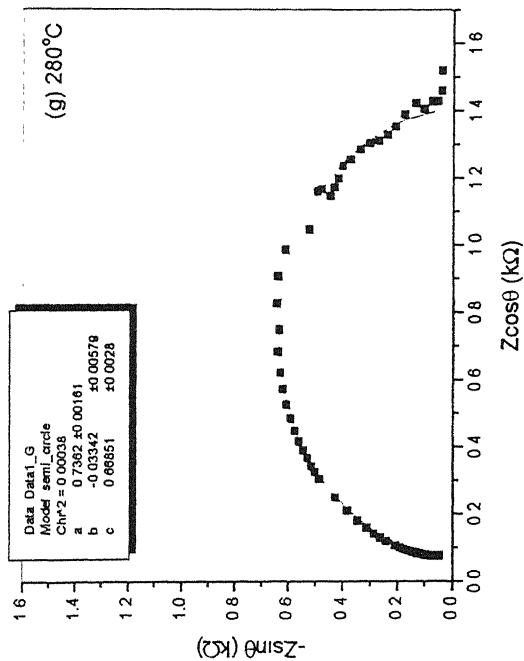
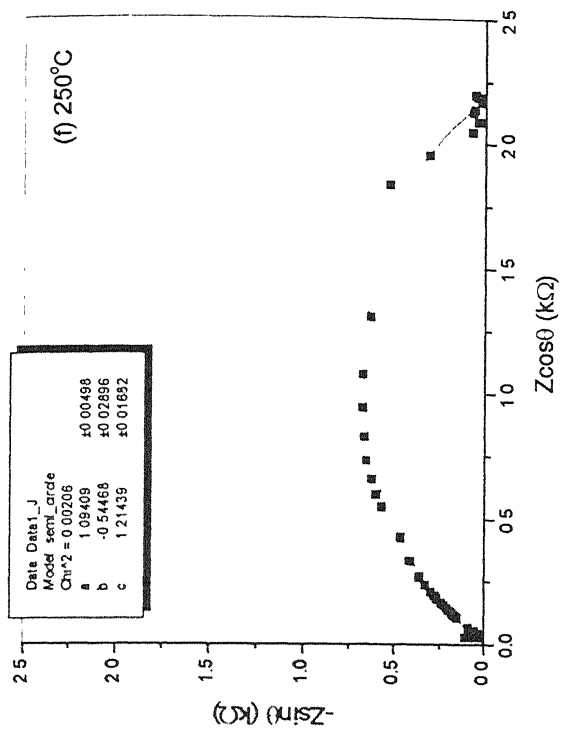
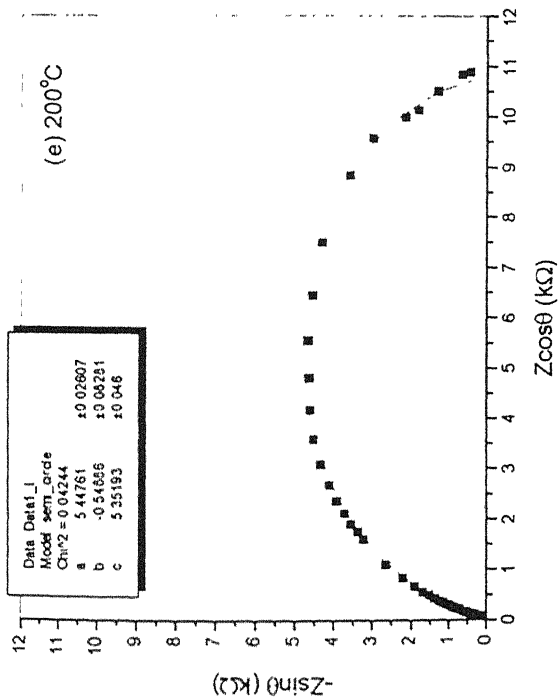
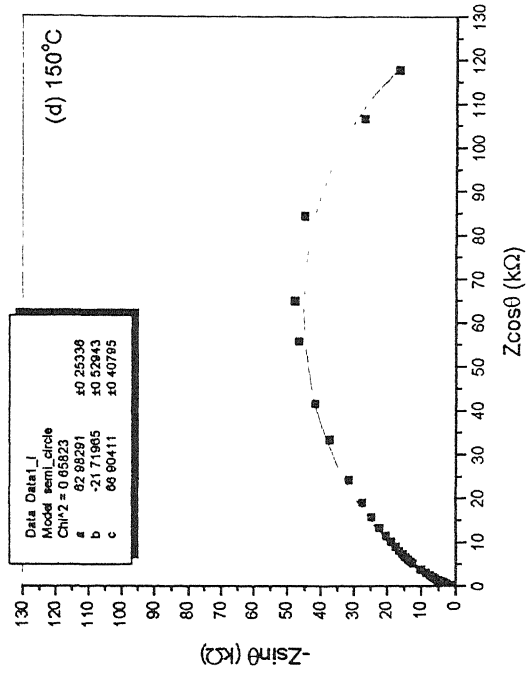
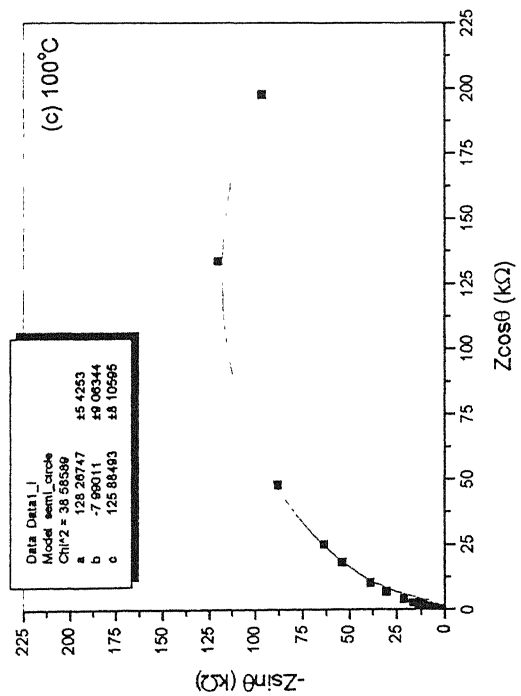
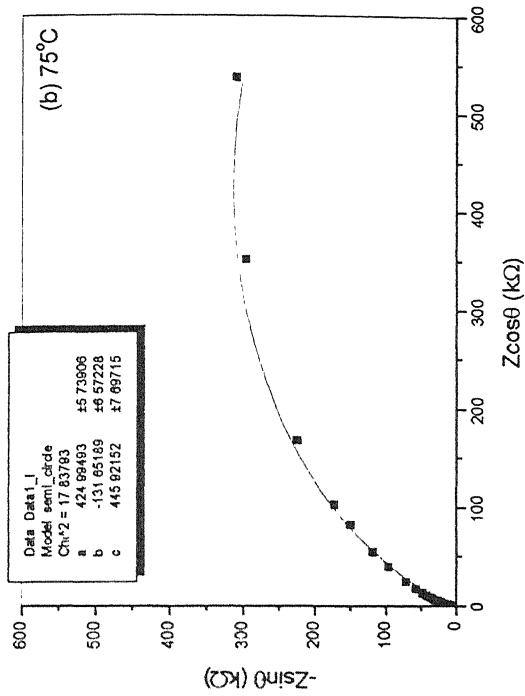
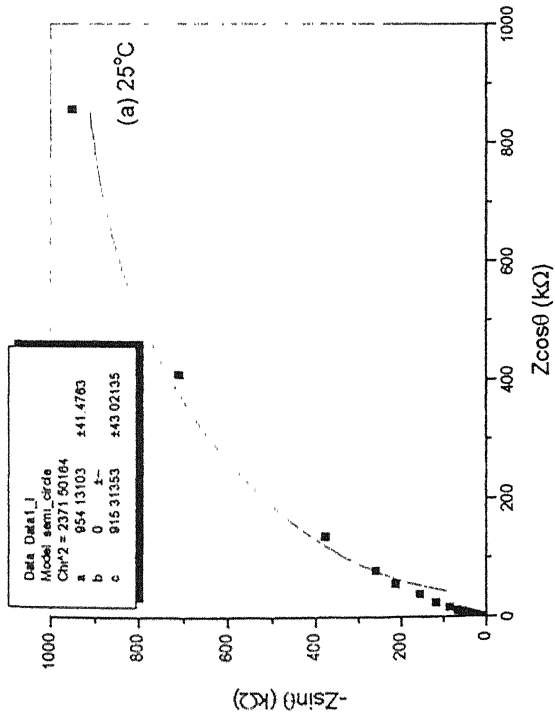


Fig. 3.5 Cole-Cole plots for undoped ZrO_2 thin film at different temperatures



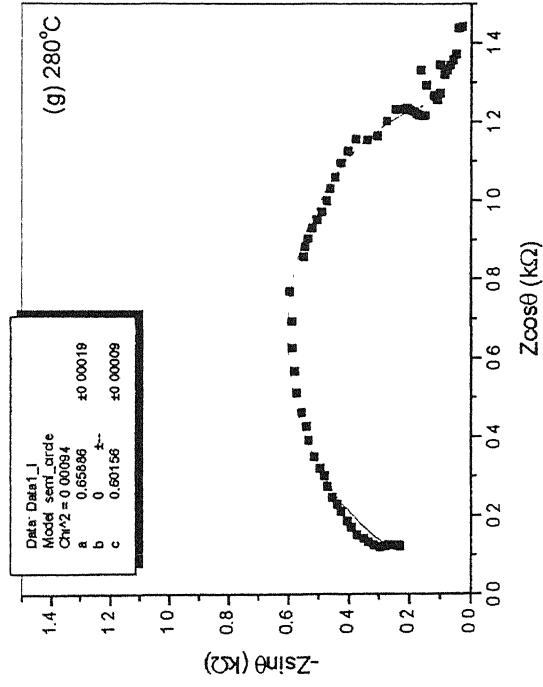
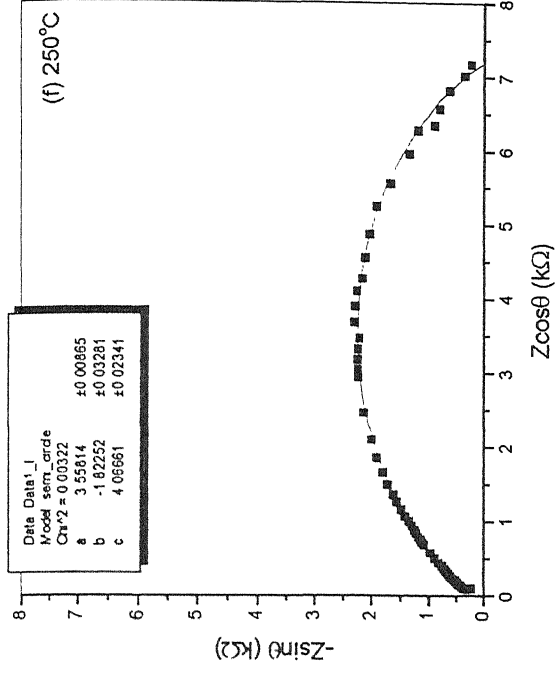
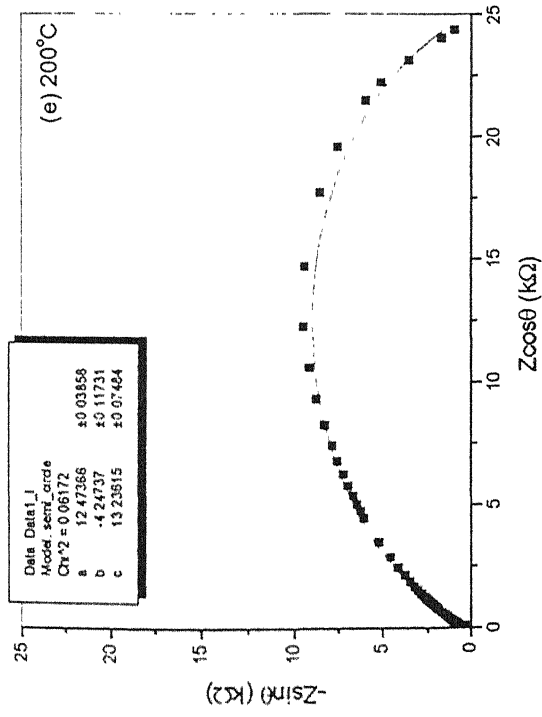
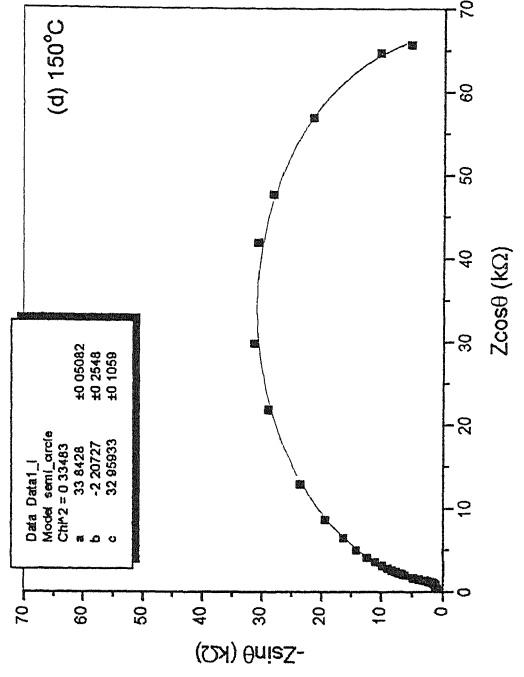
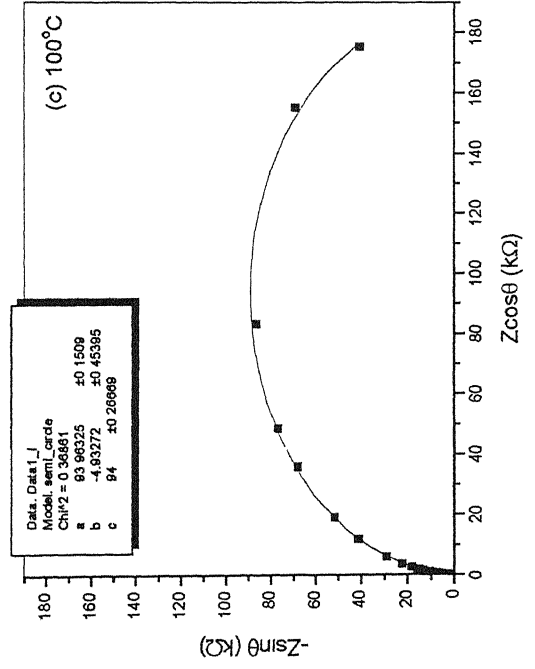
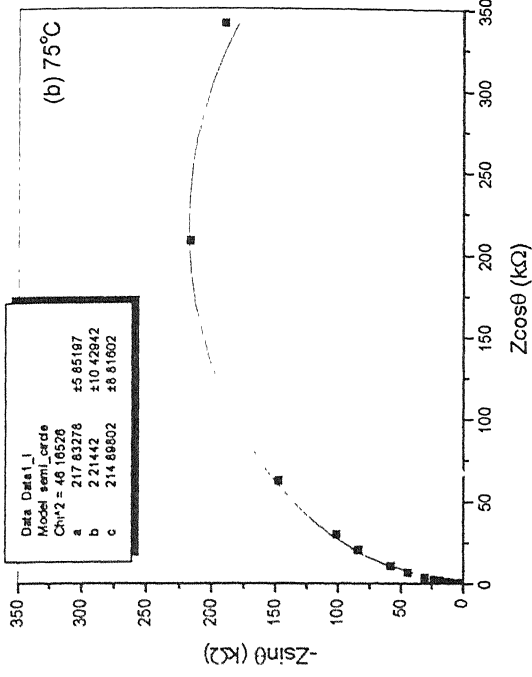
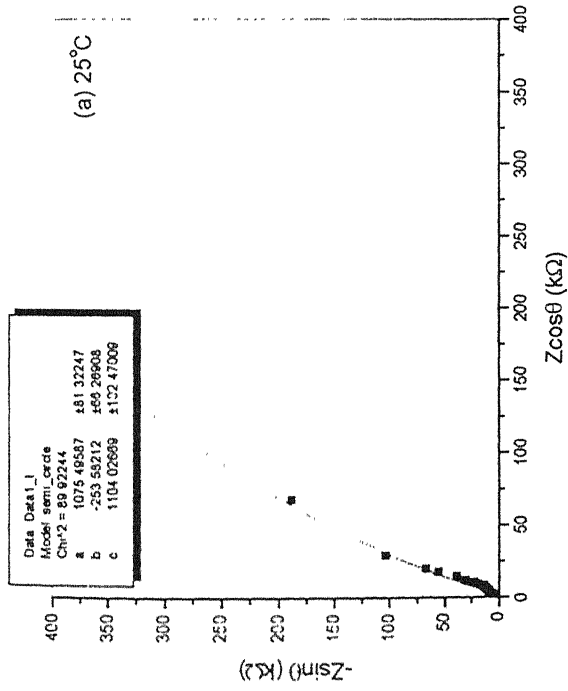


Fig. 3.6 Cole-Cole plots for 1.75mole% Gd₂O₃-ZrO₂ thin film at different temperatures



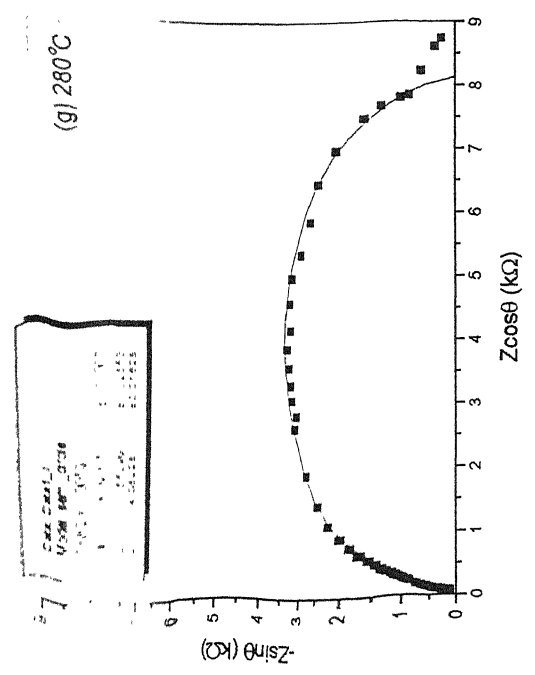
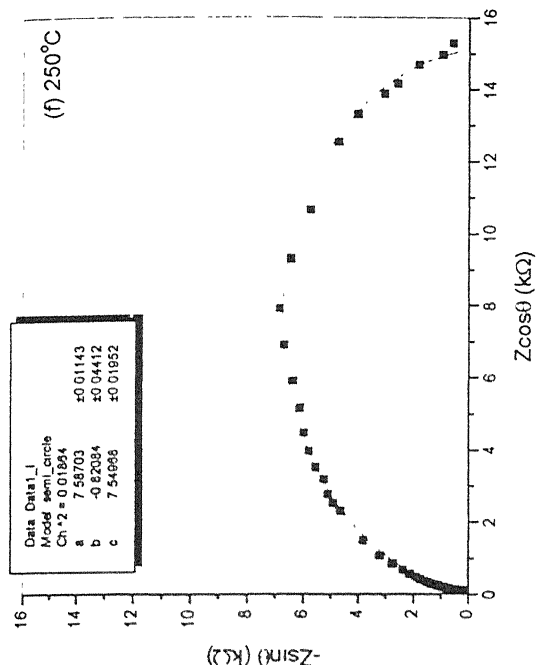
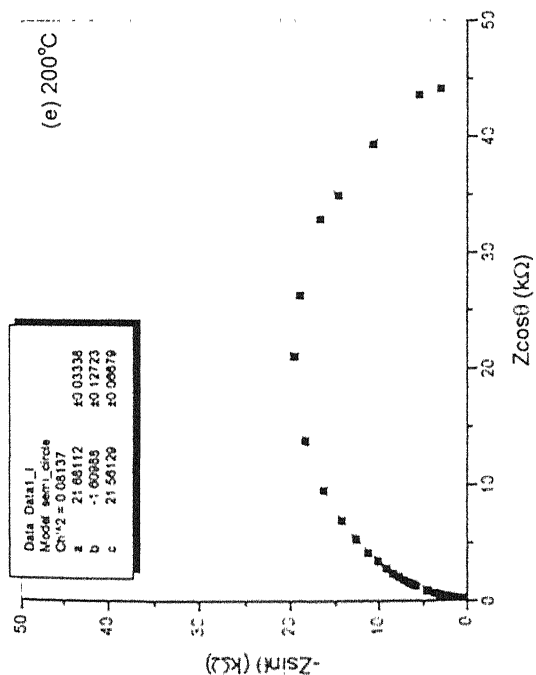
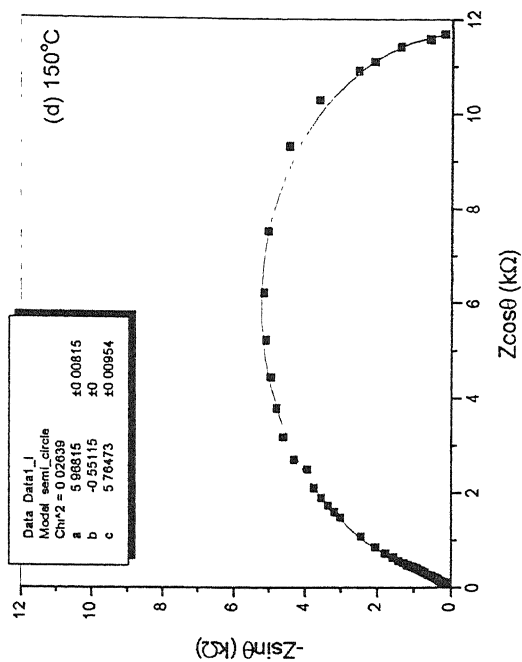
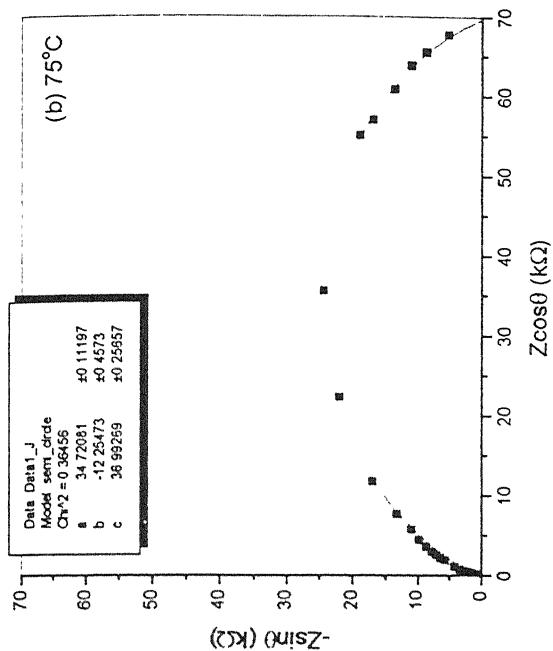
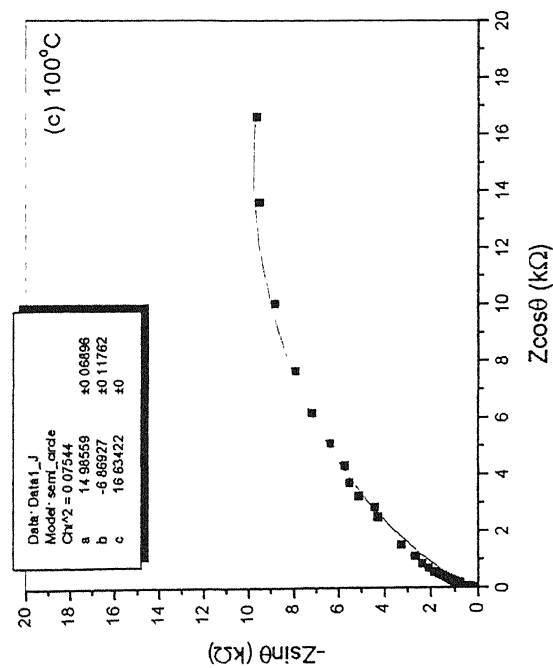
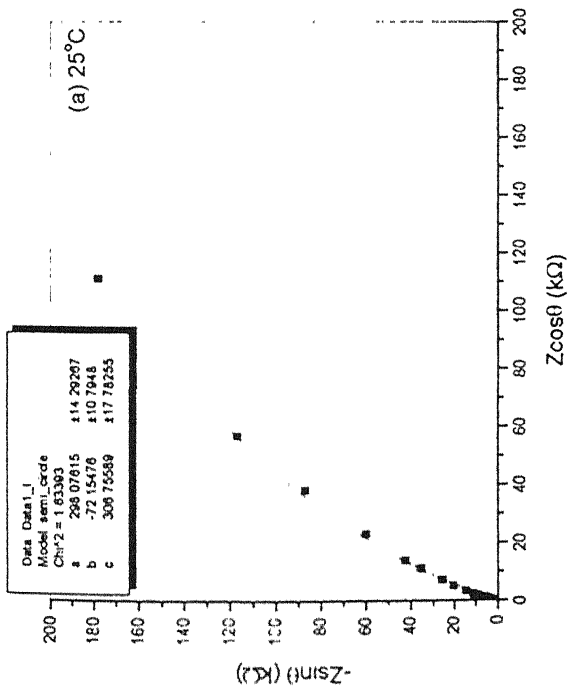


Fig. 3.7 Cole-Cole plots for 2.5mole% $\text{Gd}_2\text{O}_3\text{-ZrO}_2$ thin film at different temperatures



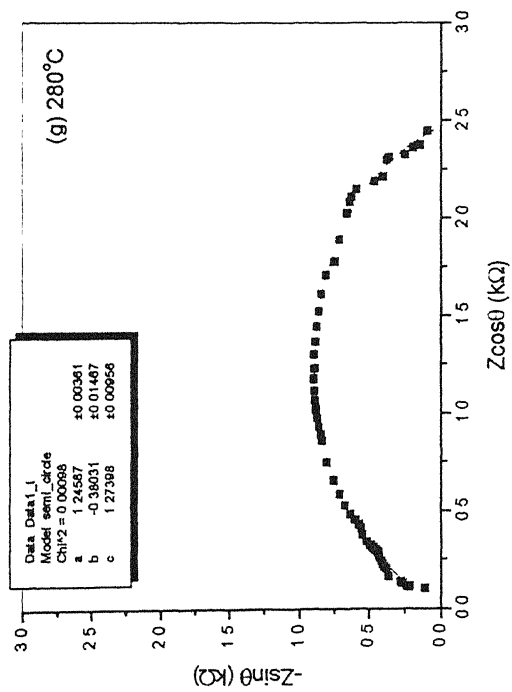
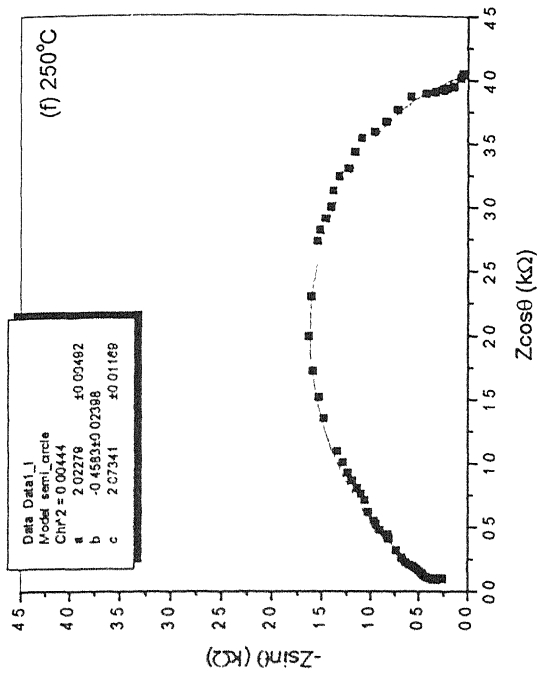
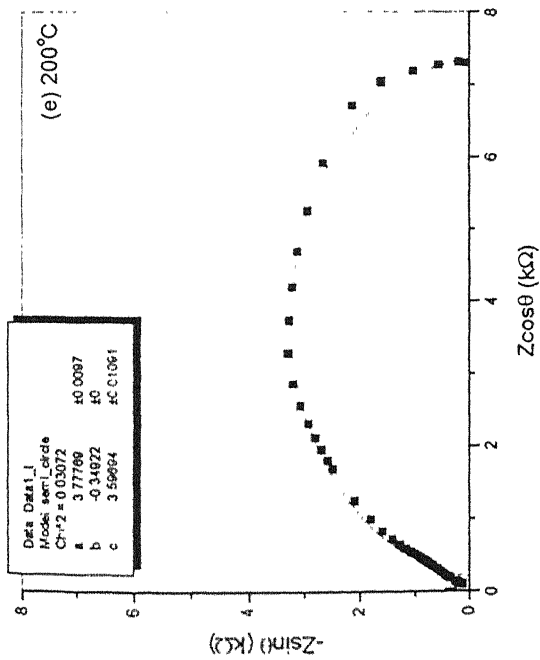
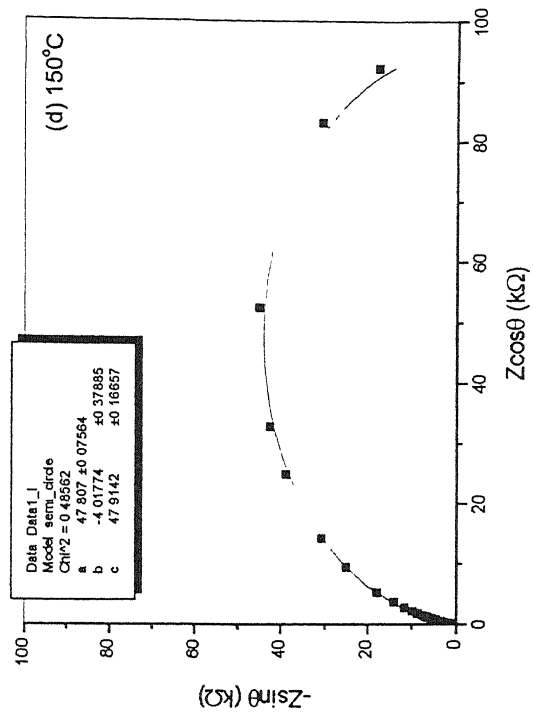
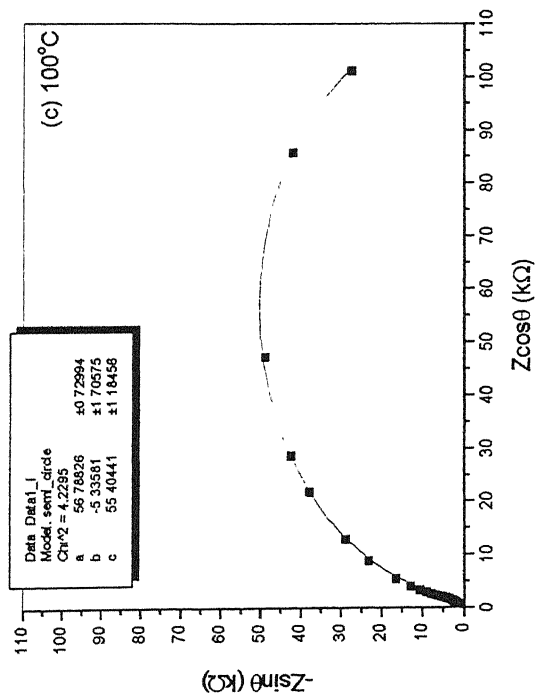
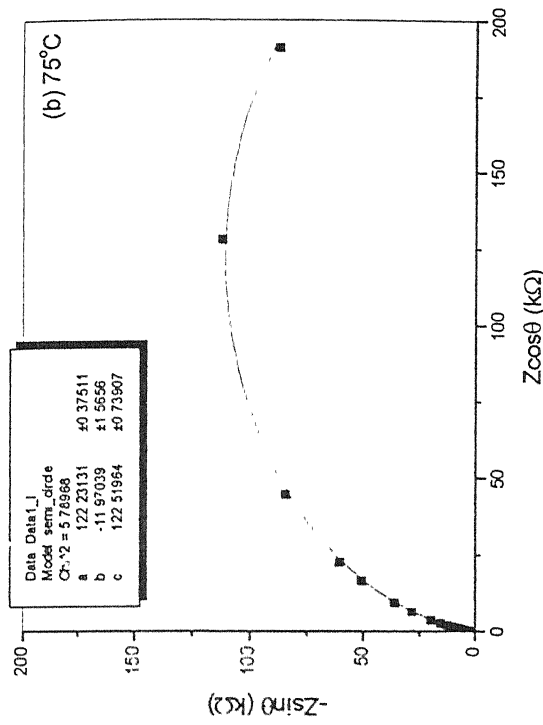
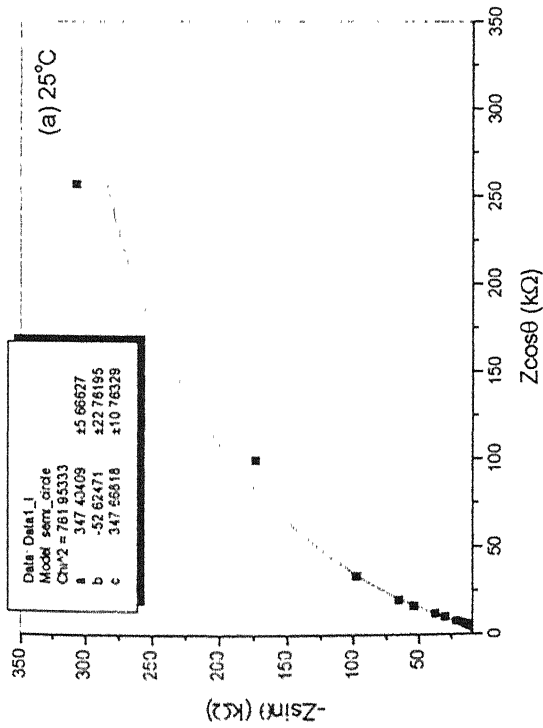


Fig. 3.8 Cole-Cole plots for 4 mole% $\text{Gd}_2\text{O}_3\text{-ZrO}_2$ thin film at different temperatures



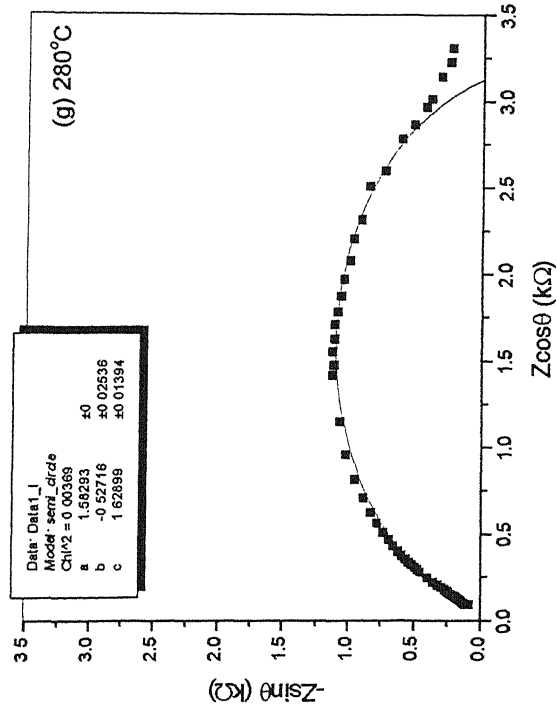
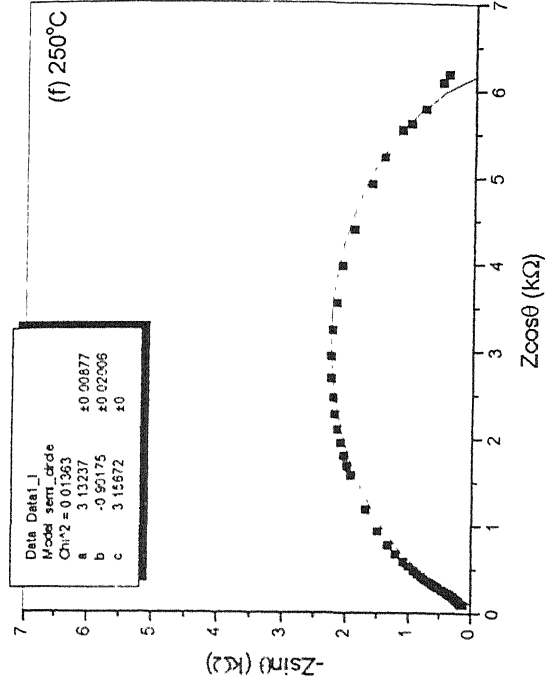
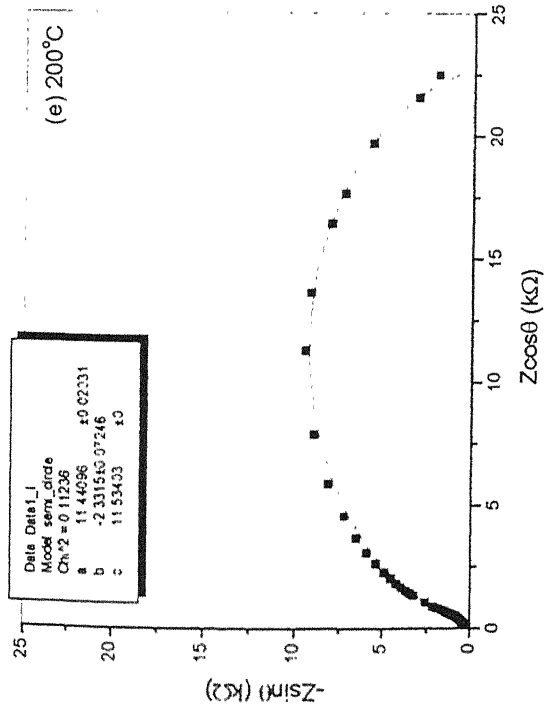
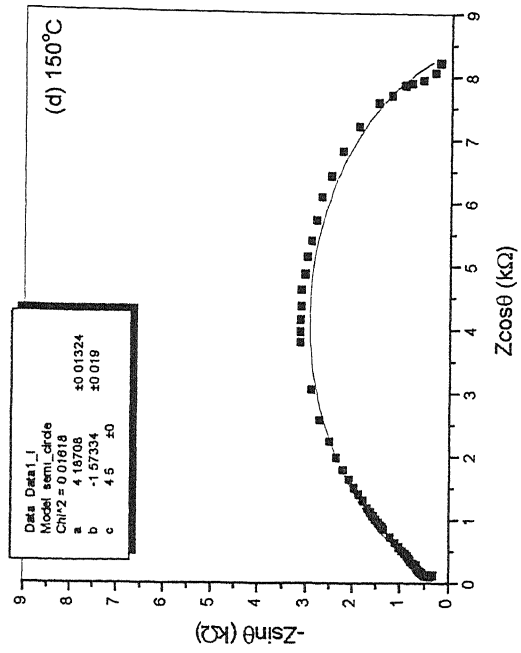
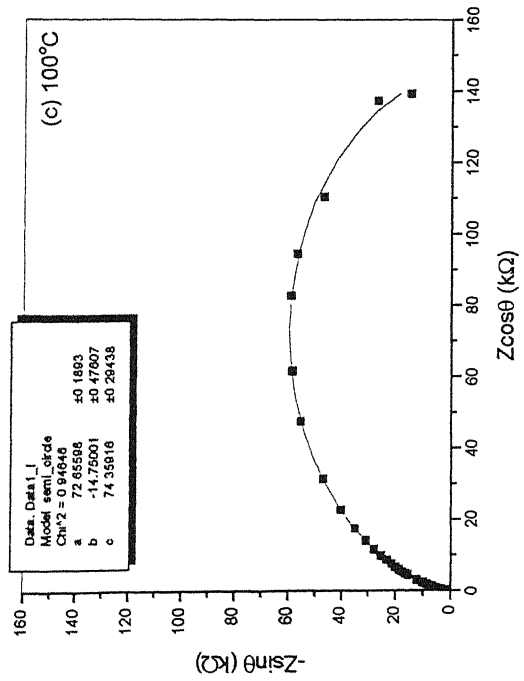
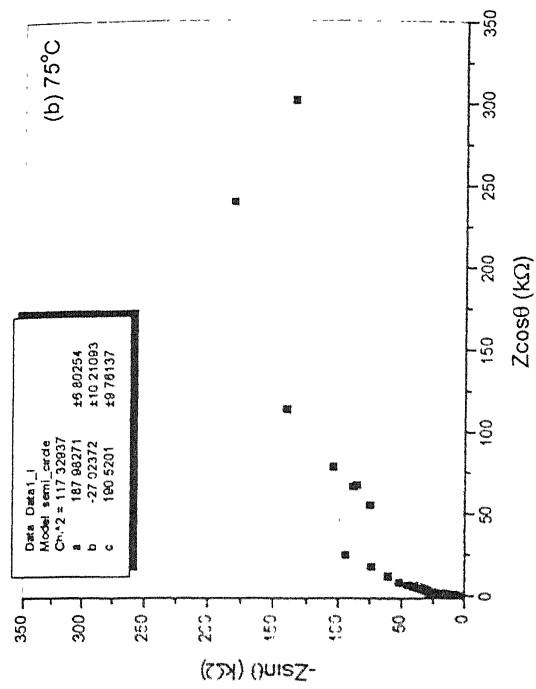
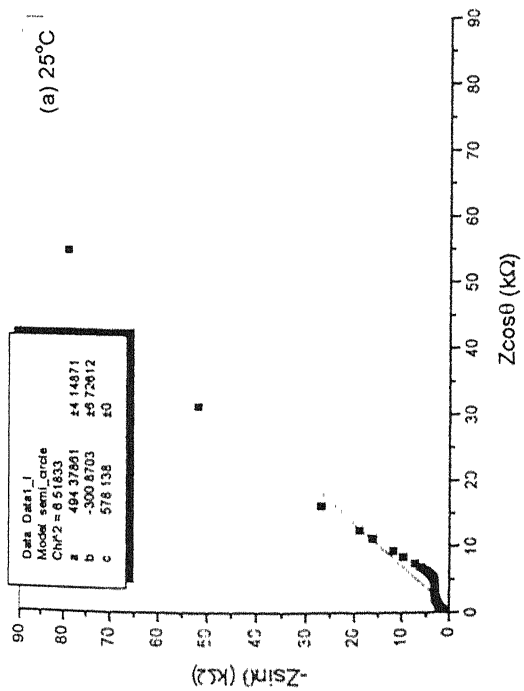


Fig. 3.9 Cole-Cole plots for 5 mole% $\text{Gd}_2\text{O}_3\text{-ZrO}_2$ thin film at different temperatures



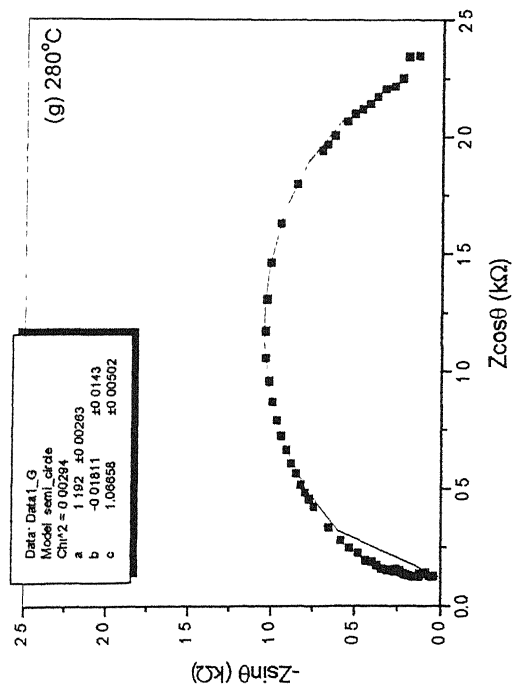
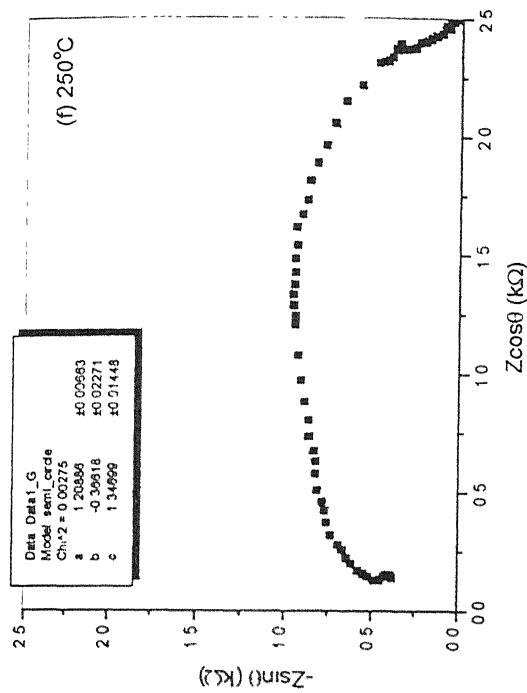
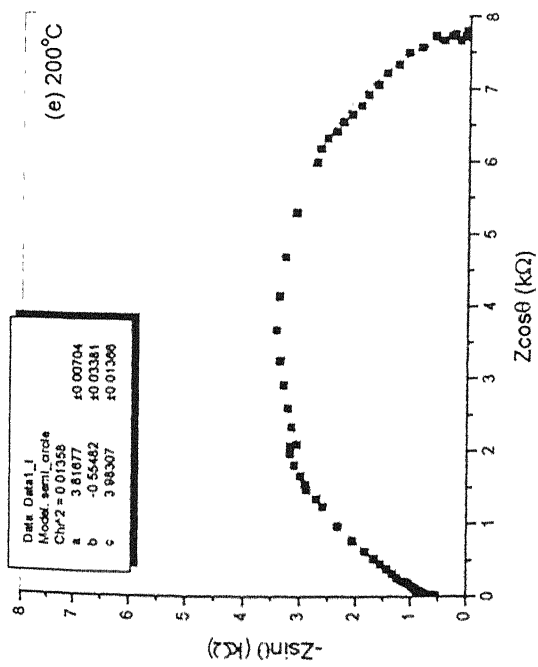
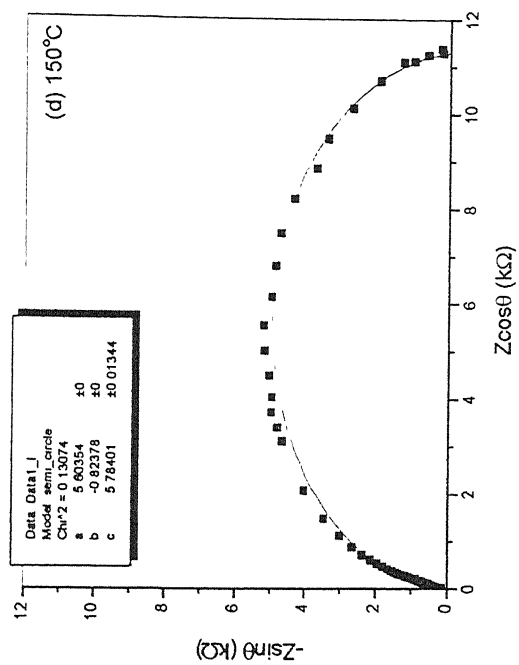
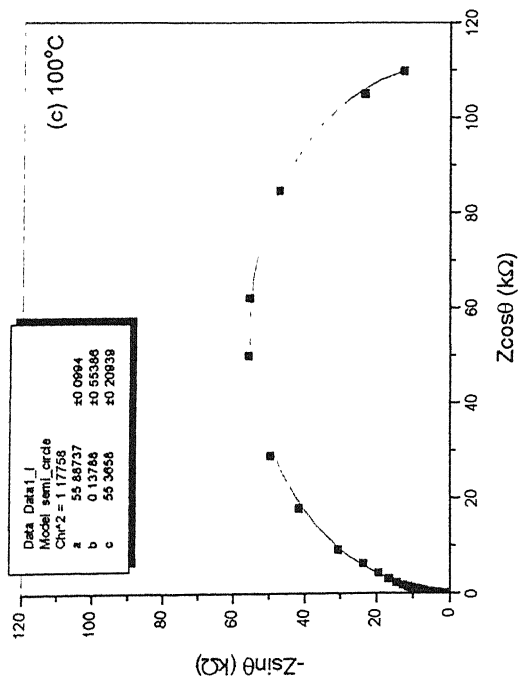
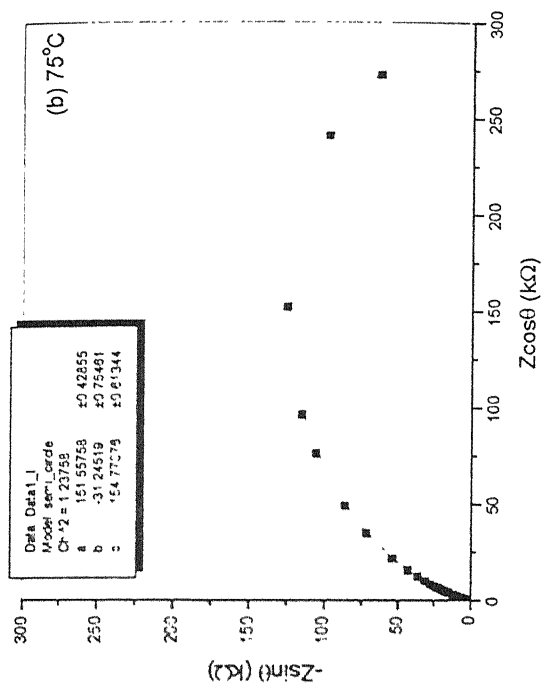
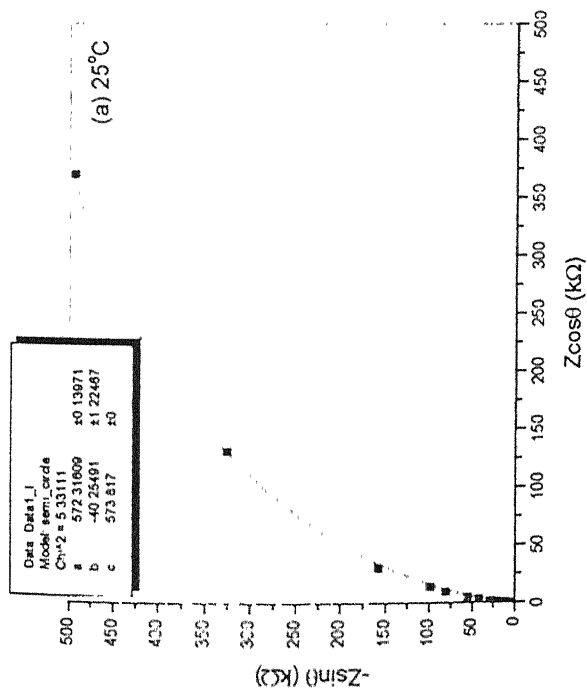


Fig. 3.10 Cole-Cole plots for 8 mole% $\text{Gd}_2\text{O}_3\text{-ZrO}_2$ thin film at different temperatures



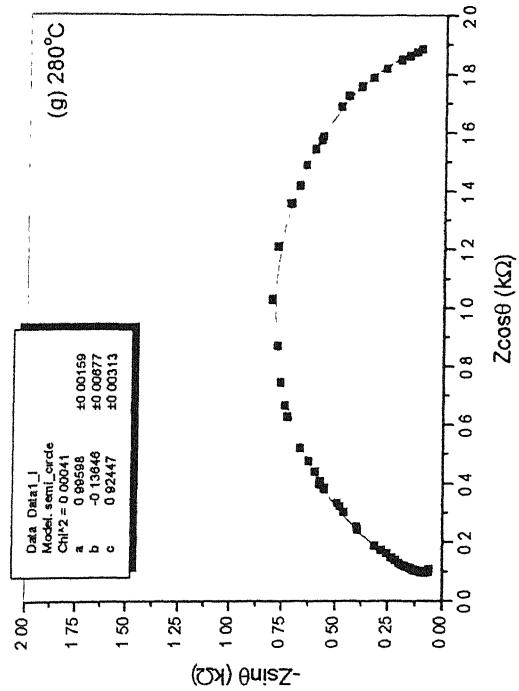
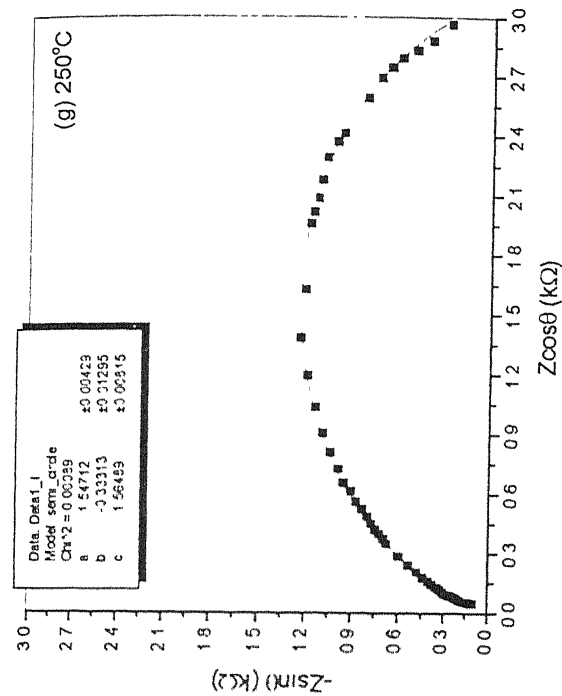
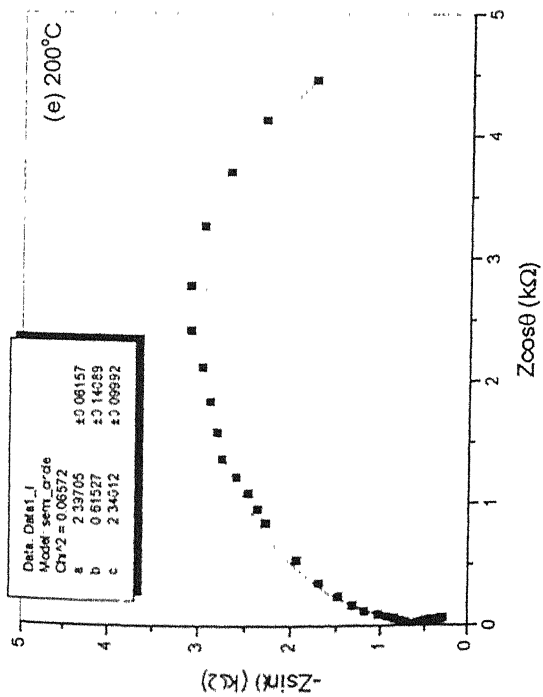
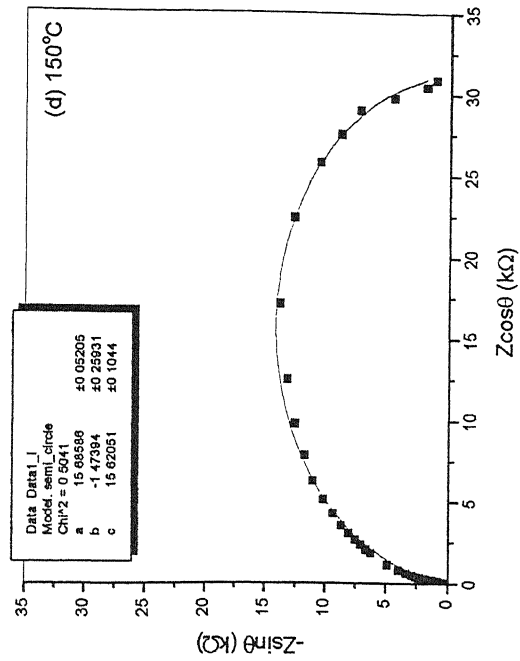
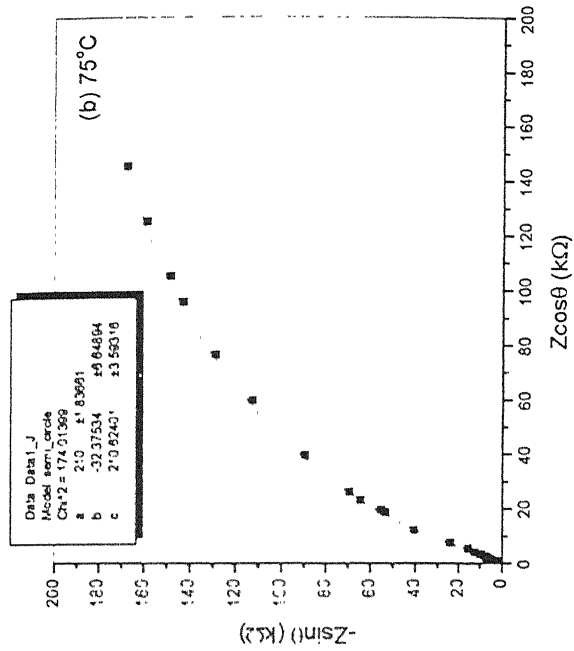
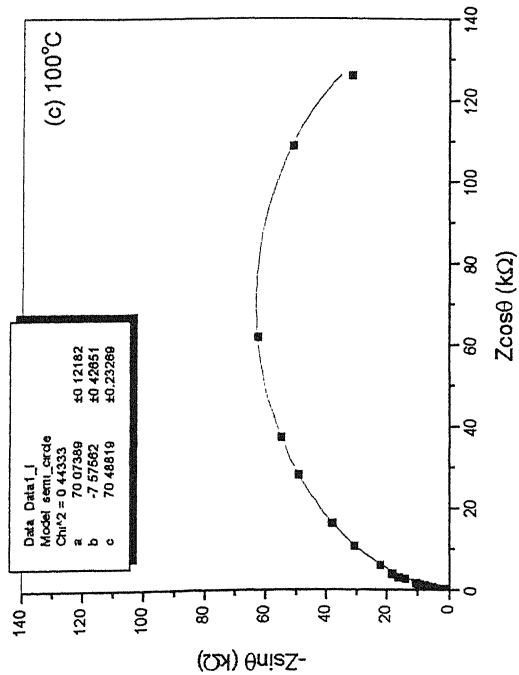
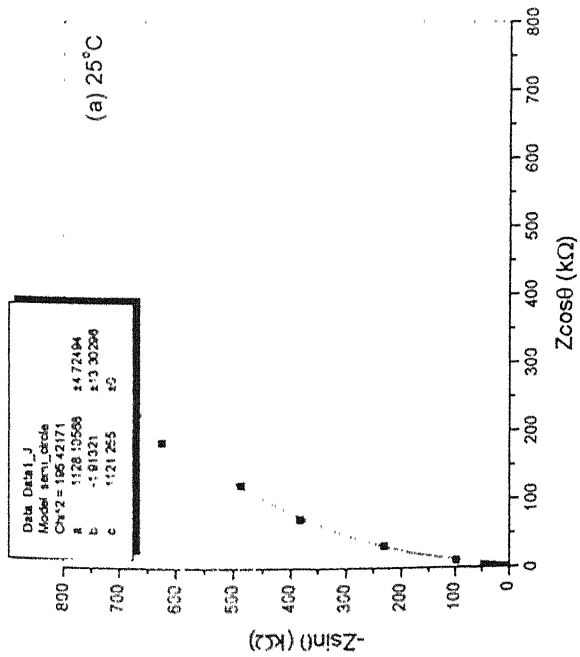


Fig. 3.11 Cole-Cole plots for 9 mole% $\text{Gd}_2\text{O}_3\text{-ZrO}_2$ thin film at different temperatures



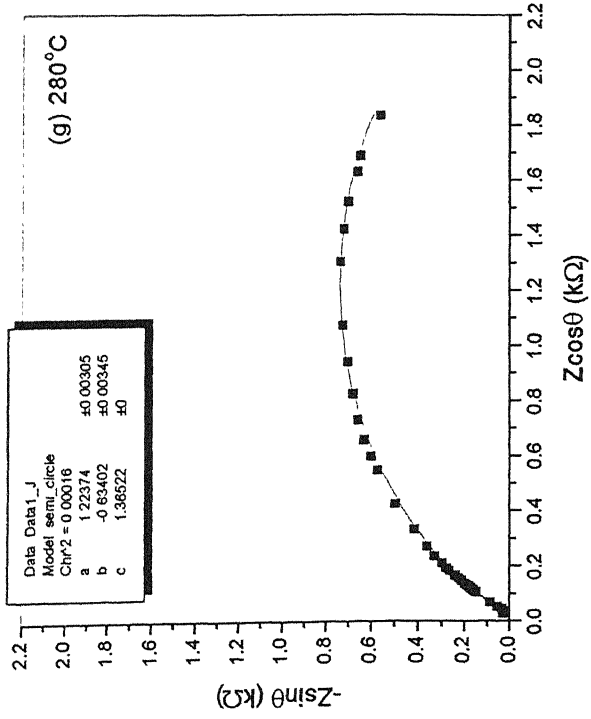
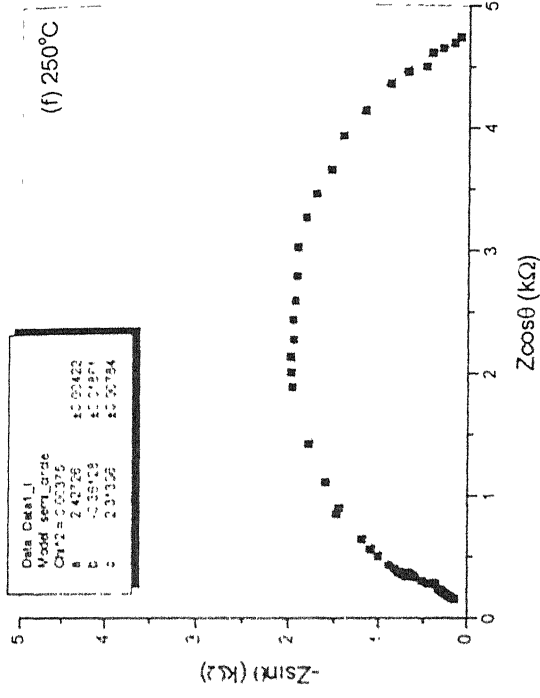
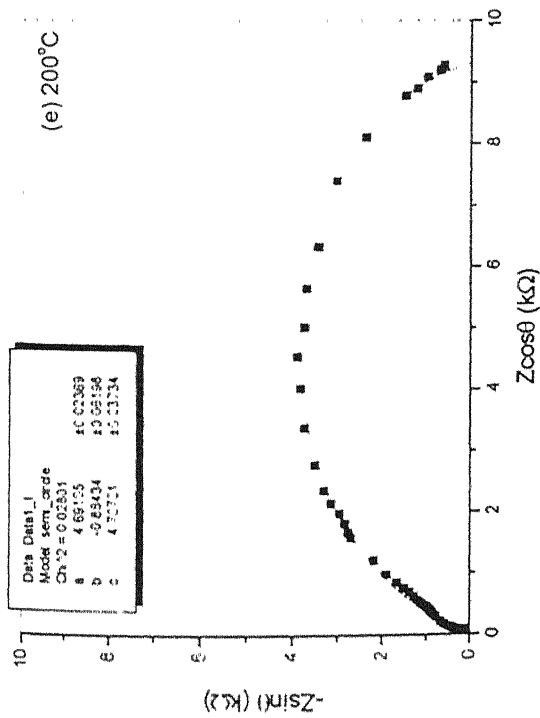
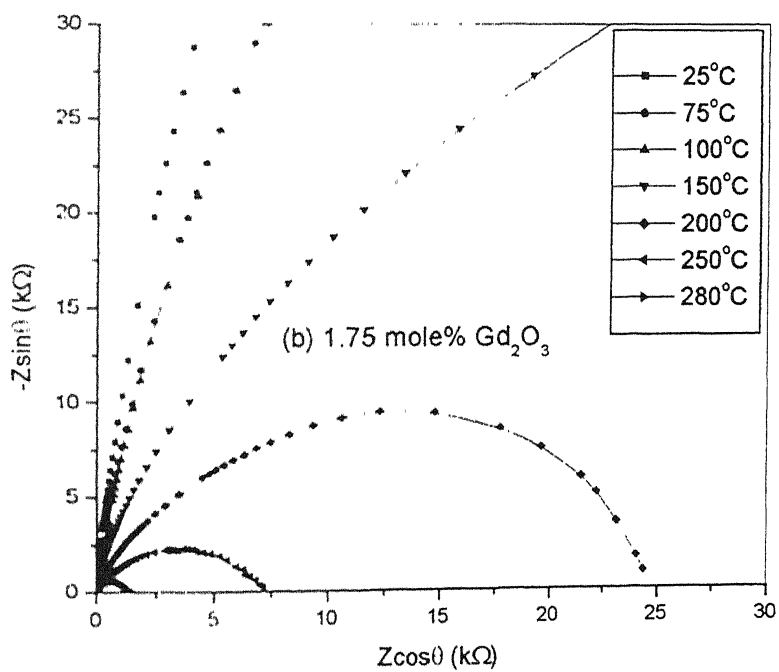
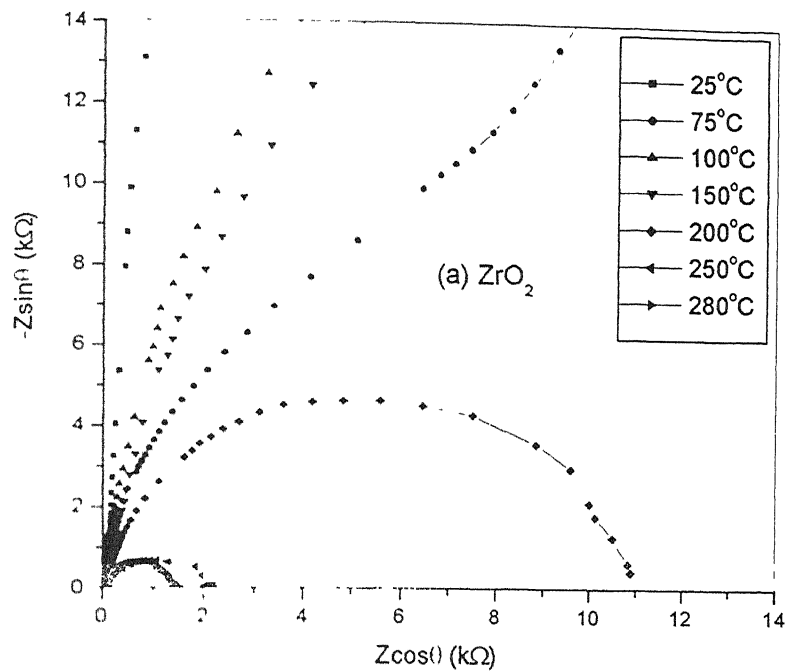
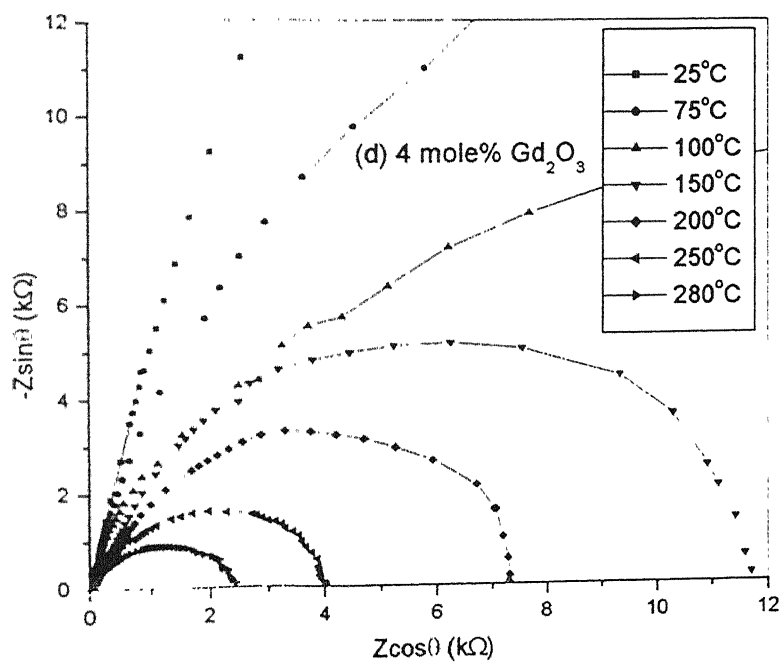
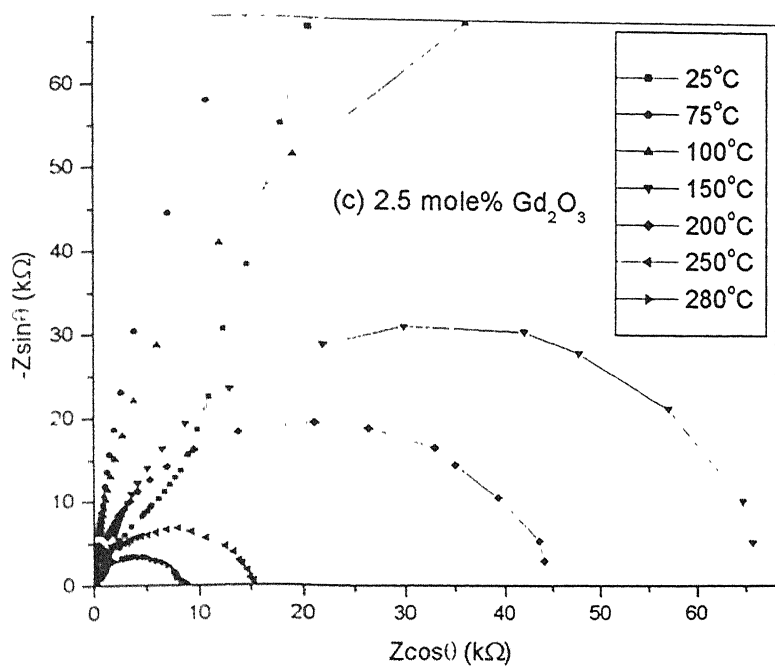
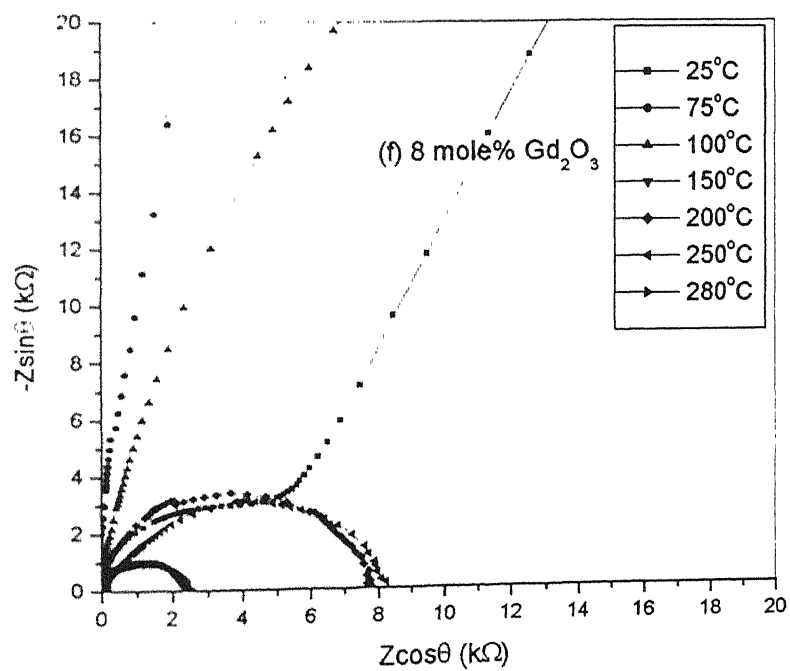
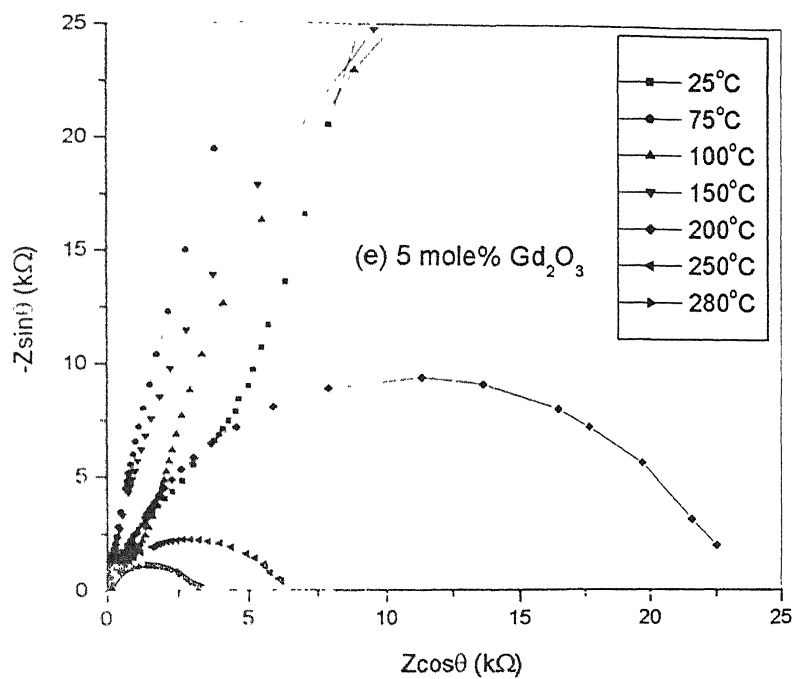


Fig. 3.12 Cole-Cole plots for 11 mole% $\text{Gd}_2\text{O}_3\text{-ZrO}_2$ thin film at different temperatures







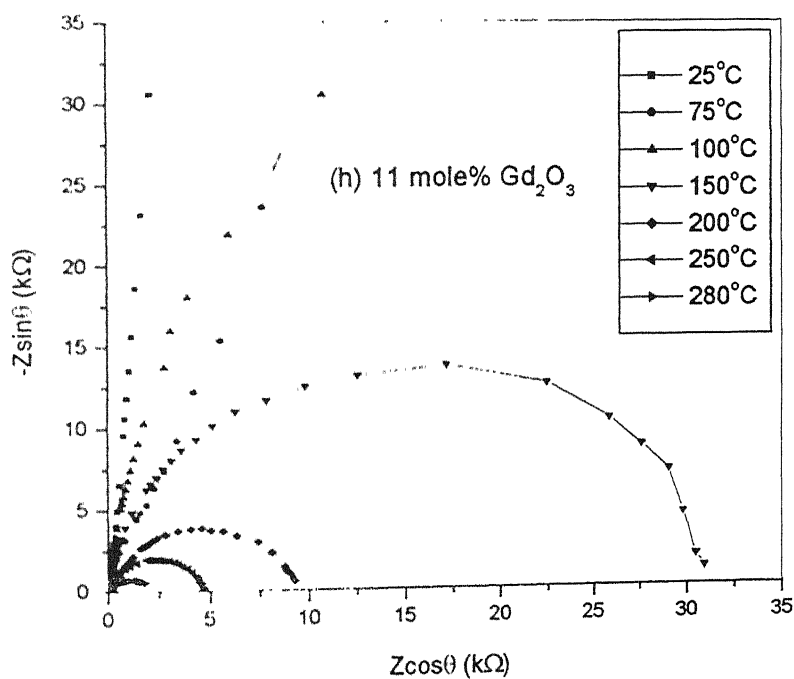
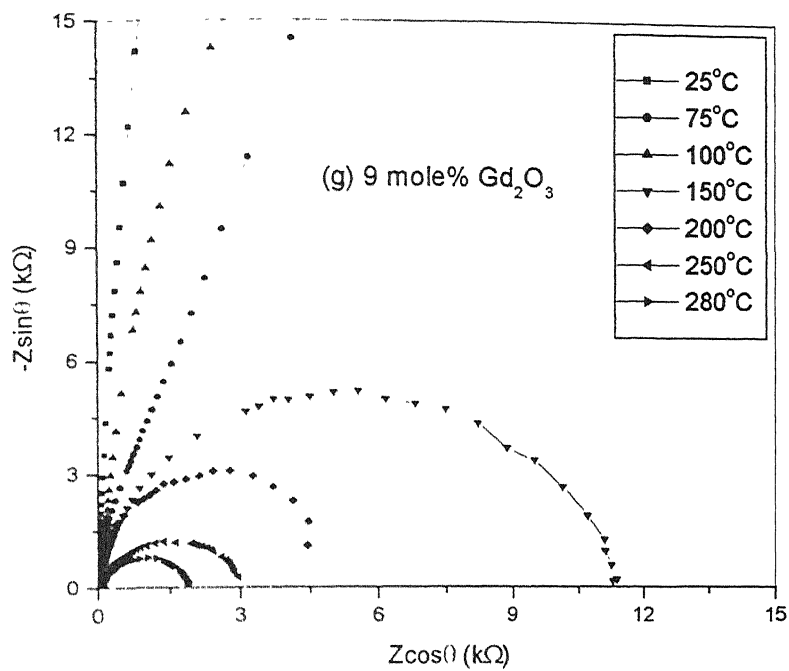
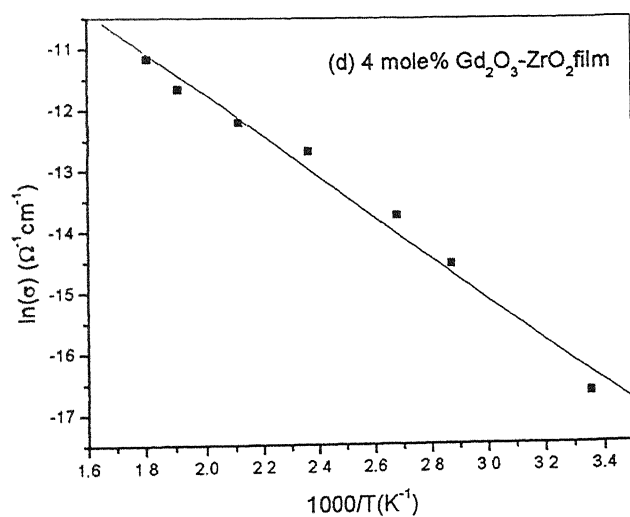
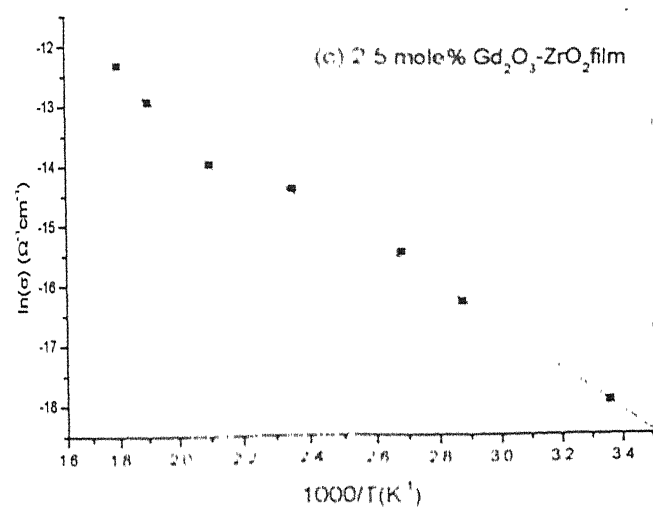
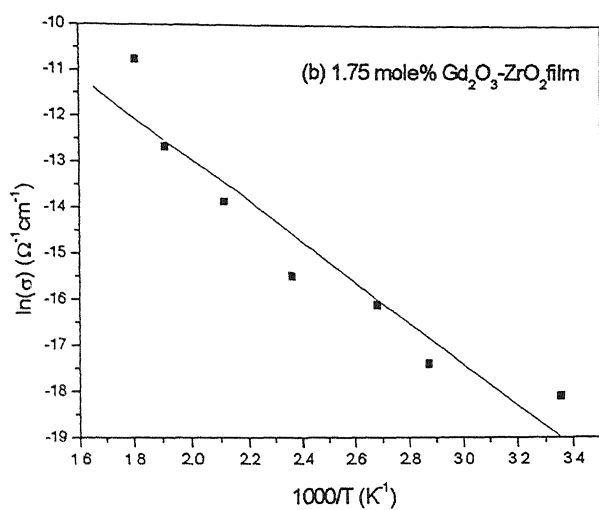
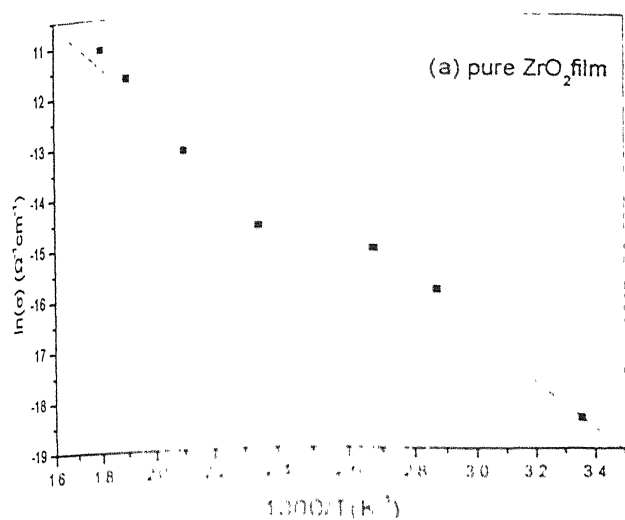


Fig. 3.13 Cole-Cole plots for pure and Gd_2O_3 - ZrO_2 films at different temperatures



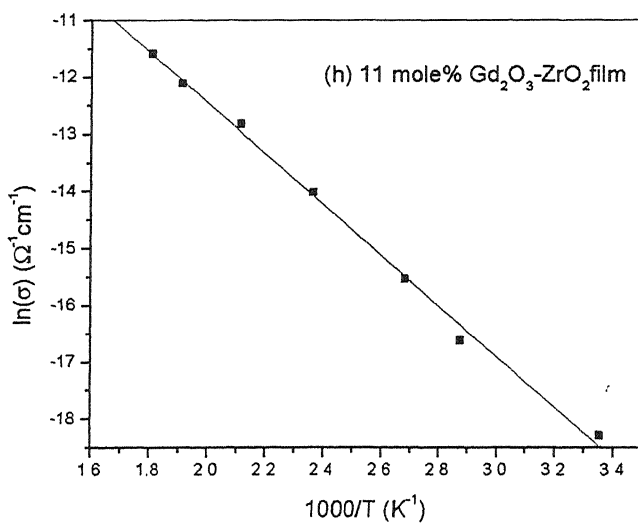
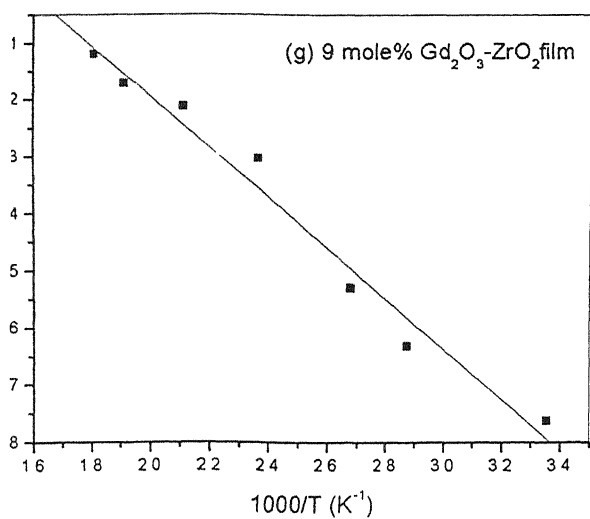
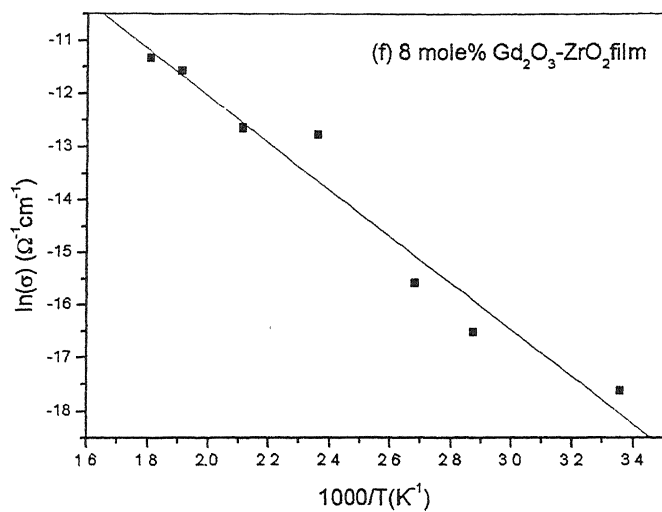
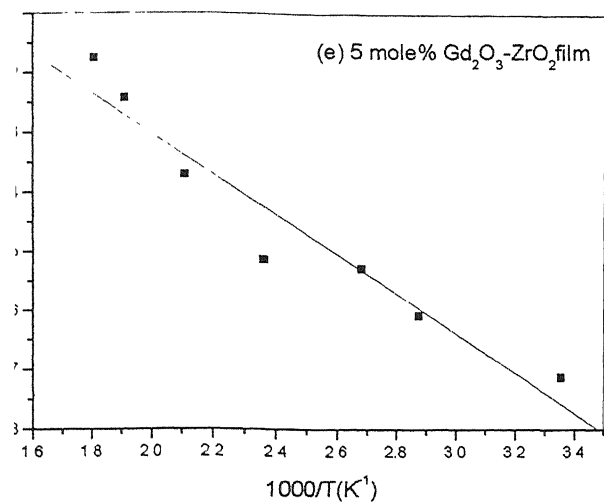


Fig. 3. 14 Arrhenius plots of dc conductivity for pure and Gd_2O_3 - ZrO_2 films

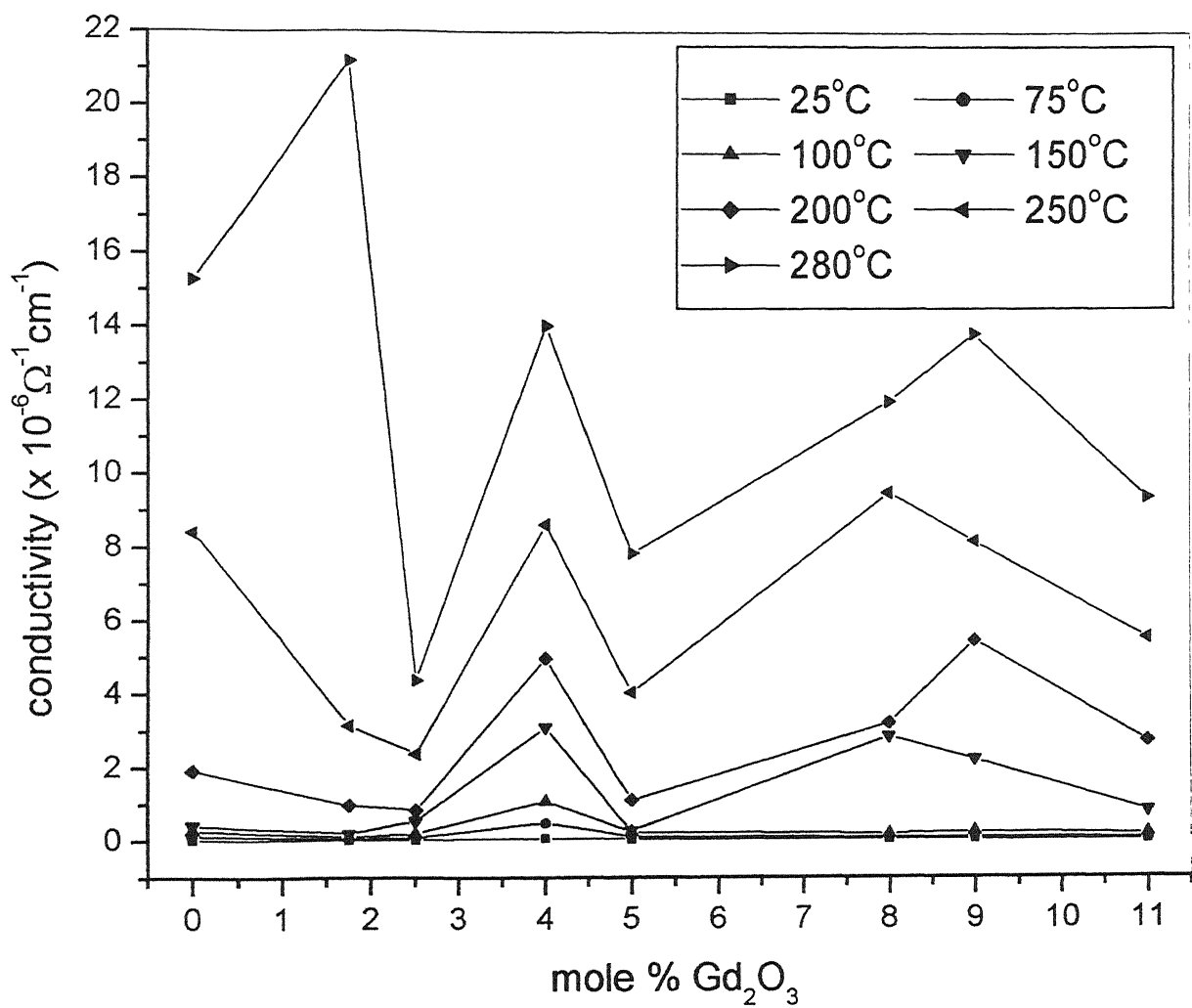


Fig.3.15 Variation of dc conductivity with temperature and Gd_2O_3 content

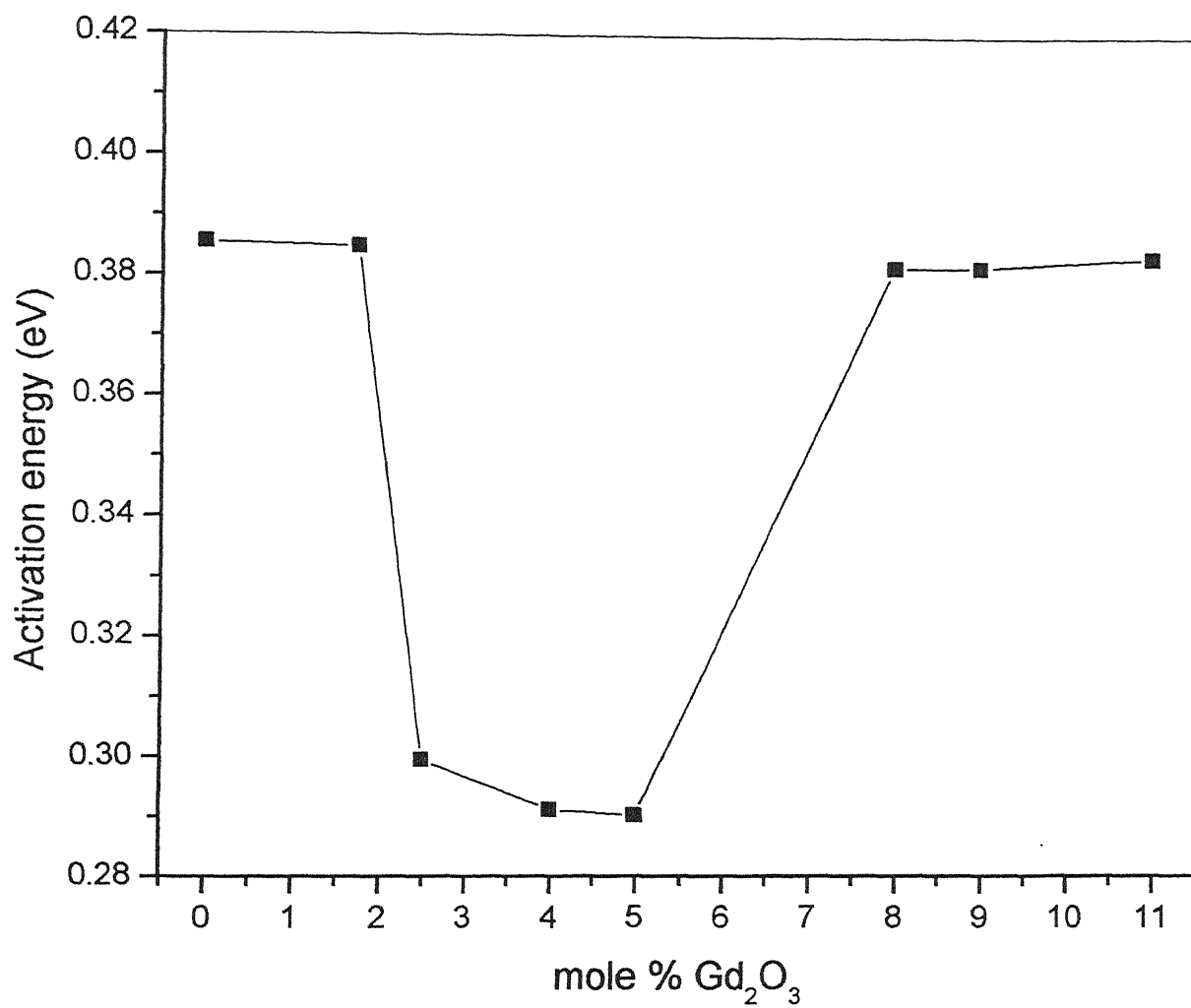
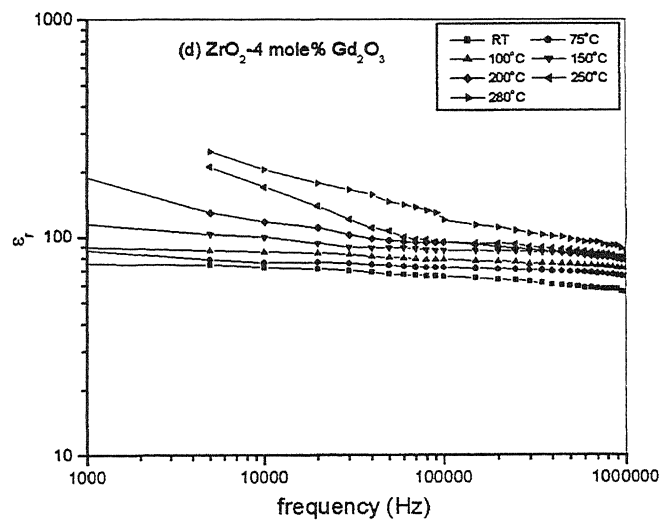
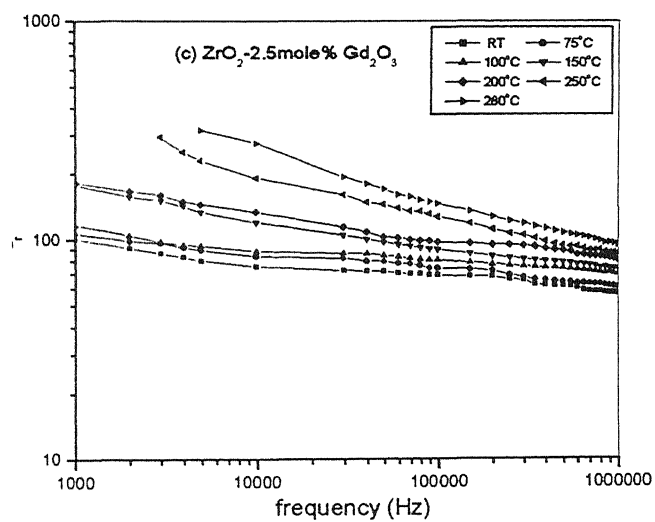
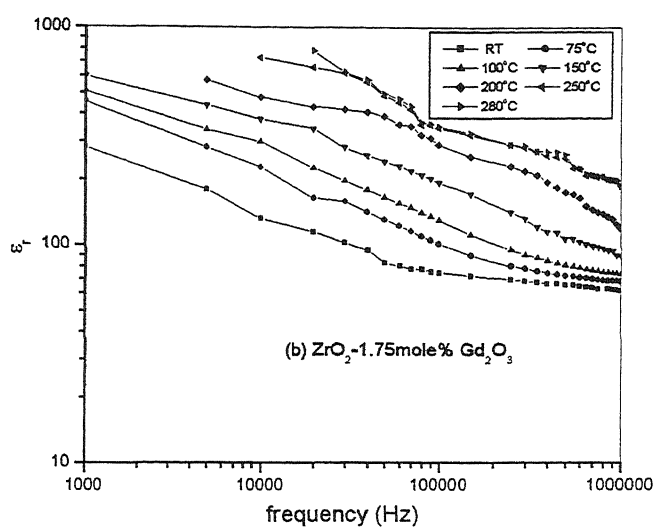
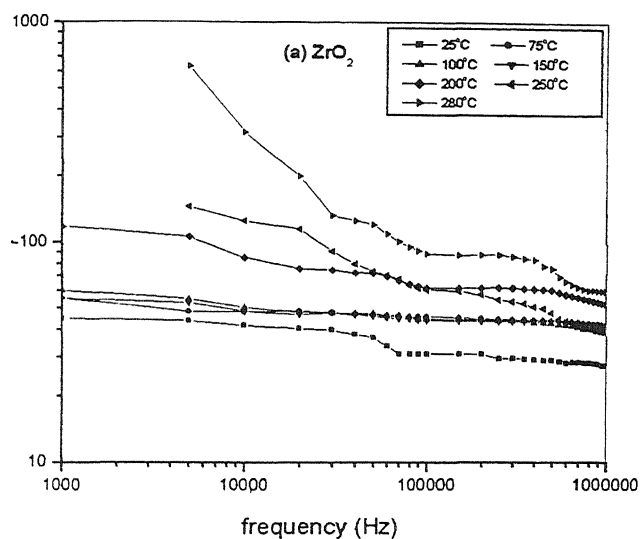


Fig.3.16 Variation of activation energy for conduction in pure and Gd_2O_3 - ZrO_2 films



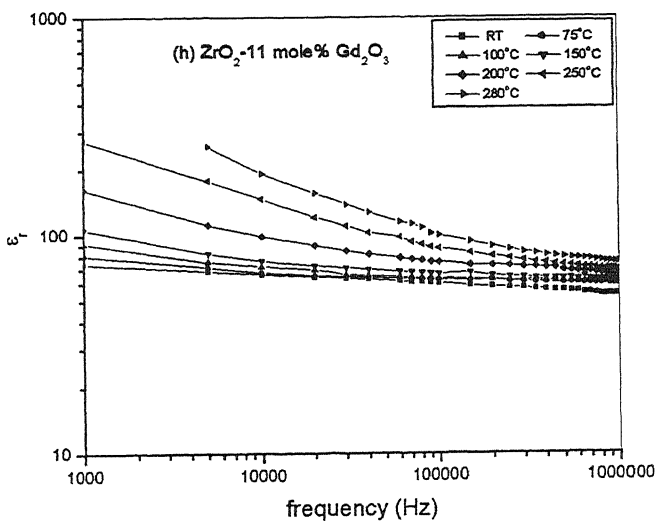
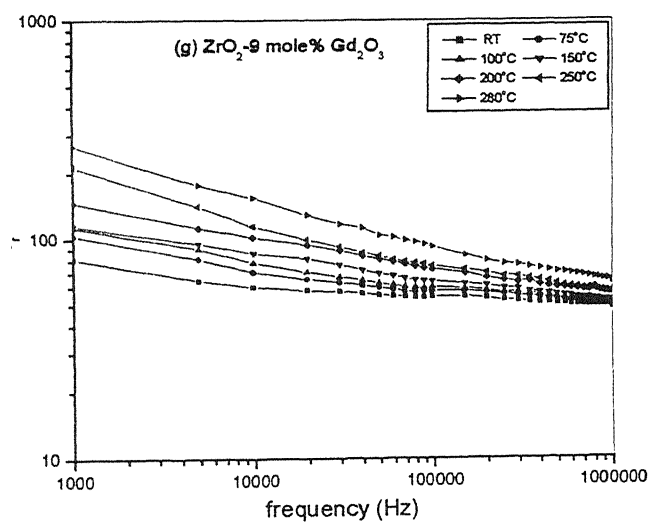
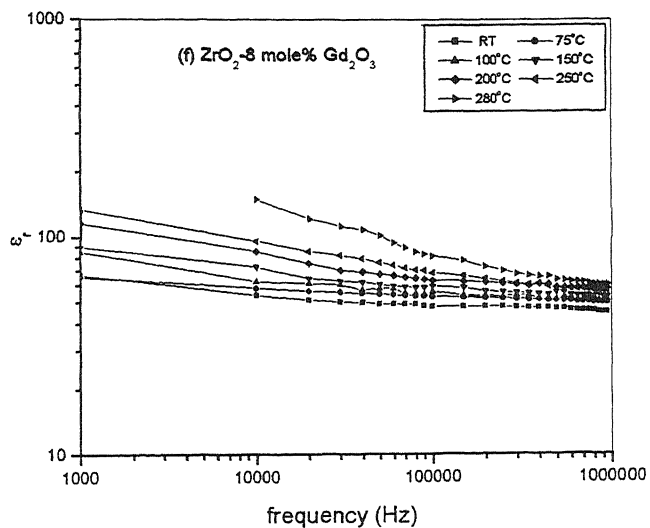
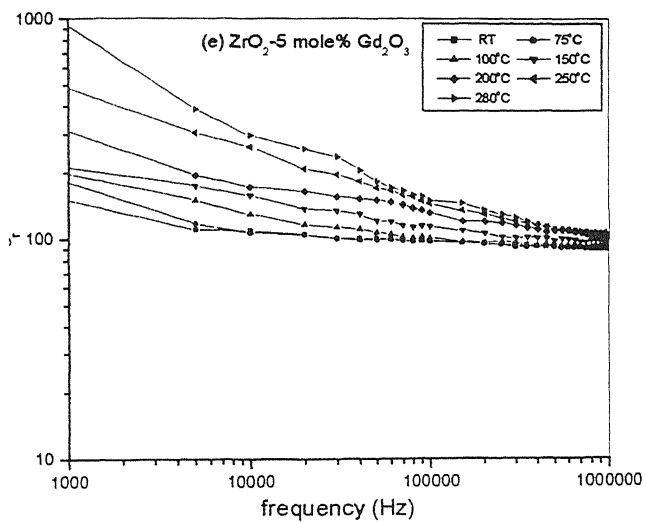
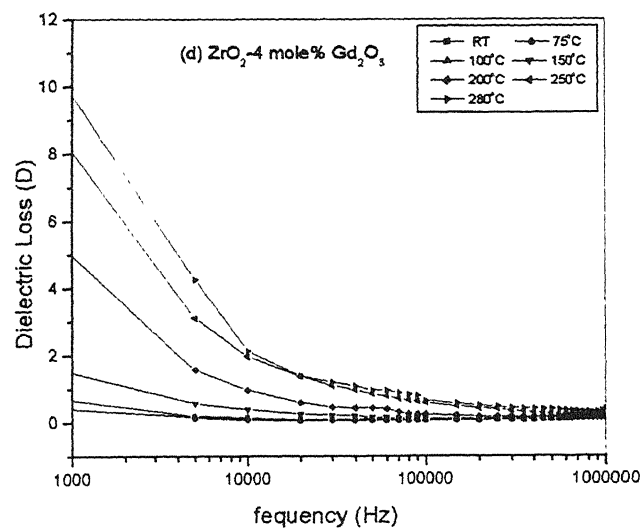
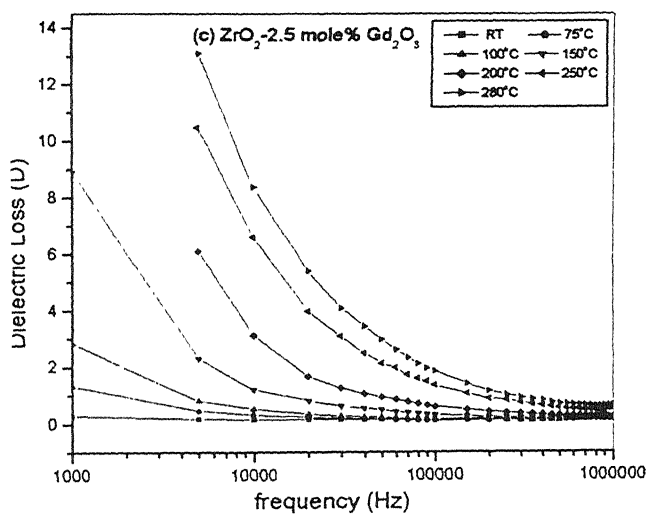
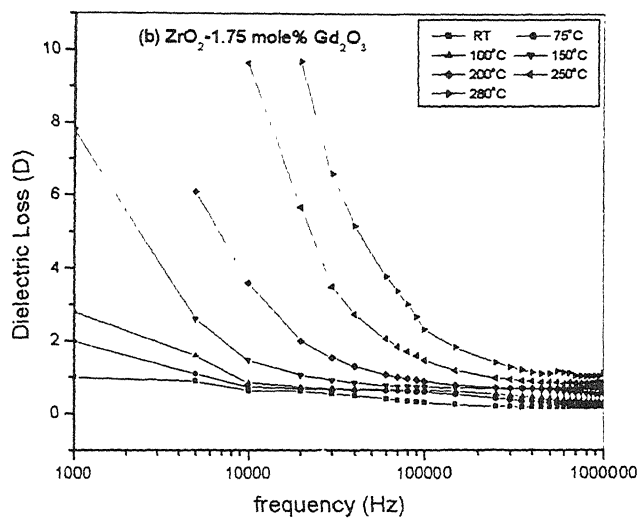
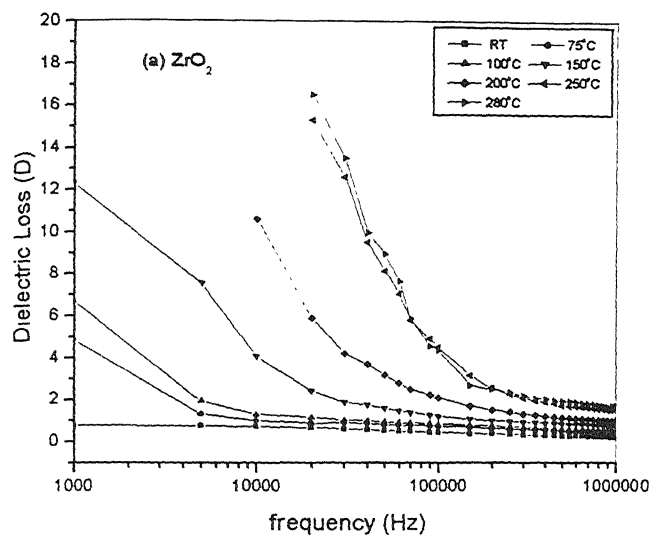


Fig.3.17 Frequency dependence of relative dielectric constant for ZrO_2 and Gd_2O_3 - ZrO_2 films at different temperatures.



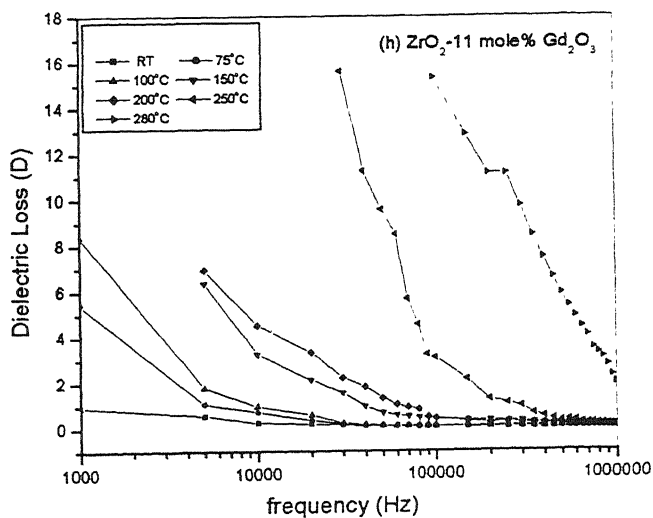
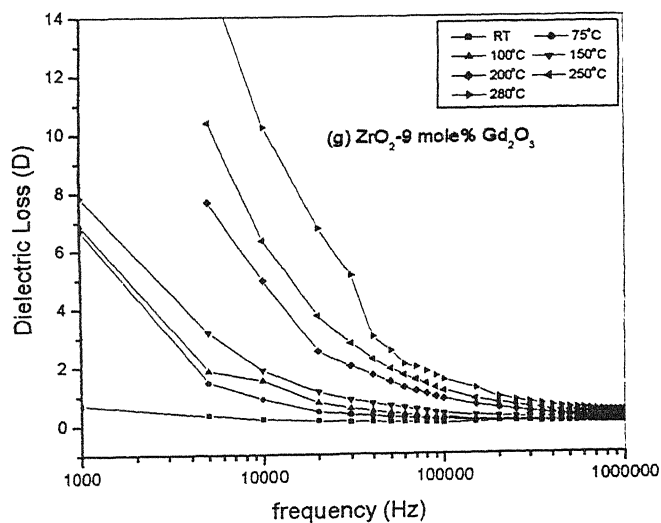
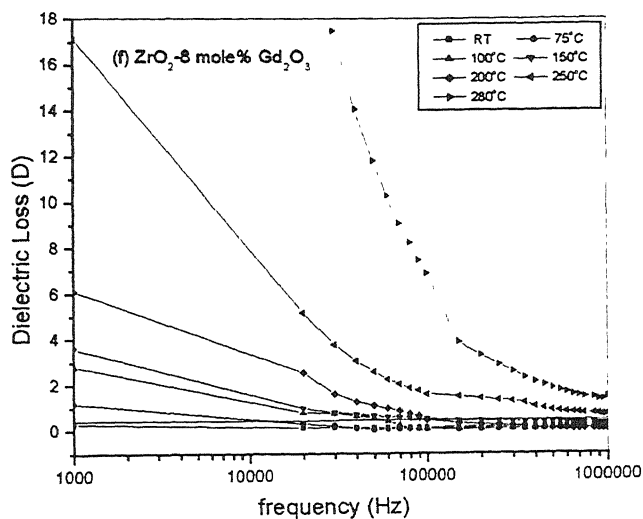
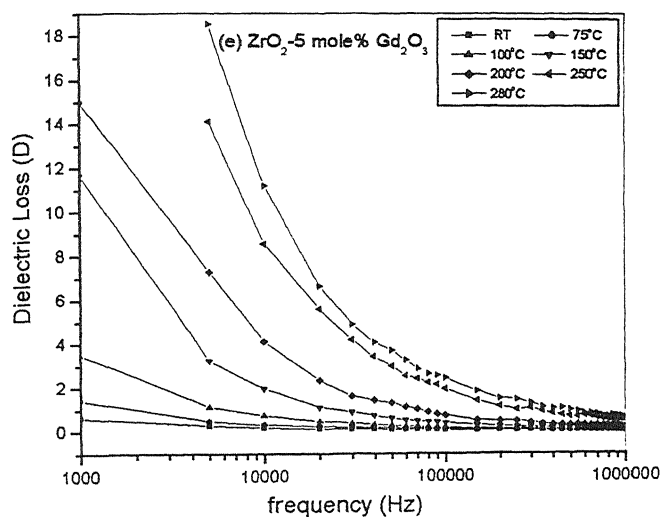


Fig.3.18 Frequency dependence of dielectric loss for ZrO_2 and Gd_2O_3 - ZrO_2 films at different temperatures.

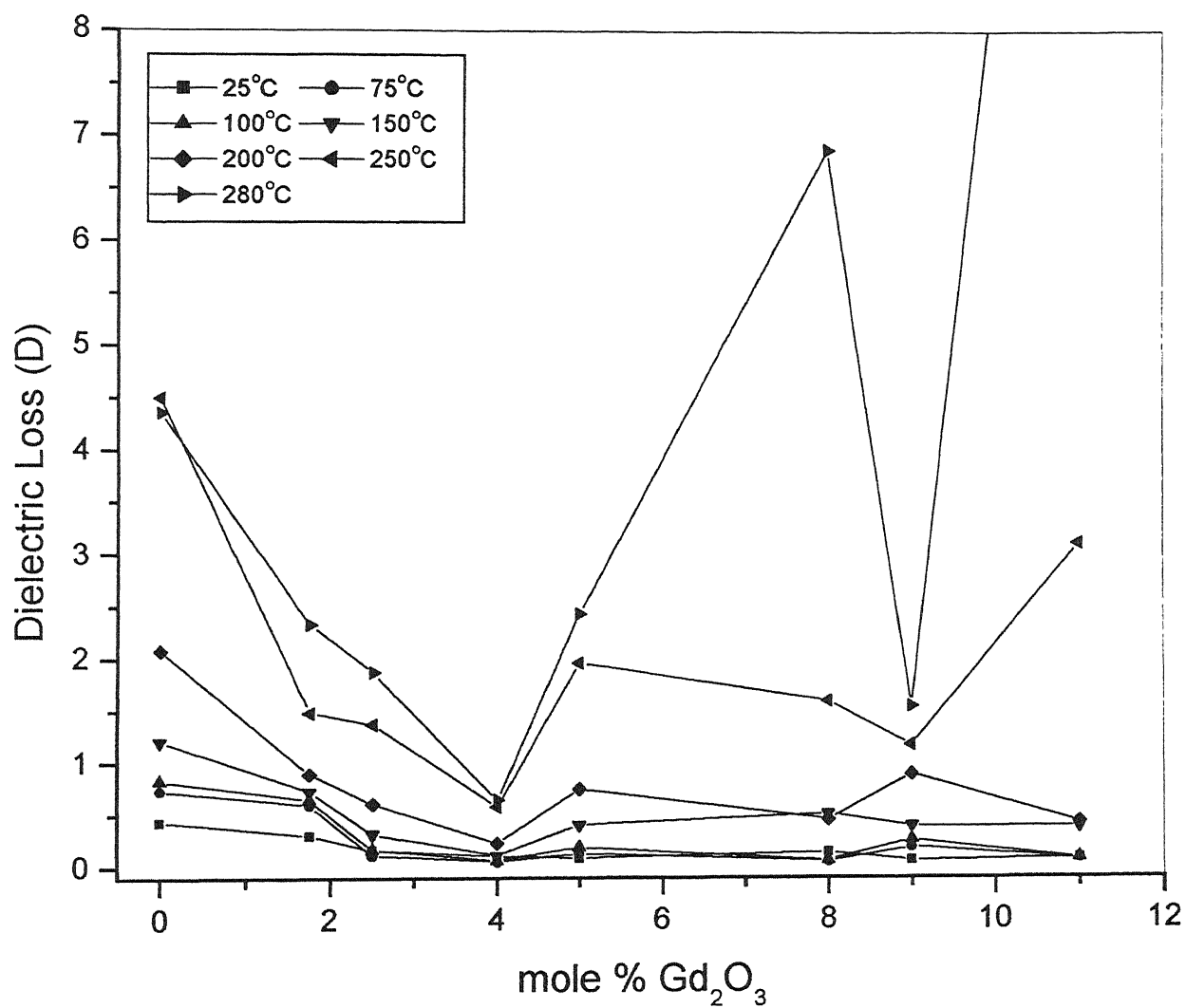


Fig. 3.19 Variation of dielectric loss with Gd_2O_3 content at 100kHz.

Table 3.1 Thickness of films prepared under different conditions

| S.No | Sol composition (mole% Gd_2O_3) | Sol concentration (M) | Temperature ($^{\circ}\text{C}$) /Time (min) | PVP/Zr | No. of coatings | Thickness (μm) |
|------|---|--------------------------|--|--------|--------------------|--------------------------------|
| 1 | 0.00 | 0.2 | 500/10 | 0.5 | 10 | 0.4 |
| 2 | 1.75 | 0.2 | 500/10 | 0.5 | 10 | 0.5 |
| 3 | 2.50 | 0.2 | 500/10 | 0.5 | 10 | 0.7 |
| 4 | 4.00 | 0.2 | 500/10 | 0.5 | 10 | 0.7 |
| 5 | 5.00 | 0.2 | 500/10 | 0.5 | 10 | 0.5 |
| 6 | 8.00 | 0.2 | 500/10 | 0.5 | 10 | 0.5 |
| 7 | 9.00 | 0.2 | 500/10 | 0.5 | 10 | 0.5 |
| 8 | 11.00 | 0.2 | 500/10 | 0.5 | 10 | 0.5 |

Table 3.2 Standard x-ray diffraction data for different zirconia phases

| Phase | 2 θ (Angle in degrees) | Intensity (%) | Plane (hkl) |
|--------------------------------------|----------------------------------|---------------|----------------|
| Monoclinic (m) (JCPDS: 13-0307) | 28.268 | 100 | T11 |
| | 31.57 | 65 | 111 |
| | 34.265 | 20 | 002 |
| Tetragonal (t) (JCPDS: 24-1164) | 29.832 | 100 | 101 |
| | 49.506 | 23 | 112 |
| | 59.428 | 15 | 211 |
| | 34.024 | 10 | 002 |
| Cubic (c) (JCPDS: 27-0997) | 30.510 | 100 | 111 |
| | 35.194 | 25 | 200 |
| | 50.688 | 50 | 220 |
| | 60.338 | 20 | 311 |
| Orthorhombic (o) (JCPDS: 34-1084) | 30.563 | 100 | 111 |
| | 34.184 | 75 | 002 |
| | 35.789 | 50 | 200 |
| | 50.991 | 100 | 202 |
| | 50.991 | 100 | 220 |
| | 59.023 | 50 | 113 |
| | 61.042 | 75 | 311 |
| | 63.647 | 50 | 222 |
| | 66.342 | 25 | 302 |

Table 3.3 X-ray diffraction analysis chart

(F = Fe-Cr, N = Cr-Fe-Ni, c = cubic, m = monoclinic, t = tetragonal)

| S.No. | Composition | 2 θ (Angle in degrees) | Intensity (%) | Plane (hkl) | Phase |
|-------|--|---|---|---|---------------------------------|
| 1 | ZrO ₂ - 0%Gd ₂ O ₃ | 30.79 43.91 44.91 51.02 60.27 65.04 74.79 | 34.92 35.11 100.00 20.71 8.28 14.82 28.58 | 111 100 100 200 311 200 220 | c N F N c F N |
| 2 | 1.75 mole% Gd ₂ O ₃ -ZrO ₂ | 30.17 44.77 50.90 59.67 64.90 74.67 | 26.97 100.00 14.47 6.96 19.57 20.82 | 111 100 200 311 200 220 | c F N c F N |

| | | | | | |
|---|--|-------|--------|-----|---|
| 3 | 2.5 mole% Gd ₂ O ₃ - ZrO ₂ | 29.47 | 34.04 | 101 | t |
| | | 34.47 | 12.99 | 020 | m |
| | | 43.29 | 23.31 | 100 | N |
| | | 44.34 | 97.79 | 100 | F |
| | | 49.45 | 14.61 | 112 | t |
| | | 50.45 | 16.61 | 200 | N |
| | | 59.02 | 8.26 | 211 | t |
| | | 64.62 | 11.27 | 200 | F |
| | | 74.44 | 34.04 | 220 | N |
| 4 | 4 mole% Gd ₂ O ₃ - ZrO ₂ | 30.30 | 20.61 | 111 | c |
| | | 44.60 | 99.52 | 100 | F |
| | | 49.60 | 7.57 | 112 | t |
| | | 50.60 | 11.93 | 200 | N |
| | | 59.95 | 6.15 | 311 | c |
| | | 64.65 | 17.00 | 200 | F |
| | | 74.55 | 22.87 | 220 | N |
| 5 | 5 mole% Gd ₂ O ₃ - ZrO ₂ | 30.31 | 27.62 | 111 | c |
| | | 34.43 | 11.13 | 020 | m |
| | | 35.24 | 10.10 | 200 | c |
| | | 43.69 | 30.43 | 100 | N |
| | | 44.69 | 100.00 | 100 | F |
| | | 50.83 | 18.12 | 200 | N |
| | | 60.08 | 6.92 | 311 | c |
| | | 64.66 | 22.43 | 200 | F |
| | | 74.57 | 41.65 | 220 | N |

| | | | | | |
|---|---|-------|--------|-----|---|
| 6 | 8 mole% Gd ₂ O ₃ - ZrO ₂ | 30.14 | 21.65 | 111 | c |
| | | 32.90 | 20.61 | | |
| | | 34.21 | 9.51 | 200 | m |
| | | 43.70 | 29.66 | 100 | N |
| | | 44.65 | 98.52 | 100 | F |
| | | 50.83 | 17.63 | 200 | N |
| | | 59.76 | 7.18 | 211 | t |
| | | 64.78 | 6.86 | 200 | F |
| | | 74.67 | 10.98 | 220 | N |
| | | 76.23 | 7.14 | | |
| 7 | 9 mole% Gd ₂ O ₃ - ZrO ₂ | 30.33 | 22.03 | 111 | c |
| | | 34.50 | 9.01 | 020 | m |
| | | 43.63 | 21.75 | 100 | N |
| | | 44.53 | 100.00 | 100 | F |
| | | 50.40 | 12.31 | 200 | N |
| | | 59.98 | 6.57 | 311 | c |
| | | 64.70 | 19.71 | 200 | F |
| | | 74.58 | 13.72 | 220 | N |
| 8 | 11 mole% Gd ₂ O ₃ - ZrO ₂ | 30.07 | 38.71 | 111 | c |
| | | 32.69 | 18.34 | | |
| | | 34.75 | 15.40 | 110 | t |
| | | 43.56 | 36.33 | 100 | N |
| | | 44.52 | 99.22 | 100 | F |
| | | 50.61 | 27.64 | 200 | N |
| | | 59.52 | 11.67 | 211 | t |
| | | 64.66 | 12.34 | 200 | F |
| | | 74.63 | 21.82 | 220 | N |

Table 3.4 Conductivity and activation energy values for pure and
Gd₂O₃-ZrO₂ thin films at different temperatures

| S.No. | Sample Details | Temperature (°C) | DC conductivity (σ) $\times 10^{-5}$ ($\Omega^{-1}\text{cm}^{-1}$) | Activation Energy(E_a) (eV) |
|-------|---|---|---|---------------------------------------|
| 1. | Pure ZrO ₂ Film | 25 75 100 150 200 250 280 | 0.01024 0.12428 0.27168 0.41483 1.90417 8.39194 15.25598 | 0.385 |
| 2. | 1.75 mol% Gd ₂ O ₃ - ZrO ₂ film | 25 75 100 150 200 250 280 | 0.01392 0.02857 0.10119 0.1904 0.9624 3.13285 21.1757 | 0.384 |
| 3. | 2.5 mol% Gd ₂ O ₃ - ZrO ₂ film | 25 75 100 150 200 250 280 | 0.01615 0.08299 0.18973 0.5411 0.82715 2.36227 4.36872 | 0.299 |

Table 3.5 Comparison of grain boundary conductivity in bulk and thin film samples at ~280°C

| Mole % Gd ₂ O ₃ | Bulk Samples ⁴⁴ | | Thin Film | | | |
|--|---|---------------------------|---|-----------------|---------------------------|-----------------|
| | Conductivity ($\Omega^{-1}\text{cm}^{-1}$) $\times 10^{-6}$ | Activation Energy (eV) | Conductivity ($\Omega^{-1}\text{cm}^{-1}$) $\times 10^{-6}$ | | Activation Energy (eV) | |
| | | | ref. 40 | Present Work | ref. 40 | Present work |
| 0 | - | - | 128 | 15.25 | 0.36 | 0.385 |
| 1.75 | - | - | 268 | 21.17 | 0.39 | 0.384 |
| 2.5 | 0.60 | 0.75 | 1.37 | 4.37 | 0.40 | 0.299 |
| 4 | 0.65 | 1.11 | 2.88 | 13.99 | 0.31 | 0.291 |
| 5 | 0.20 | 1.04 | 2.1 | 7.81 | 0.37 | 0.290 |
| 8 | 0.40 | 1.12 | 0.9 | 11.94 | 0.28 | 0.381 |
| 9 | 0.60 | 0.92 | 0.6 | 13.77 | 0.27 | 0.381 |
| 11 | 1.50 | 0.85 | 0.8 | 9.33 | 0.30 | 0.383 |

Summary and Conclusions

The aim of this work was to investigate the electrical properties of Gd_2O_3 doped ZrO_2 thin films synthesized by the sol-gel process. As aliovalent impurities of lower valence are introduced in solid solution in ZrO_2 , oxygen valence defects are created and the electrical conductivity of ZrO_2 increases. Gd_2O_3 is chosen as a dopant in ZrO_2 because the properties of Gd_2O_3 - ZrO_2 system are not so well investigated as with other dopants such as Y_2O_3 and other R_2O_3 type dopants.

The conclusions of this work are as follows: -

- (i) The use of polymer poly-vinyl pyrrolidone (PVP) in the sol helps in obtaining thicker crack free films. It is found that at $\text{PVP/Zr} = 0.5$ molar ratio, the films are almost crack free when the drying temperature is $\sim 125^\circ\text{C}$.
- (ii) The thickness of ZrO_2 and Gd_2O_3 - ZrO_2 film is in the range of 0.4 to 0.7 μm for 10 coatings. The RMS surface roughness value of 0, 5, 9 mole% Gd_2O_3 - ZrO_2 film was found to be ~ 0.67 , 0.81 and 6.42 nm respectively for a scan area of 300 x 300nm, while the RMS surface roughness value for polished stainless steel substrate was found to be ~ 1.18 nm for a scan area of 1000 x 1000 nm.
- (iii) The optical microscopic observations show that the as deposited and dried films ($\sim 125^\circ\text{C}$) from 0.2 M sol are crack free but the films dried at $\sim 200^\circ\text{C}$ developed cracks. Increasing the heat treatment temperature from 500°C to 700°C again causes crack formation in the

min due to oxidation of steel. Hence the heat treatment temperature should be limited to 500°C

- (iv) Due to the use of a lower crystallization temperature, the films have a very fine grain size giving rise to broad x-ray peaks. This makes the unambiguous interpretation of the x-ray data difficult. However, x-ray data, combined with the trends in the electrical conductivity, lead to the conclusion that the films tend to crystallize into phases as expected from the composition i.e. monoclinic (m) phase for 0 and 1.75 mole % Gd_2O_3 , tetragonal (t) phase for 4 mole % Gd_2O_3 , cubic (c) phase for 9 mole % Gd_2O_3 and mixed phases for the intermediate composition.
- (v) According to AFM phase analysis, the 0 and 5 mole % $\text{Gd}_2\text{O}_3\text{-ZrO}_2$ films have grain size of the order of 10-25nm, while the 9 mole % film has somewhat coarser grains.
- (vi) The Cole-Cole plots of $\text{Gd}_2\text{O}_3\text{-ZrO}_2$ films of all compositions consist of one semicircle. This is believed to be due to the grain boundary conductivity, as this is the dominant conduction path due to fine grain size of the films. The dc conductivity for the thin films increases as the temperature is increased for the films of all compositions. The present data of the thin films is compared with that for the bulk samples. It is seen that the conductivity for thin films is larger by a factor of more than 10 for all $\text{Gd}_2\text{O}_3\text{-ZrO}_2$ films. In case of Y_2O_3 containing ZrO_2 films, the conductivity for the thin films and the bulk samples have been found to be nearly equal by Chun and Mizutani²⁹.
- (vii) The conductivity has high values for compositions that fall in the single-phase region (m for 1.75 %, t for 4 % and c for 8-9 mole %) and is low in the intermediate compositions corresponding to the intermediate regions.
- (viii) The activation energy for conduction is about 0.29 eV for the compositions in the tetragonal (t) phase region and 0.38 eV in the monoclinic (m) and cubic (c) phase regions. The activation energy for $\text{ZrO}_2\text{-3mol\% Y}_2\text{O}_3$ thin film is 1.22 eV as reported by Chun and

Mizutani²⁹. The activation energy for grain conduction in bulk $\text{Gd}_2\text{O}_3\text{-ZrO}_2$ samples is found to vary between 0.6 eV to 1 eV with Gd_2O_3 concentrations between 1.75 to 11 mole %⁴⁴. However, we obtained much lower values (0.29 to 0.38 eV) in the thin film samples on stainless steel substrate. The values in the same range was reported by Yeh et. al.³¹. It appears that thermal annealing (at 250°C after electrode deposition) reduces the activation energy for electrical conduction due to free oxygen vacancies. The substrate and the phase of the film have a significant effect on the conductivity of thin films. The activation energy decreases with an increase in Gd_2O_3 content and then again increases after 5 mole % Gd_2O_3 addition. The same trend was observed in YSZ single crystals by Hartmanova et. al.⁸. It is suggested that the decrease in activation energy can be attributed to- (a) the interaction or clustering of the vacancies, (b) ordering of the vacancies and (c) the formation of a second phase. This is related to the phase changes in the film due to different Gd_2O_3 contents. In the $\text{Y}_2\text{O}_3\text{-ZrO}_2$ films, activation energy is found to increase with increasing Y_2O_3 in the c phase region implying a clustering of vacancies. But this was not observed in the $\text{ZrO}_2\text{-Gd}_2\text{O}_3$ films.

- (ix) The dielectric constant has very high values at lower frequencies and decreases rapidly at higher frequencies for thin films of all compositions. Also, the dielectric constant increases rapidly as the temperature is increased. At temperatures higher than 150°C the increase in the dielectric constant is associated with the presence of space charge polarization⁴⁷. At higher frequencies (>1MHz), the space charge polarization is negligible and only the dipolar, ionic and electronic polarization contribute to the total permittivity. However, in the bulk samples of $\text{Gd}_2\text{O}_3\text{-ZrO}_2$ ⁴⁴, the dielectric constant is very high (~ 300 at higher frequencies) compared to our thin film samples (<60 at higher frequencies for almost all films). In thin films, no distinct step in the plots is observed as the dominant conduction mechanism changes from grain to grain boundary.

(A) The dielectric loss decreases rapidly below 100 kHz frequencies for all the compositions. At higher frequencies, it is almost constant. However, dielectric loss increases with increase in temperature. All the doped samples show similar behavior.

References:

1. Michael Hu, R. D. Hunt, E.A. Payzant, and C. R. Hubbard, "Nanocrystallization and Phase Transformation in Monodispersed Ultrafine Zirconia Particles From Various Homogeneous Precipitation Methods", *J. Am. Ceram. Soc.*, 82 (9) pp. 2313-20 (1999)
2. S. Rossignol, Y. Madier and D. Duprez, "Preparation of Zirconia-Ceria Materials by Soft Chemistry", *Catalysis today* 50 pp. 261-270 (1999).
3. N. Shibata, J. Katamura, A. Kuwabara, Y. Ikuhara and T. Sakuma, "The Instability and Resulting Phase Transition of Cubic Zirconia", *Materials Science and Engineering A* 312 pp. 90-98 (2001).
4. C. J. Howard, E. H. Kisi, R. B. Roberts and R. J. Hill, "Neutron Diffraction Studies of Phase Transformations between Tetragonal and Orthorhombic Zirconia in Magnesia-Partially-Stabilized Zirconia", *J. Am. Ceram. Soc.*, 73 (10) pp. 2828-33 (1990).
5. Yawen Zhang, Shu Jin, Chunsheng Liao and C. H. Yan, "Microstructures and Optical Properties of Nanocrystalline Rare Earth Stabilized Zirconia Thin Films Deposited by a simple Sol-Gel Method", *Materials Lett.*, 56 (6) pp. 1030-1034 (2002).
6. H. Li, K. Liang, L. Mei, S. Gu and S. Wang, "Oxidation Protection of Mild Steel by Zirconia Sol-Gel Coatings", *Materials Lett.*, 51 pp. 320-324 (2001).
7. R. S. Niranjana, S. D. Sathaye and I. S. Mulla, "Bilayered Tin Oxide: Zirconia Thin Film as a Humidity Sensor", *Sensors and Actuators B* 81 pp. 64-65 (2001).
8. M. Hartmanova, J. Schneider, V. Navratil, F. Kundracik, H. Schulz and E. E. Lomonova, "Correlation Between Microscopic and Macroscopic Properties of Yttria Stabilized Zirconia", *Solid State Ionics* 136-137 pp. 107-113 (2000).
9. O. Ohtaka, T. Yamanaka, S. Kume, E. Ito and A. Navrotsky, "Stability of Monoclinic and Orthorhombic Zirconia: Studies by High-Pressure Phase Equilibria and Calorimetry", *J. Am. Ceram. Soc.*, Vol. 74(3), pp. 505-509 (1991).
10. R. E. Cohen, M. J. Mehl and L. L. Boyer, "Phase Transitions and Elasticity in Zirconia", *Physica B* 150, pp. 1-9 (1988).
11. F. Moztafzadeh, "Conductivity Measurements of Gd_2O_3 Stabilized ZrO_2 up to 2300K", *Advances in Ceramics*, Vol. 24B, Science and Technology of Zirconia III, p 901-905.
12. R. Ramamoorthy, D. Sundararaman, S. Ramasamy, " Ionic Conductivity Studies of Ultrafine-Grained Yttria Stabilized Zirconia Polymorphs ", *Solid State Ionics*, 123 pp. 271-278 (1999).

13. T. Mori, J. Drennan, Jong-heun Lee, Ji-Guaang Li and T. Ikegami, " Improving the Ionic Conductivity of Yttria-Stabilized Zirconia Electrolyte Materials", *Solid State Ionics*, 154-155 pp. 529-533 (2002).
14. J. R. MacDonald, " Impedance Spectroscopy ", John Wiley & Sons (1987).
15. Jean-Claude M'Peko, D. L. Spavieri Jr., C L. da Silva, C. A. Fortulan, D. P. F. de Souza and M. F. de Souza, " Electrical Properties of Zirconia-Alumina Composites", *Solid State Ionics*, 156 pp. 59-69 (2003).
16. I. Kosacki, H. U. Anderson, Y. Mizutani and K. Ukai, " Nonstoichiometry and Electrical Transport in Sc-doped Zirconia", *Solid State Ionics*, 152-153 pp. 431-438 (2002).
17. J. Luo, D. P. Almond and R. Stevens, " Ionic Mobilities and Associated Energies from an Analysis of Electrical Impedance of ZrO_2 - Y_2O_3 Alloys", *J. Am. Ceram. Soc.*, 83 (7) pp. 1703-1708 (2000).
18. E. N. S. Muccillo and D. M. Avila, " Impedance Spectroscopy of Tetragonal Zirconia Polycrystals doped with Ceria", *Materials Lett.*, 56 pp. 454-459 (2002).
19. A. Tsoga, A. Naoumidis and D. Stover, " Total Electrical Conductivity and Defect Structure of ZrO_2 - CeO_2 - Y_2O_3 - Gd_2O_3 Solid Solutions", *Solid State Ionics*, 135 pp. 403-409 (2000).
20. J. D. Solier, M.A. Perez-Jubindo, A. Dominguez-Rodriguez, and Arthur H. Heuer, " Low-Temperature Ionic Conductivity of 9.4-Mol%-Yttria-Stabilized Zirconia Single Crystals ", *J. Am. Ceram. Soc.*, 72 (8) pp. 1500-1502 (1989).
21. V. V. Srdic and R. P. Omorjan, " Electrical Conductivity of Sol-Gel Derived Yttria-Stabilized Zirconia", *Ceramics International* 27 pp. 859-863 (2001).
22. U. Shultz, K. Fritscher, C. Leyens and M. Peters, " Influence of Processing on Microstructure and Performance of Electron Beam Physical Vapor Deposition (EB-PVD) Thermal Barrier Coatings", *Journal of Engineering for Gas Turbines and Power*, Vol. 124, pp. 229-234 (2002).
23. H. Li, K. Liang, L. Mei and S. Gu, "Oxidation Protection of Mild Steel by Zirconia Sol-Gel Coatings." *Materials Science and Engineering A* 341(1-2) pp. 87-90 (2003).
24. M. J. Paterson and B. Ben-Nissan, "Multilayered sol-gel zirconia coatings on 316 stainless steel", *Surface and Coatings Technology* 86-87 pp. 153-158 (1996).
25. M. J. Paterson, D. G. McCulloch, P. J. K. Paterson and Besim Ben-Nissan, " The morphology and structure of sol-gel zirconia films on stainless steel." *Thin Solid Films* 311 pp. 196-206 (1997).

26. A. Mehner, H. Klumper-Westkamp, F. Hoffmann and P. Mayer, "Crystallization and residual stress formation of sol-gel-derived zirconia films." *Thin Solid Films* 308-309 pp.363-368 (1997).
27. R. Di Maggio, A. Tomasi and P. Scardi, "Characterization of Thin Ceramic Coatings on Metal Substrates", *Materials Lett.* 31 pp. 345-349 (1997).
28. F. Kundracik, M. Hartmanova, J. Mullerova, M. Jergel, I. Kostic and R. Tucoulou, "Ohmic Resistance of Thin Yttria Stabilized Zirconia Film and Electrode-Electrolyte Contact Area", *Materials Science and Engineering B* 84 pp. 167-175 (2001).
29. S. Y. Chun and N. Mizutani, "The Transport Mechanism of YSZ Thin Films Prepared by MOCVD", *Applied Surface Science*, 171 pp 82-88 (2001)
30. S. Charpentier, P. Fragnaud, D. M. Schleich and E. Gehain, "Preparation of Thin Film SOFCs Working at Reduced Temperature", *Solid State Ionics*, 135 pp. 373-380 (2000).
31. W. Yeh, C. Patuwathavithane and R. H. Zee, "Electrical Properties of Vapor-Deposited Yttria-Stabilized Zirconia Thin Films", *J. Appl. Phys.* 79 (10), pp. 7809-7813 (1996).
32. Santanu Bhattacharyya, PhD thesis under Prof. D. C. Agrawal, IIT-Kanpur (1995).
33. S. D. Dubey, "Preparation of Thick PZT Films by Sol Gel Method Using PVP as a Processing Aid and Their Characterization," M. Tech. Thesis, Materials Science Programme, IIT Kanpur (2001).
34. H. Schmidt and M. Mennig, "Wet Coating Technologies For Glass", downloaded from Internet.
35. Paul Morrell And Roy Taylor, "Thermal Diffusivity And Phase Structure of Zirconia-Based Thermal Barrier Coatings ", *Advances In Ceramics*, Vol. 24B, pp. 927-943.
36. B. E. Yoldas and T. W. O'Keeffe, "Antireflective Coatings Applied From Metal-Organic Derived Liquid Precursors ", *Applied Optics*, Vol. 18, No. 18, pp. 3133-3138 (1979).
37. J. E. Baurele, "Study Of Solid Electrolyte Polarization By A Complex Admittance Method ", *J. Phys. Chem. Solids* 30, pp. 2657-70 (1969).
38. T. Bhattacharya, "Enhanced Electrical Transport in KCl-KI System, " M. Tech. Thesis, Materials Science Programme, IIT Kanpur (2002).
39. A. Tiwari, "Electrical And Electric Modulus Studies On $\text{Li}_3\text{PO}_4\text{-Li}_2\text{S}$ Superionic System", M. Tech. Thesis, Materials Science Programme, IIT Kanpur (2001).
40. N. K. Singh, "Structure and Electrical Properties of Sol-gel $\text{ZrO}_2\text{-Gd}_2\text{O}_3$ Thin Films", M. Tech. Thesis, Materials Science Programme, IIT Kanpur (2002).

41. H. Kozuka and M. Kazimura, " Single Step Dip Coating of Crack-Free BaTiO₃ Films >1 μm Thick: Effect of Poly (vinylpyrrolidone) on Critical Thickness", J. Am. Ceram. Soc. 83 (5) pp. 1056-1062 (2000).
42. R. Howland and L. Benatar, "A Practical Guide to Scanning Probe Microscopy", Park Scientific Instruments (1997).
43. G. S. Kim, S. C. Hwang, Y. S. Kim and H. S. Shin, " Growth of Ytria-Stabilized Zirconia Thin Films on Textured Silver Substrate by Chemical Vapor Deposition", J. Am. Ceram. Soc. 85 (7), pp. 1897-1899 (2002).
44. S. Dutta, "Electrical Properties of ZrO₂-Gd₂O₃ Ceramics", M. Tech. Thesis, Materials Science Programme, IIT Kanpur (2001).
45. S. Dutta, S. Bhattacharyya and D. C. Agrawal, "Electrical Properties of ZrO₂-Gd₂O₃ Ceramics", Materials Science and Engineering B (in press).
46. X. Wang, J. Mei and P. Xiao, " Non Destructive Evaluation of Thermal Barrier Coatings using Impedance Spectroscopy", Journal of the European Ceramic Society 21, pp. 855-859 (2001).
47. M. Hartmanova, K. Gmucova and I. Thurzo, " Dielectric Properties of Ceria and Ytria-Stabilized Zirconia Thin Films Grown on Silicon Substrates", Solid State Ionics 130 pp. 105-110 (2000).

APPENDIX-1

CALCULATION OF THE AMOUNTS OF DIFFERENT INGREDIENTS USED IN THE PREPARATION OF ZIRCONIA (ZrO_2) AND GADOLINIA-DOPED ZIRCONIA SOL FOR THIN FILM PREPARATION

To prepare 10 ml of alkoxide solutions of unstabilized ZrO_2 and Gd_2O_3 -doped ZrO_2 , the different ingredients are required in the following amounts:

(1) Zr-n-Propoxide [$\text{Zr}(\text{OCH}_2\text{CH}_2\text{CH}_3)_4$]

Molecular weight = 327.57, Density = 1.05 gm/cc

For 0.2 M/L concentration,

$$\begin{aligned}\text{Wt. of Zr-n-P} &= 0.2 \times 327.57 \\ &= 65.514 \text{ gms in 1000ml.}\end{aligned}$$

Therefore, in 10ml of sol,

$$\text{Wt of Zr-n-P} = \frac{65.514 \times 10}{1000} \cong 0.655 \text{ gms.}$$

$$\begin{aligned}\text{Hence, Volume of Zr-n-P} &= \text{Mass/Density} = 0.655/1.05 \\ &= 0.624 \text{ ml (in 10 ml total volume of sol).}\end{aligned}$$

(2) Acetic acid

Molecular weight = 60.50, Density = 1.049 gm/cc

Molar ratio of acetic acid to Zr-n-P is taken as 3 i.e.,

$$\text{Acetic acid/Zr-n-P} = 3 \text{ (Molar Ratio)}$$

Therefore, the concentration of acetic acid = $3 \times 0.2 = 0.6 \text{ M/L}$

$$\begin{aligned}\text{and weight of acetic acid} &= 0.6 \times 60.05 \\ &= 36.03 \text{ gms in 1000 ml.}\end{aligned}$$

So, in 10 ml total volume of sol,

$$\begin{aligned}\text{weight of acetic acid} &= 36.03 \times (10/1000) \text{ gms} \\ &= 0.3603 / 1.049 = 0.252 \text{ ml.}\end{aligned}$$

(3) Amount of H₂O

The molar ratio of H₂O to Zr-n-P is taken 1.8.

The concentration of H₂O in sol = $1.8 \times 0.2 = 0.36 \text{ M/L}$

Weight of H₂O in 1000 ml = $0.36 \times 18 = 6.48 \text{ ml.}$

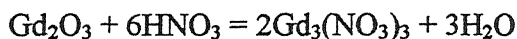
Hence, in 10 ml sol,

Amount of H₂O = $6.48 \times (10/1000) = 0.0648 \text{ ml.}$

(4) Amount of HNO₃

Molecular weight = 63, density = 1.4 gm/cc

Gadolinia reacts with nitric acid in the following way,



So, to dope x mole% Gd₂O₃ in ZrO₂, the required amount of gadolinia in 1000ml is

$$W = \frac{x}{(100 - x)} \times 0.2 \times M$$

where, M = Molecular weight of Gd₂O₃,

(100-x) is the mole% of ZrO₂,

The concentration of zirconia in Zirconium-n-Propoxide is 0.2 M/L.

From the above chemical equation, we see that 6 moles of HNO₃ are required for 1 mole of Gd₂O₃ to have 2 moles of gadolinium nitrate and 3 moles of H₂O in 1000 ml ZrO₂ sol.

Therefore, in 10 ml sol, the required volume of HNO₃ is

$$V_{HNO_3} = \frac{6 \times \left(\frac{W}{M}\right)}{d_{HNO_3}} \times \frac{63.01}{0.7} \times \frac{10}{1000} \quad \text{----- (1)}$$

In actual practice, 3 to 4 drops of HNO_3 were used. This gives an excess of nitric acid.

(5) Amount of Gd_2O_3

To prepare x mole% of Gd_2O_3 doped ZrO_2 sol of 0.2 M/L concentration, the number of moles of Gd_2O_3 required is

$$\frac{x}{(100-x)} \times 0.2 (M/L).$$

$$\text{The weight of } Gd_2O_3 \text{ required} = \frac{x}{(100-x)} \times 0.2 \times M_{Gd_2O_3} \text{ (gms) (in 1000 ml).}$$

where, $M_{Gd_2O_3}$ is the molecular weight of gadolinia.

Therefore, in 10 ml volume of sol,

$$\text{Weight of } Gd_2O_3 = \frac{x}{100 \times (100-x)} \times 0.2 \times M_{Gd_2O_3} \text{ (gms).}$$

(6) Amount of PVP (Poly-Vinyl Pyrrolidon)

In the present work, PVP/Zr ratio is taken as 0.5 after optimizing the problem of cracks. Molecular weight of PVP monomer is 111.

To prepare 0.2 M/L concentration and 10 ml total volume of the sol, the amount of PVP is calculated below:

Weight of PVP in 10 ml = (Number of moles of Zr-n-P \times 0.5 \times mol. wt. of PVP monomer)

$$\begin{aligned} &= 2 \times 10^{-3} \times 111 \times 0.5 \\ &= 0.111 \text{ gms.} \end{aligned}$$

(7) Ethyl Alcohol

Ethyl alcohol is used as a solvent.

For 10 ml sol preparation,

$$\text{Amount of ethyl alcohol} = \{10 - (\text{volume of Zr-n-P} + \text{volume of acetic acid} + \text{volume of H}_2\text{O})\}$$

Table A 1 gives the actual amounts of the various chemicals used to prepare the sols of different compositions.

Table A.1: Actual amounts of the various chemicals used to prepare the sols of different compositions.

| S. No. | Mole% Gd ₂ O ₃ | Zr-n-propoxide (gms) | Gd ₂ O ₃ (gms) | Ehtyl Alcohol (ml) |
|--------|---|-------------------------|---|-----------------------|
| 1 | 0 | 0.65 | 0.0 | 9.50 |
| 2 | 1.75 | 0.65 | 0.0130 | 8.97 |
| 3 | 2.5 | 0.65 | 0.0190 | 8.97 |
| 4 | 4 | 0.65 | 0.030 | 8.97 |
| 5 | 5 | 0.65 | 0.038 | 8.97 |
| 6 | 8 | 0.65 | 0.063 | 8.90 |
| 7 | 9 | 0.65 | 0.072 | 8.90 |
| 8 | 11 | 0.65 | 0.090 | 8.90 |
| 9 | 13 | 0.65 | 0.110 | 9.00 |

The following amount for other ingredients for all compositions are taken as below:

HNO₃ \cong 0.25 ml (3 to 4 drops),

Acetic acid \cong 0.36 gms,

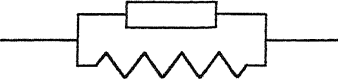
Water \cong 2 drops in HNO₃ plus 3 to 4 drops after addition of PVP,

PVP \cong 0.1 gms.

APPENDIX-2

Switch on the impedance analyzer

Press blue switch and then self test switch

1. Press OSC level and then press 50 mV
2. Press spot frequency
3. For short circuit test, first short the leads and then press the blue switch and then the short switch
4. To deactivate this mode separate the leads and then again press blue switch and short switch
5. Press  switch for parallel mode
6. For open circuit test, press blue switch and then open switch
7. To deactivate this mode press blue switch and then open switch again
8. Finally, press auto switch for auto mode
9. During calibration the display 'A' should show z and display 'B' should show θ .

APPENDIX-3

FOR COLE-COLE PLOTS

1. Table the data in an origin worksheet so that $\text{col(A)} = Z$ and $\text{col(B)} = \theta$
2. Set column values as $\text{col(C)} = \text{col(B)} * (3.14) / (180)$
3. Set column values as $\text{col(D)} = \text{col(A)} * \sin(\text{col(C)})$
4. Set column values as $\text{col(E)} = \text{col(A)} * \cos(\text{col(C)})$
5. Set column values as $\text{col(F)} = \text{col(D)} * (-1)$
6. Plot a graph having col (F) as Y-axis and col (E) as X-axis
7. Choose non-linear curve fit option from analysis(origin tool bar)
8. Choose circular fit and then change the parameters to obtain the best-fit semicircle.

FOR DIELECTRIC PLOTS

1. Table the data in an origin worksheet so that $\text{col(A)} = \text{capacitance(in pF)}$,
 $\text{col(B)} = \text{loss}$ and $\text{col(C)} = \text{frequency(in Hz)}$
2. Let the thickness of the given film under consideration be $d \mu\text{m}$
3. Set column values as $\text{col(D)} = 0.575767 * \text{col(C)} * d$
4. Set column values as $\text{col(E)} = \log(\text{col(D)})$
5. Set column values as $\text{col(F)} = \log(\text{col(B)})$
6. Plot two graphs one having col (E) as Y-axis and col (F) as X-axis and the other having col (B) as Y-axis and col (F) as X-axis.

A 144412

